SEISMIC SOURCE PROCESSES AND TECTONICS: OBSERVATIONS OF FOUR INTRACONTINENTAL EARTHQUAKES

Thesis by

John Joseph Cipar

In Partial Fulfillment of the Requirements

for the Degree of

Doctor of Philosophy

California Institute of Technology

Pasadena, California, U.S.A.

1981

(Submitted May 14, 1981)

In Memory of My Father, John;

To My Mother, Susan;

and to My Wife, Mary,

This Thesis Is Dedicated.

Acknowledgements

Certainly the most pleasant part of writing this thesis is to put into words my thanks to all of the people who have helped me to write it and who have made my years at Caltech so enjoyable. My advisors, Don Helmberger and Hiroo Kanamori, provided advice, patience and the resources which allowed me to finish this work. More than that, their own work and writings are models of excellent scientific research. Likewise the other faculty members at the Seismological Laboratory, in particular Tom Ahrens, have been valuable teachers, colleagues and good friends. Wai-Ying Chung, John Ebel, Tom Hanks, Tom Heaton, Chuck Langston, George Mellman, Jim Pechmann and Terry Wallace materially aided in doing this research either by correcting sometimes turgid prose, by valuable discussions and by providing necessary computer programs. Through these people, I want to thank all the other graduate students who have helped make my life so enjoyable and my work rewarding. A special thanks is due to John Ebel, a valued colleague, good friend and apartment-mate and a good soft-ball pitcher. I also want to thank the people who keep the Seismo Lab running: the Staff, in particular, Roberta Eager, Virginia Gilliam and Dee Page. Laszlo Lenches patiently reworked my wobbly drawings into fine figures, ably assisted by Joe Galvan. Roslyn Scherr and Mary Martyak typed and proofread parts of the manuscript. To all of you, for all you have been and done, Thank You.

This research was supported by National Science Foundation grants EAR78-14786 and PFR-7921769.

Abstract

This thesis presents studies of the source processes of four shallow earthquakes and their relation to regional tectonics. In the first chapter, long-period teleseismic P and S waves from the Haicheng, China earthquake of February 4, 1975 are compared directly to time domain synthetic seismograms to infer source parameters. The P-wave focal mechanism indicates that faulting was dominantly left-lateral strike-slip along a northwest striking nodal plane (strike = 288^{o}, dip = 78^{o}N, rake = 342^{o}). The strike of this nodal plane agrees with the trend of the aftershock distribution. Azimuthal variation of P-wave duration is attributed to fault rupture 22 km in a northwesterly direction, along strike of the aftershock zone. There is considerable discrepancy between the observed SH waves and synthetics computed using this model. These discrepancies are due to either structural complexities in the source region or change in fault mechanism as the rupture propagated along strike. Seismic moment, average dislocation and stress drop are computed to be 2.7 x 10^{26} dyne-cm, 2.5 meters and 48 bars, respectively.

The remaining three chapters present a detailed examination of seismograms recorded by the 1976 Friuli, Italy earthquake (May 6, 1976, M_S = 6.5) and two major aftershocks (both on September 15, 1976 at 03h 15m, M_S = 6.0 and 09h 21m, M_S = 5.9). Teleseismic long-period body waves and surface waves radiated by the mainshock and 09h 21m aftershock are studied in Chapter Two to determine source characteristics. Focal mechanisms along with geological evidence suggest that both events

represent underthrusting of the Friuli Plain beneath the Southern Alps. The depths of both earthquakes, estimated by matching synthetic body wave seismograms to observations, are found to lie between 6 and 10 km. Synthetic seismogram calculations which include source directivity effects suggest that the fault length of the mainshock is approximately 16 to 24 km assuming a rupture velocity of 3.0 km/sec. Observations of 100 sec Rayleigh waves confirm the body wave focal mechanism, but suggest that the seismic moment of the mainshock is 5×10^{25} dyne-cm compared to 2.9×10^{25} dyne-cm estimated from body waves. The P-wave moment of the aftershock is 1×10^{25} dyne-cm.

In Chapter Three, short-period records are modeled to obtain additional details of the source time history. Two point sources of radiation are required to adequately model the aftershock short-period records. For the 09h 21m aftershock, the model derived from short-period records also produces good fits to the long-period data. The SP model for the 03h 15m aftershock, on the other hand, predicts long-period synthetics which do not agree with the observations. In particular, the SP moment (0.37×10^{25} dyne-cm) is about 2-1/2 times smaller than the LP moment (1×10^{25} dyne-cm). Adding a long-period component to the SP model considerably improves LP waveform and moment agreement. In the case of the mainshock, a reasonable fit to the observed SP data is obtained using three point sources of radiation. However, LP synthetics computed using this model do not agree with the observations, and the SP moment (0.65×10^{25} dyne-cm) is a small fraction of the LP moment ($3\text{-}5 \times 10^{25}$ dyne-cm). Time function durations

indicate that the individual events inferred from the SP records are radiated from patches of the fault having radii of 2 to 4 km and stress drops in the range 35 to 276 bars. In comparison, overall stress drops estimated from LP data are found to be 12 bars (mainshock) and 24 bars (09h 21m aftershock). Strong-motion accelerograms are used to put additional constraint on the source geometry of the 09h 21m aftershock.

The 03h 15m and 09h 21m aftershocks are the culminating events of a series of large aftershocks which began on September 11, 1976. Cumulative seismic moment of the Friuli aftershock sequence was as large as the moment released by the mainshock. By comparison, aftershock moments of California earthquakes are typically 1 to 10 percent of the mainshock moment. The large size, location and focal mechanism of the aftershocks suggest that they represent failure of major stress concentrations remaining after the mainshock.

TABLE OF CONTENTS

INTRODUCTION

This thesis describes studies of the source processes of four moderate-sized, shallow earthquakes and their relation to regional tectonics. The first chapter discusses the source of the February 4, 1975 Haicheng, China earthquake (origin time = 11h 36m GMT, M_S = 7.4). This shock was one of a series of six large earthquakes which struck northeastern China between 1966 and 1976 and was preceeded by numerous foreshocks and other precursory phenomena. It has the distinction of being the first major seismic event to have been predicted. Because of the timely prediction, the potentially great loss of life was minimized.

The remaining three chapters present a detailed discussion of the source processes of the 1976 Friuli, Italy earthquake sequence. The Friuli sequence began on May 6, 1976 with the M_S = 6.5 mainshock (origin time = 20h 00m GMT). A small foreshock (M_L = 4.5) preceeded the mainshock by one minute. On September 15, 1976, two major aftershocks, at 03h 15m (M_S = 6.0) and at 09h 21m (M_S = 5.9, occurred within the aftershock zone of the mainshock. The mainshock and accompanying aftershocks resulted in heavy casualties and severe property damage in northeastern Italy.

Chapter Two discusses the tectonic setting of the Friuli earthquakes and describes modeling of teleseismic long-period body and surface waves written by the mainshock and 09h 21m aftershock. Teleseismic short-period records are inverted in Chapter Three to obtain a more detailed estimate of the source time function. The teleseismic

short-period models are tested against locally recorded strong-motion data. The fourth chapter presents a synthesis of the results of the waveform modeling with an interpretation of the regional tectonics.

The thread which ties the Haicheng earthquake to the Friuli sequence is that both are intracontinental earthquakes in regions of moderate seismicity. They occur in distinctly different tectonic environments, however. The Friuli events are the consequence of the collision between Africa and Eurasia. The ultimate cause of the Haicheng earthquake is unclear, although it may be related to the northward movement of India into central Asia. On the scale of the history of the Earth, these earthquakes are vanishingly brief episodes, yet they have significant impact on the human populations which resided in the areas affected by them. The goal of this thesis is to better understand the processes which occur at the source of these earthquakes and from this infer their relation to regional tectonics.

The basic data for most of this thesis are teleseismic body wave seismograms recorded by the World Wide Standardized Seismograph Network (WWSSN). The method of analysis is to compute realistic time-domain seismograms comparing these directly to the observed records. Parameters describing the model are changed until reasonable agreement between observed and synthetic waveforms is obtained. For the purpose this study, teleseismic records are those observed at distances between 30^{o} and 90^{o}. Body waves that emerge at these ranges have their turning point below the lowest upper mantle discontinuity and above the core-mantle boundary in a region of smooth velocity increase (Burdick

and Powell, 1980). Thus, the signal emitted from the source region is relatively undistorted by the earth's velocity structure. The primary effect of the mantle is to attenuate the wave, both geometrically (Bullen, 1965, p. 125) and anelastically. Numerical values for the geometrical spreading coefficient for a shallow source are given in Langston (1976a). Kanamori and Anderson (1977) point out that available data suggest that seismic attenuation is independent of frequency in the period range from 1 hour to 1 sec. In order to preserve linearity and causality, any constant attenuation model implies phase velocity dispersion (Futterman, 1962; Carpenter, 1966). Carpenter (1966) derives the time-domain impulse response for such an absorption model parameterized by the ratio of the travel time, T, to average Q (T/Q). Interpretation of free oscillation and surface wave attenuation measurements suggest that for long-period P waves, T/Q_P should be about 1.0 sec at the distance range 30^o to 90^o (Anderson and Hart, 1978). Body-wave observations at periods shorter than 1 sec give $T/Q_P \sim 1.0$ sec implying that Q is, in fact, frequency dependent (Frasier and Filson, 1972; Der et al., 1980). T/Q ratios for S waves are approximately four times the P-wave value (Carpenter and Flinn, 1965). That is, T/Q_S is about 4.0 sec. Burdick (1978), however, determined T/Q_S to be 5.3 sec for paths across North America.

The starting point for the theoretical treatment of seismic sources is the elastodynamic representation theorem. Haskell (1964) presents a lucid derivation of the far-field radiation from a planar shear dislocation using this theorem. Such a source is equivalent to a

distribution of point double couple forces (Burridge and Knopoff, 1964). Haskell shows that at sufficiently great distance, P and S waves decouple and that the radiation pattern is separable from the time history of displacement. By "sufficiently great distance", we mean the distance at which the direction cosines are essentially constant over the fault plane. Furthermore, the time dependence is proportional to the derivative of the time history of faulting. The form and duration of the time function observed at each receiver point depends on the mode of rupture propagation and the orientation of the fault plane relative to the receiver (e.g., Savage, 1966). As Savage (1965) points out, the radiation pattern is unaffected by the details of fault propagation. In addition, P waves and S waves in general, have time functions of different shapes and durations.

The presence of the free surface reflects upgoing rays causing them to interfere in a complex fashion (depending on depth and local seismic velocity) with the downgoing direct waves. Relative amplitudes of the up and down going waves are controlled by the focal mechanism and the azimuth and take-off angle at which the rays emerge from the focal sphere. Crustal structure in the source region further complicates the waveform by creating additional internally reflected waves which then are radiated to the far-field. Reflection and transmission coefficients at the free surface and at internal crustal boundaries are computed assuming a plane wave approximation.

We will assume that a moderate-sized, shallow earthquake can be approximated at teleseismic distances by a point shear dislocation (or

possibly by several such sources). Because the spatial extent of the source is small, we will assume that the time function is constant over the focal sphere. That is to say, all rays have the same time function irrespective of wave type (P or S), take-off angle or azimuth. In the study of the Haicheng earthquake, we will be forced away from this assumption in modeling the P waves. On the other hand, this assumption seems to be valid for the Friuli earthquakes.

The instrument response was calculated using the method described by Hagiwara (1958) for World Wide Standardized Seismograph Network (WWSSN) long- and short-period instruments. A measure of the effective bandwidth of the instrument is the period range over which the response is within a factor of 10 of the peak magnification. Using this criterion, the effective bandwidths of the long-period (peak magnification at 15 sec) and short-period (peak at 0.6 sec) instruments are approximately 1 to 100 sec and 0.1 to 2 sec respectively. For earthquakes of the size studied in this paper, long-period records measure primarily the flat portion of the source spectrum whereas short-period instruments sample the high-frequency slope.

An equation illustrating these factors for the vertical P-wave group in a half-space is:

$$W(t) = (M_o/G)\{C(t)*I(t)*Q(t)*S(t)\}$$

with

$$C(t) = R(\phi,\theta)\{\delta^P(t) + R_{pP}\delta^{pP}(t') + R_{sP}\delta^{sP}(t'')\}$$

where $C(t)$ = the source crustal response, including the free surface

M_o = the seismic moment

G = the geometrical spreading factor

I(t) = time-domain instrument operator.

Q(t) = attenuation operator

S(t) = far-field source time function

$R(\phi,\theta)$ = radiation pattern.

R_{pP}, R_{sP} = reflection coefficients at the free surface.

* indicates the convolution operation.

t', t'' = time lags relative to direct P-wave time, t.

Note that the delta function, $\delta(t)$, is the form that the medium response takes under the far-field, first-motion approximation. The derivation and the explicit form of these relations are described by Helmberger (1974), Langston and Helmberger (1975) and Langston (1976a). A comprehensive review of source studies by time domain synthetic seismograms has been given by Helmberger and Burdick (1979). The above expression for the medium response, C(t), represents the generalized ray formulation. Crustal reverberations are computed by multiplying the delta function response by the appropriate reflection and transmission coefficients corresponding to the ray path and wave type (P or S). Alternatively, C(t) can be described by layer matrices (Haskell, 1960, 1962; Fuchs, 1966; Langston, 1976a) which automatically include all crustal multiples.

The amplitude of the synthetic is scaled by the seismic moment, M_o, which is determined at zero frequency (or, in practise, long periods). To do this properly, the zero frequency level of S(t) and Q(t) must be unity:

$$\lim_{\omega \to 0} \int_0^\infty S(t)dt = 1$$

(Langston and Helmberger, 1975). The seismic moment is given by $M_o = \mu D_o A$ where μ is the rigidity (dynes/cm^2), D_o is the average dislocation and A is the fault area (Aki, 1966). The observed seismic moment for each record is obtained by the formula:

$$M_o{}^{obs} = (A^{obs}/A^{syn})M_o{}^{syn}$$

where A^{obs} and A^{syn} are the observed and synthetic amplitudes in microns and the M_o are the corresponding seismic moments in dyne-cm.

We will now examine the interaction of the source time function with the instrument and attenuation operators. Figure I-1 shows the time domain response of WWSSN long-period (seismometer period, Tp = 15 sec; galvanometer period, Tg = 100 sec) and short-period (Tp = 1.0 sec, Tg = 0.75 sec) seismographs to an input delta function (Hagiwara, 1958) and these responses convolved with a Futterman (1962) Q-operator calculated using T/Q = 1.0 sec. Below the plots of I(t)*Q(t), these functions are shown convolved with various idealized far-field source time functions, S(t), having the form of triangles and trapezoids (defined by the rise, top and fall times, indicated below each time function). While triangular and trapezoidal time functions are unphysical in that they predict singularities in acceleration and displacement (Savage, 1972), their value lies in the fact that they reproduce the overall shape of the far-field time functions predicted by reasonable theories of the seismic source (e.g., Savage, 1966;

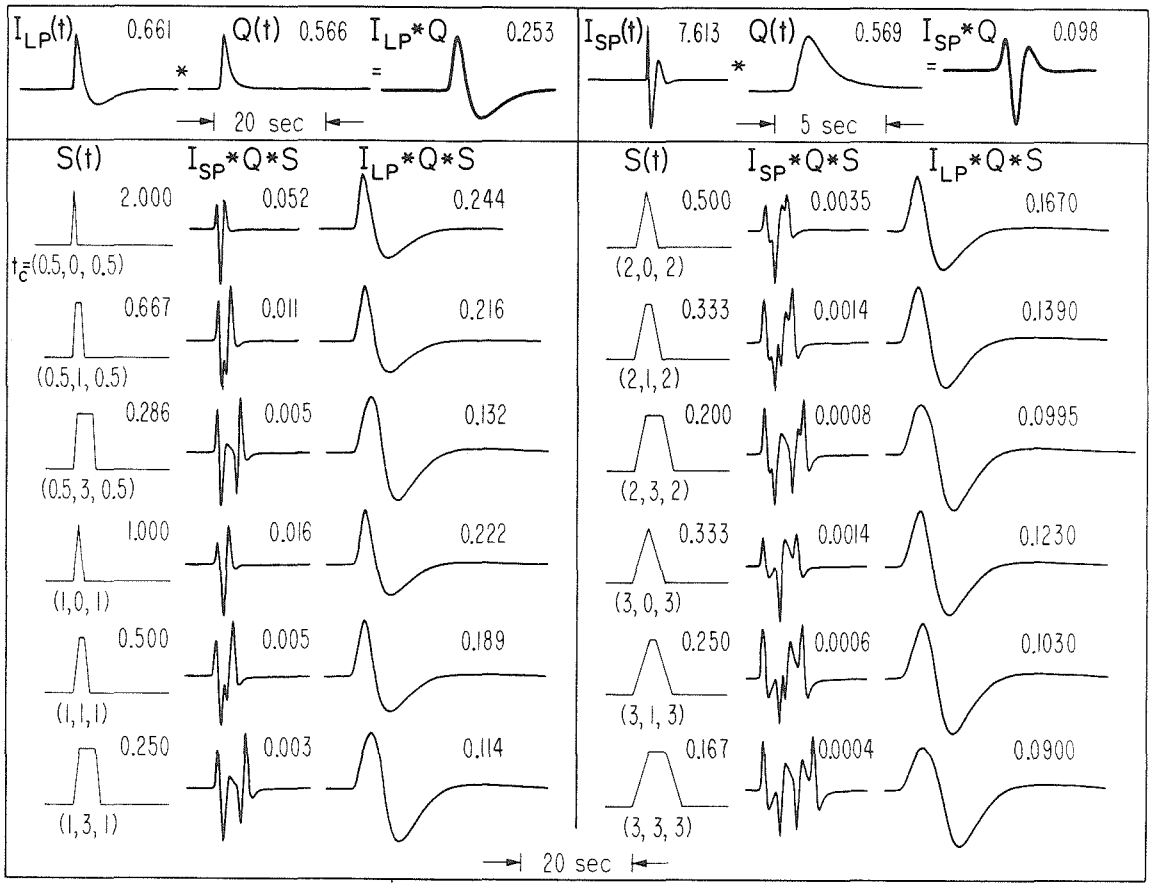

Figure I-1. WWSSN long-period (I_{LP}: Tp = 15 sec, Tg = 100 sec) and short-period (I_{SP}: Tp = 1.0 sec, Tg = 0.75 sec) instruments where Tp = pendulum period and Tg = galvanometer period, convolved with Futterman's (1962) Q-operator (T/Q = 1.0 sec) and with various far-field time functions (time durations in sec of rise, top and fall indicated by t_c). The numbers after the waveforms are zero to peak amplitudes scaled to make the zero frequency level equal to unity to allow final scaling by seismic moment.

Madariaga, 1976).

Figure I-1 illustrates how long-period and short-period instruments respond to time functions having different shapes and durations. Note that the long-period waveforms (columns headed I_{LP}*Q*S) do not change very much in overall shape with different time functions; whereas the short-period waveforms (I_{SP}*Q*S) are quite sensitive to the shape of S(t). In addition, the amplitudes of the long-period waveforms vary by a factor of 2-1/2 for the time functions shown, whereas the short-period amplitudes range over two orders of magnitude. A corollary of this is that an earthquake with a very long time function would have negligible response on a WWSSN short-period seismograph. The crucial point for short-period records is that the instrument is sensitive to the sloping parts of the time function. For example, note the differences between t_c = (1, 3, 1) and t_c = (3, 3, 3) cases: there is an extra "glitch" in the second case. Also note how the flat portion of the time function does not contribute to the short-period response (e.g., t_c = (0.5, 3, 0.5)).

The effect of different T/Q values on I_{SP}*Q*S is illustrated in Figure I-2 for two representative triangular and trapezoidal time functions. There is little change in overall duration with changing T/Q; the duration being controlled, as mentioned above, by the slopes of the time function. The Q-operator is a smoothing filter. Synthetics computed with lower values of T/Q have enhanced high frequency characteristics whereas the long-period shape of the signal is relatively unaffected. Note that amplitudes vary by nearly an order of

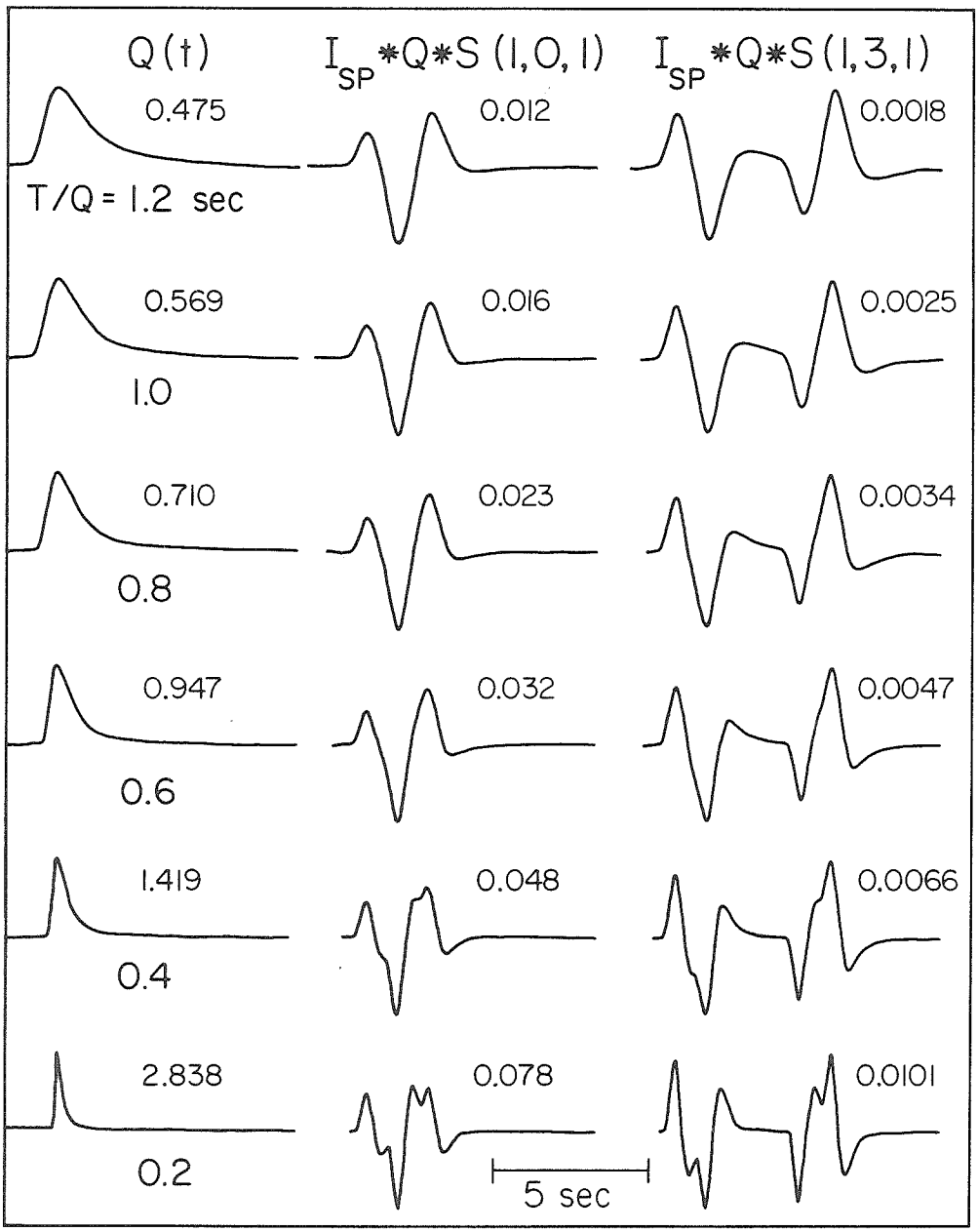

Figure I-2. Variation of I_{SP}*Q*S for various values of T/Q ratio. Left column shows Q(t) computed using a frequency independent Q-operator (Futterman, 1962). The Q-operator convolved with the short-period instrument and triangular and trapezoid time functions are shown in the center and right columns respectively. Other notation is the same as Figure I-1.

magnitude over the range of T/Q ratios shown with synthetics computed using lower T/Q values having the largest amplitude.

The processes which take place at the earthquake source manifest themselves in the time function, S(t). The goal of this thesis is to interpret this function in terms of fault mechanics which then can be related to regional tectonics. Observed azimuthal variation S(t) for the Haicheng earthquake will be interpreted as fault propagation in a direction transverse to the regional structural grain. The complexity of the short-period time functions of the Friuli earthquakes imply wide variation of strength and stress in the fault zone.

Chapter One

Source Processes of the Haicheng, China Earthquake from Observations of P and S Waves

Introduction

The Haicheng, Liaoning Province, China Earthquake of February 4, 1975, was the first major earthquake to have been successfully predicted (Raleigh et al., 1977). Using a variety of observations, principally tilt measurements and seismicity, Chinese seismologists continually improved their estimate of the time and location of the impending event.

By 1970, long-term trends in seismicity suggested to Chinese seismologists that Liaoning Province, in northeastern China, would be the site of the next large event in a series of earthquakes which began in 1966. During this series, epicenters of large earthquakes (1966 Hsingtai earthquakes, 1967 Tientsin and 1969 Pohai Gulf) migrated northeastward towards Liaoning Province (Figure 1-1). This long-term prediction led to increased geophysical studies in Liaoning Province such as new seismic stations and more tilt observations. Beginning in late 1973, the frequency of small earthquakes in Liaoning Province showed a significant increase over the previous two years (Figure 1-2a) while previously slow ground tilting accelerated. These geophysical observations spurred provincial authorities to make preparations for a major disaster and to step up their program of alerting the citizenry.

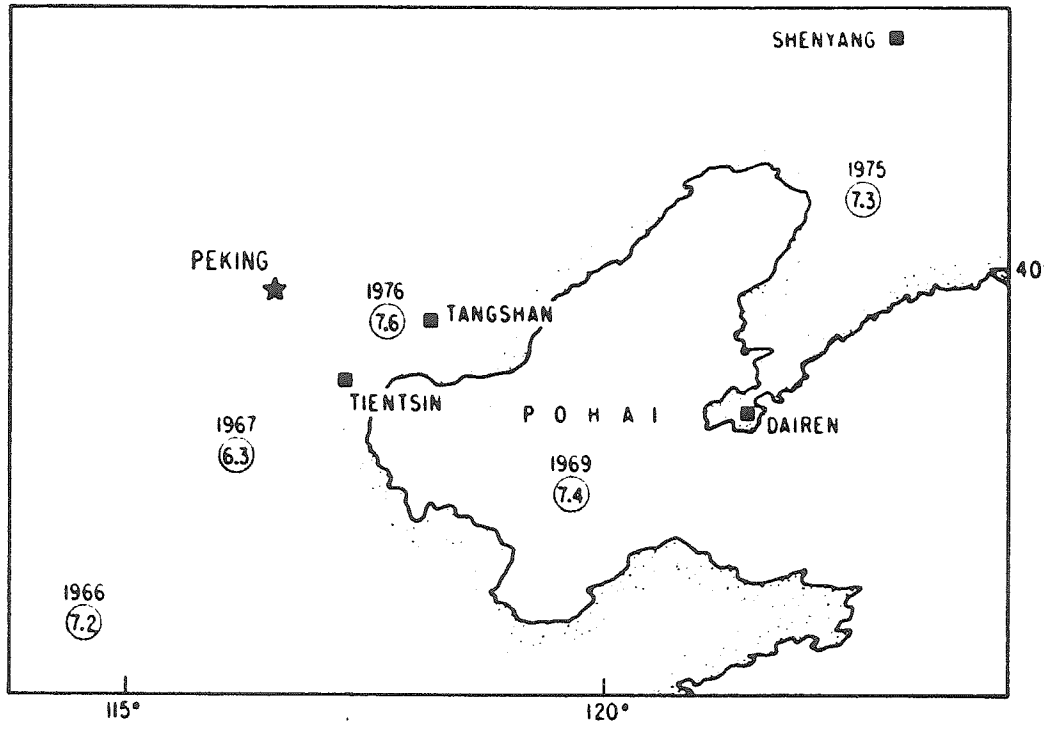

Figure 1-1. Large earthquakes of northern China (M = 6.1 or greater) since 1966 are shown as circles enclosing the magnitude value. (After Raleigh et al., 1977).

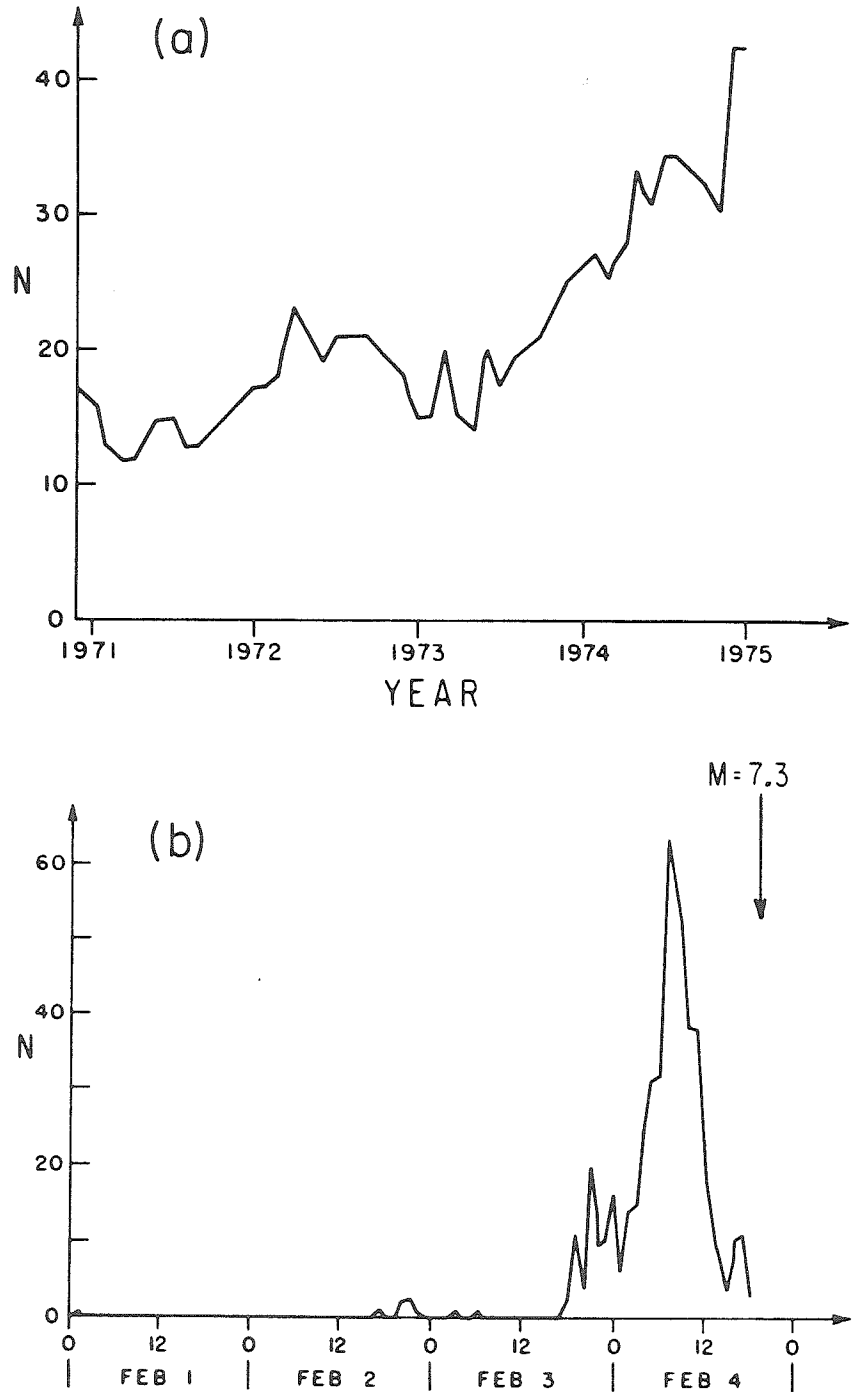

Figure 1-2. (a) Monthly numbers of earthquakes in Liaoning Province from December 1970 to February 1975. (b) Frequency of foreshocks to the Haicheng earthquake (After Raleigh et al., 1977).

On February 1st, a magnitude 0.5 earthquake ushered in a dramatic rise in seismic activity, during which the magnitude and frequency of the events continually increased (Figure 1-2b). The sequence culminated in a magnitude 4.7 shock on February 4th at 7:50 AM (local time), after which the number of events declined precipitously. The earthquakes apparently were tightly clustered in depth and location and exhibited very similar focal mechanisms (Wu et al., 1976). Furthermore, the b-value of the series was very low (0.56), in contrast to earthquake swarms whose b-values are observed to be in the range 0.70 to 1.00. According to Wu et al. (1976), the single most important factor in identifying the sequence as a foreshock series and thus making the prediction was the rapid decrease in activity after the M_L = 4.7 event. This behavior is untypical of swarms, but is a pattern which Chinese seismologists have identified as being precursory to other large earthquakes. From the amount of damage to homes and other buildings, the prediction of this earthquake undoubtedly saved many thousands of lives. Scholz (1977) has suggested that the series of large earthquakes including the Haicheng earthquake and its precursory phenomena were triggered by a deformation front propagating through northeastern China. The mainshock occurred at 11h 36m GMT on February 4, 1975 with a surface wave magnitude of 7.4 (USGS). Basic parameters of the mainshock are listed in Table 1-1.

This chapter is concerned with the interpretation of the source processes of the Haicheng earthquake by analysis of teleseismic body waves. In particular, the agreement between P-wave and S-wave

Table 1-1. Mainshock Parameters

Date: February 4, 1975 Origin Time: 11h 36m 07.5s GMT (USGS)

Location: Liaoning Province, China

40.6^{o}N, 122.6^{o}E (USGS)

40.65^{o}N, 122.8^{o}E (Gu et al, 1976)

Depth: Normal focal depth (USGS)

12 km (Gu et al, 1976)

Magnitude: m_b = 6.4, M_S = 7.4 (USGS)

M = 6.7 (Pasadena)

Fault Mechanism:* strike = 288^{o}

dip = 78^{o}N

rake = 342^{o}

*coordinate system of Langston and Helmberger (1975)

observations will be investigated. The method outlined in the introduction will be employed to construct synthetic seismograms in the time domain using a plane wave approximation to generalized ray theory for shear dislocation sources and to compare these directly to the observations. In this way, source parameters such as seismic moment, fault dip, rake, strike, source depth and source time function can be estimated. Although this work does not deal specifically with earthquake prediction, the information presented should be of help in evaluating earthquake prediction data. Specifically, it may be of interest to compare this source model for the Haicheng earthquake to source models of other earthquakes that were not preceded by premonitory tilt and seismicity.

Geological and Seismological Setting

Geomorphologically, Liaoning Province consists of a sediment filled central valley trending northeast-southwest flanked on either side by mountainous regions. The central valley is bounded on the south by Pohai Gulf while the eastern mountains extend southwestward into the Gulf to form Liaotung Peninsula (Figure 1-3). Numerous northeast striking faults, showing evidence of recent movement, have been mapped on Liaotung Peninsula and in the mountains to the north (Raleigh et al., 1977). These faults are believed to be extensions of the Tanlu Fault, a system of strike-slip faults in Shantung Province south of Pohai Gulf. The 1969 Pohai Gulf earthquake (M_S = 7.4) is evidence that this fault system is presently active (Figure 1-1).

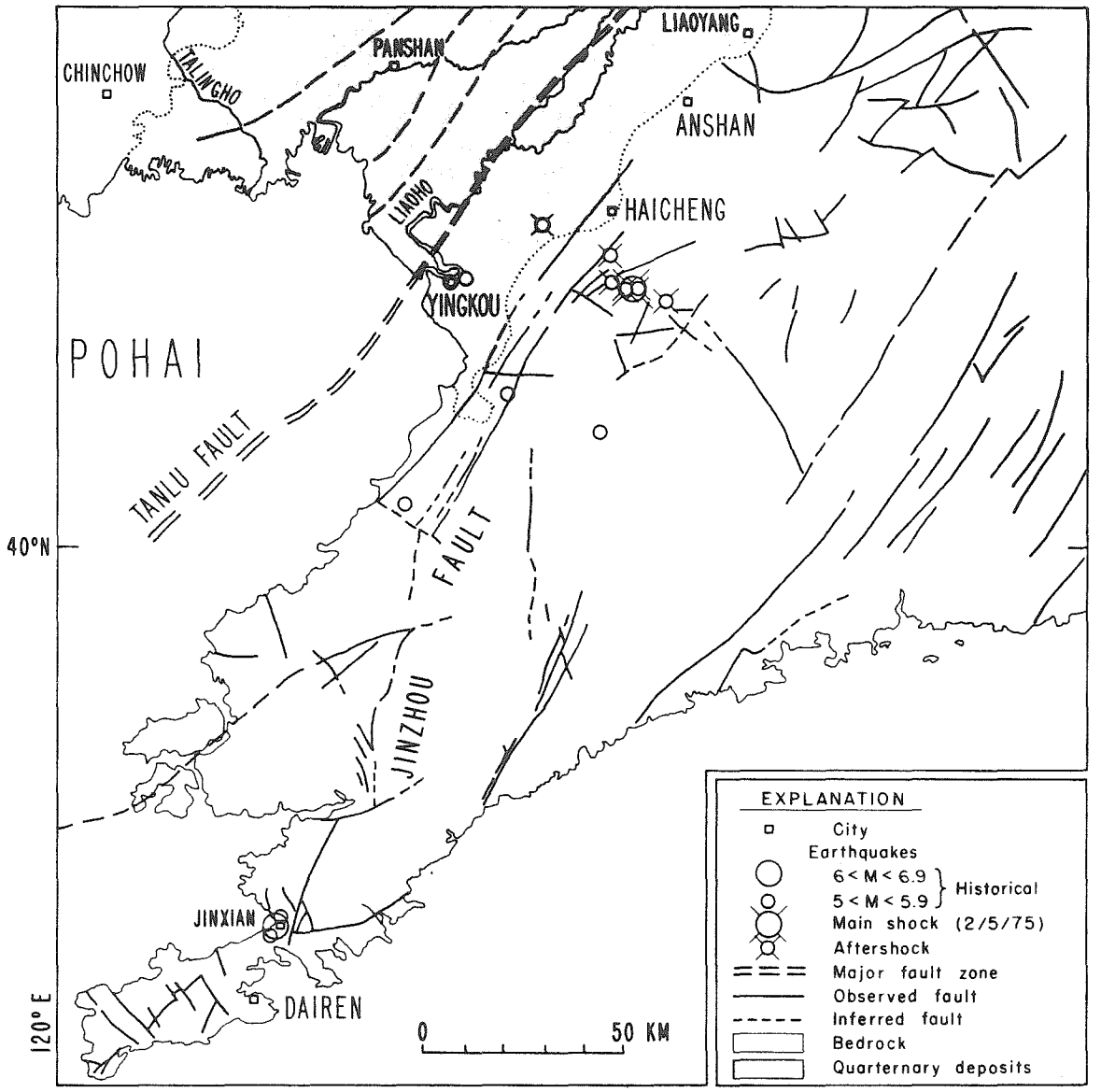

Figure 1-3. Generalized geological map of Liaoning Province showing mapped faults and epicenters of the Haicheng earthquake and its aftershocks. Stipled area is a Quaternary sedimentary basin; dotted lines are edges of the basin (After Raleigh et al., 1977).

The Haicheng earthquake occurred near the contact between the central valley and the eastern mountains. However, the aftershock distribution map (Figure 1-4) derived from local data (Gu et al., 1976), indicates that faulting did not take place on one of the northeast trending faults, but occurred on a fault plane aligned west-northwest. According to Hsu (1976), the aftershocks covered an area about 70 km x 30 km and most were shallower than 12 km. A cross-section of aftershock hypocenters normal to the strike of the distribution shows that the aftershocks define an almost vertical plane (Figure 3 of Hsu, 1976). The aftershock distribution is aligned very well with the west-northwest striking nodal plane of the teleseismic P-wave first motion diagram (Figure 1-5). This diagram, which was constructed using long-period WWSSN data, agrees closely with the mechanism derived from local data (Hsu, 1976). The first motion diagram indicates predominantly strike-slip motion on nearly vertical fault planes. Choosing the west-northwest striking plane as the fault plane, the motion is left-lateral with the following parameters: strike = 288^{o}, dip = 78^{o}, rake = 342^{o} (sign convention for the fault mechanism is that of Langston and Helmberger, 1975). Mechanisms of the aftershocks (Gu et al., 1976) are very similar to the mainshock mechanism. The mainshock focal depth estimate of 10 km from teleseismic data agrees well with the 12 km depth computed from local observations.

Data

The Haicheng earthquake was well recorded by WWSSN stations around

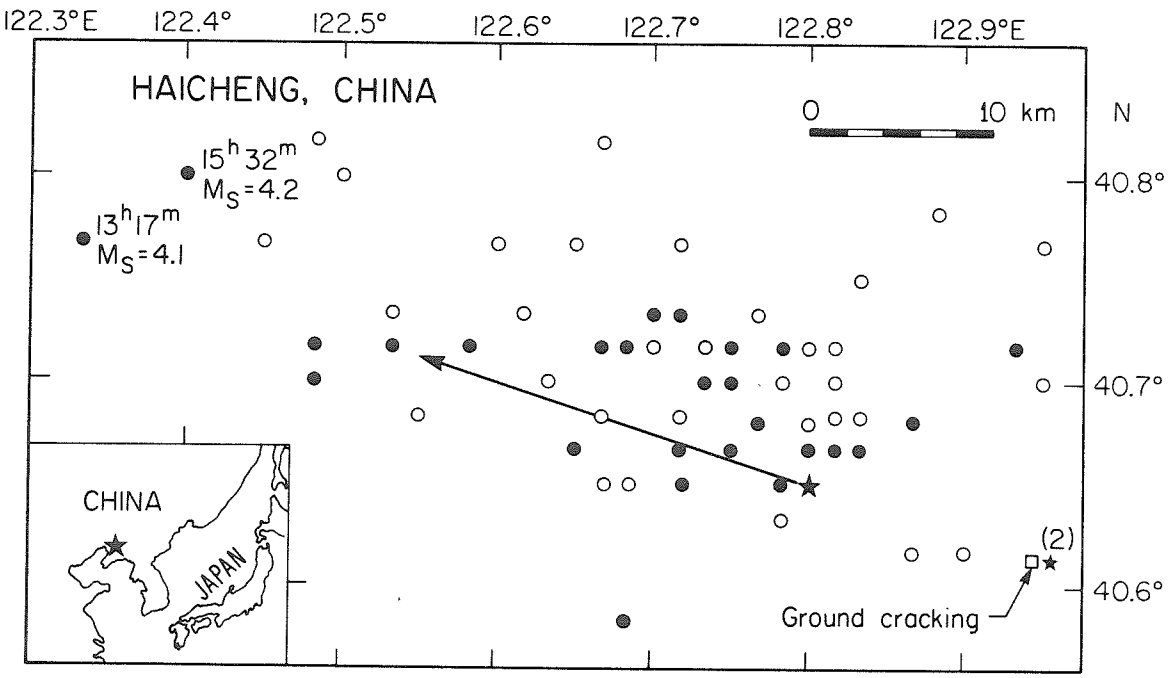

Figure 1-4. Map of aftershock distribution. Star marks the mainshock epicenter (origin time = 11h 36m). Closed circles are aftershocks which occurred within one day of the mainshock; open circles are later aftershocks. Times of two aftershocks which occurred within four hours of the mainshock at the northwest end of the aftershock zone are indicated. Data is from Gu et al. (1976). Heavy line indicates length and direction of fault propagation inferred from P waves. Locality of ground cracking as reported by Raleigh et al. (1977) is noted. Star with (2) indicates location of secondary source of radiation (see text and Figure 1-8).

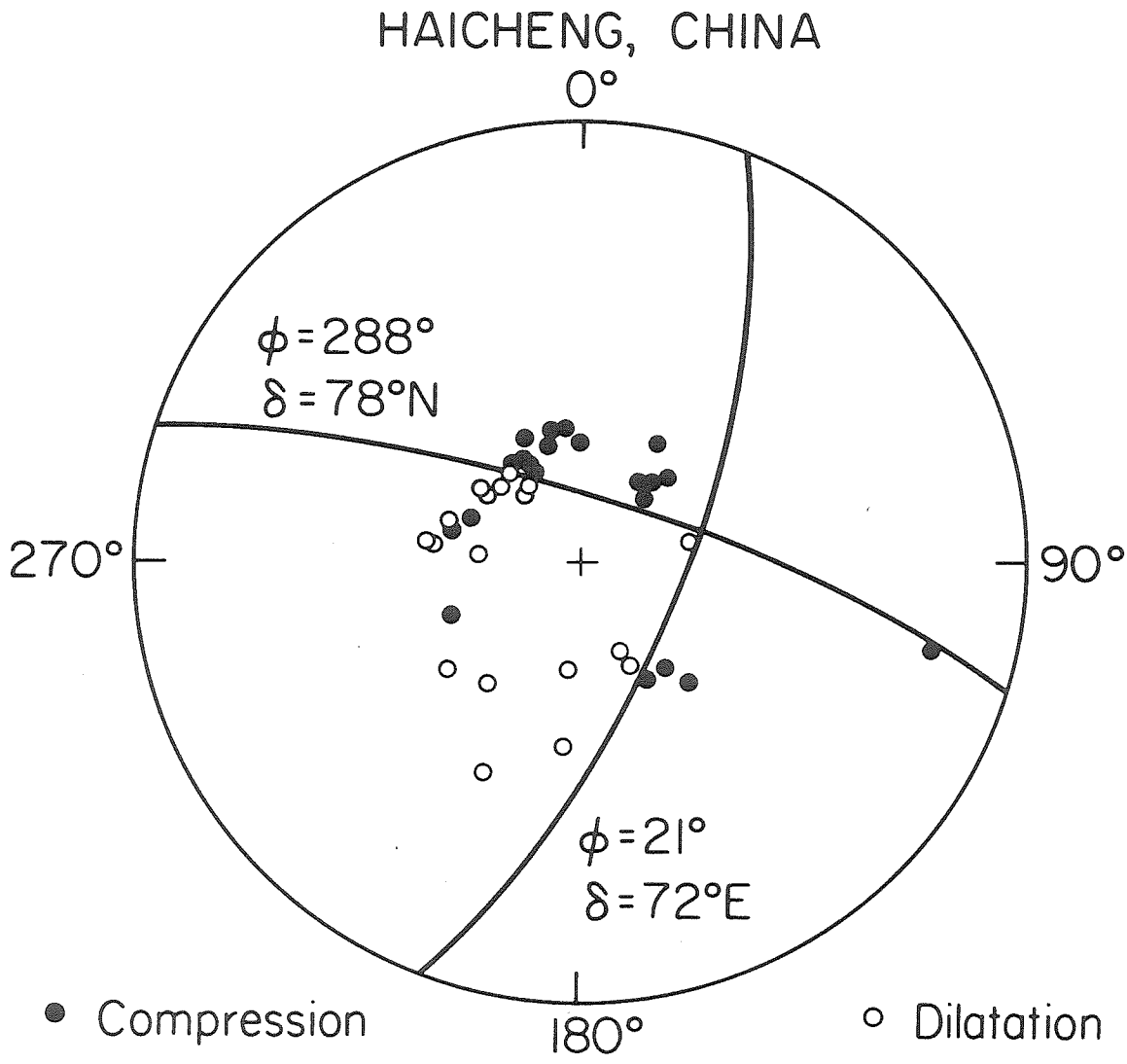

Figure 1-5. Teleseismic P-wave first motion diagram plotted on lower half of the focal sphere. Observations were read on WWSSN long-period vertical seismographs.

the world and a good collection of on-scale records is available. P-wave polarities were read from long-period WWSSN vertical seismograms and plotted on the focal mechanism (Figure 1-5) discussed above. Twelve P-wave and nine S-wave records were selected for further study based on clarity of recording and absence of long-period noise. To minimize complications due to upper mantle structure and core effects, only stations within the distance range 30^{o} to 85^{o} were used. Also, stations with obvious S-coupled PL waves were eliminated.

The seismograms were digitized on an electronic digitizing table and then detrended, deskewed, interpolated and plotted at a uniform magnification and time scale by computer. North-south and east-west components of the S waves were digitized and numerically rotated to produce transverse (SH) and radial (SV) waves. Station information and P-wave first motions are listed in Table 1-2.

Body Wave Modelling

Preliminary synthetics for the Haicheng earthquake were constructed using a single point source in a half-space. The first step was to test the determination of source depth (h = 10 km) and focal mechanism (strike = 288^{o}, dip = 78^{o}N, rake = 342^{o}) by computing synthetics for different values of each parameter and observing changes in wave shape. Source depth controls the separation of each phase (P, pP, sP) while the focal mechanism determines the polarity and relative amplitude of the phases. The above values for depth and focal mechanism produced the best fitting synthetics.

Table 1-2. Station Data

Station	Distance (deg)	Azimuth (deg)	Back Azimuth (deg)	P-wave Reading*	Synthetic
AAE	79.7	273.2	50.2	i-	P,S
ADE	76.7	166.6	347.6	e+	S
ATU	72.4	305.2	51.9	i-	P,S
AFI	81.2	116.5	315.5	node	S
COR	76.5	42.1	314.4	e+	S
GDH	70.4	358.6	3.0	i+	P
GUA	33.2	138.0	328.5	e+	P,S
IST	67.3	305.2	55.3	i-	P
MSH	48.7	286.5	64.6	i-	P,S
MUN	72.5	185.9	5.3	i-	P,S
PMG	54.7	150.0	337.4	e+	P
PTO	87.4	325.6	34.7	e-	P
RIV	78.6	156.2	338.3	e-	P
VAL	79.2	332.6	34.4	i+	P,S

*e = emergent first arrival, i = impulsive arrival
+ = up first motion on vertical seismogram,
- = down first motion

The major factor controlling the shape of the synthetic is the far-field source time function. The time function appropriate for a long, slender strike-slip fault can be approximated by a trapezoid (Savage, 1972). By trial-and-error, it was found that a trapezoidal time function of 7 sec duration with 1 to 2 sec ramps at either end produced the best overall fit to the P and S waveform data. The synthetic seismograms were not very sensitive to the length of the ramp part of the time function. Anelastic attenuation effects were included in the synthetic seismogram calculations using the Futterman (1962) frequency independent Q-operator with T/Q = 1.0 sec for P waves and 4.0 sec for S waves.

Data on crustal structure in northeastern China are presently not available; however, synthetics calculated for a strike-slip source in reasonable continental structures indicate that the principal effect of structure is to modify the latter part of the waveform while not appreciably affecting the first 10 sec. For this reason, the earthquake can be modelled as a point source in a halfspace. The wide variety of receiver crusts, ranging from oceanic island to continental rift zone, precluded any attempt to include the effect of receiver crustal structure on the synthetics.

A comparison of observed P and S waves to synthetics computed for a point source in a halfspace is shown in Figures 1-6 and 1-7. The overall agreement in polarity, shape and relative amplitude between the observed data and synthetics is good, indicating that the basic parameters of the model (fault mechanism, depth, time function) are

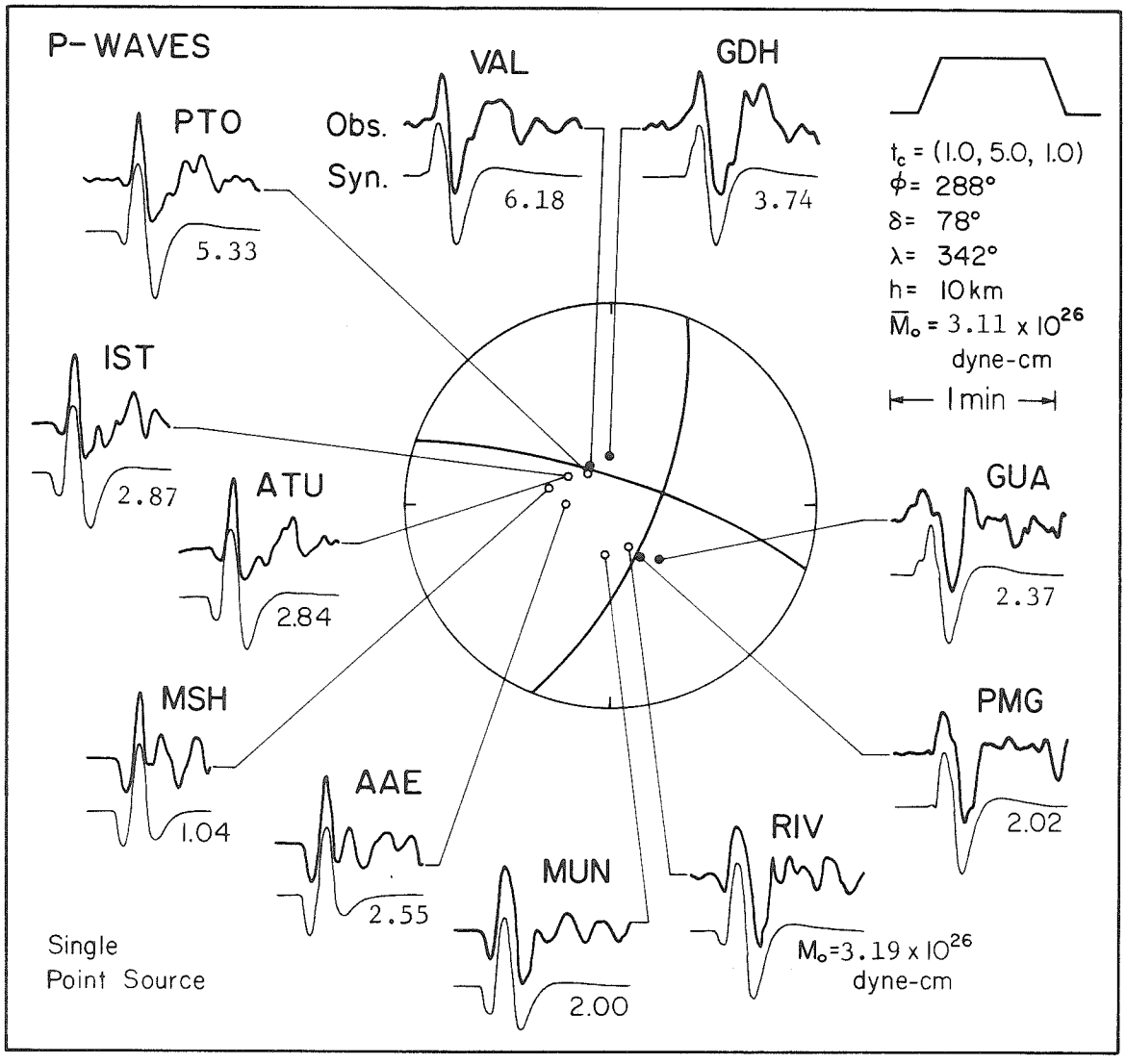

Figure 1-6. Comparison of observed and synthetic P waves. Synthetics are computed for a point source at 10 km depth in a halfspace. Far-field time function, t_c, is a trapezoid of 7 sec duration. Fault strike (ϕ), dip (δ), rake (λ), source depth (h) and average moment (M_o) are indicated.

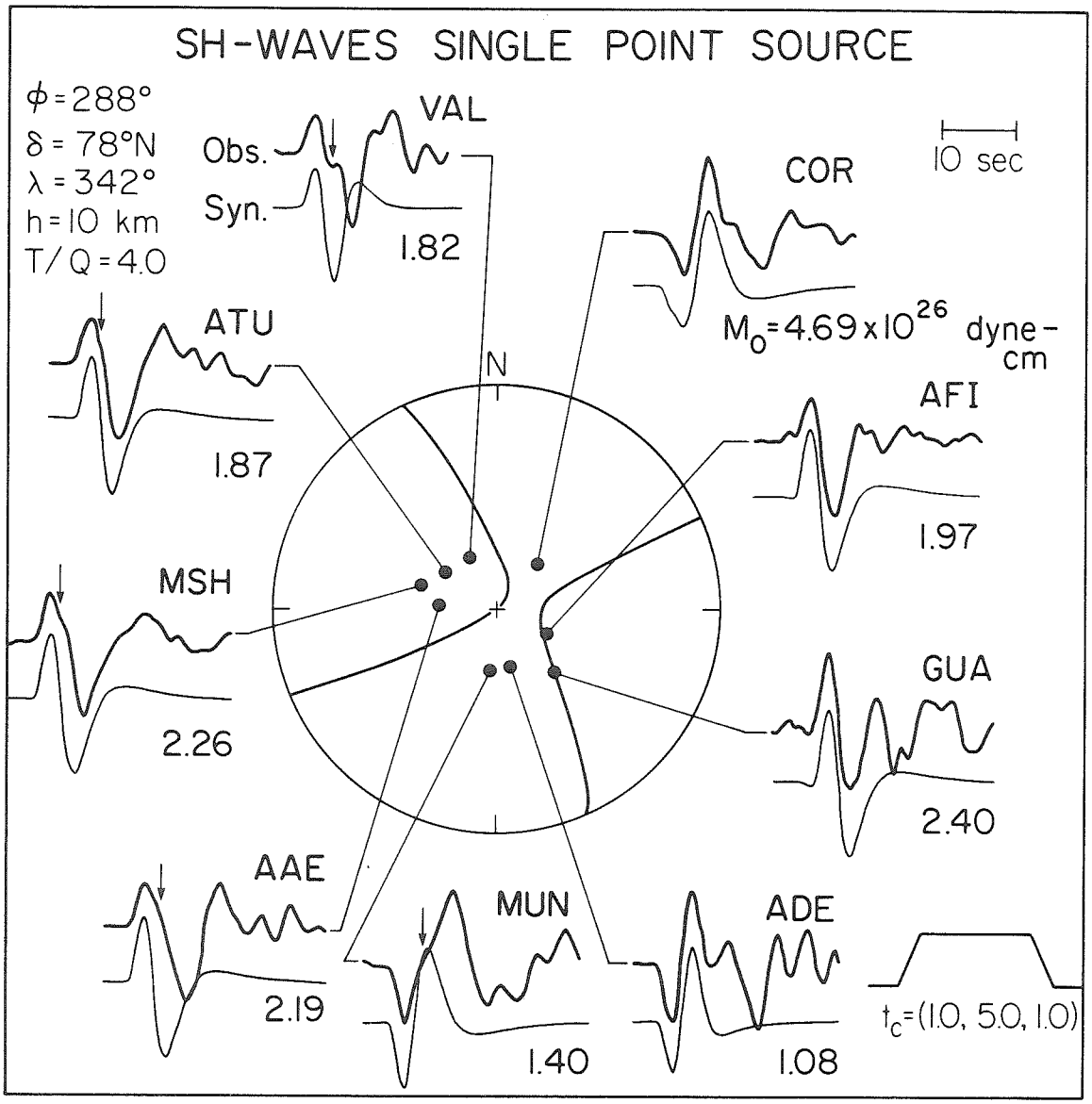

Figure 1-7. Comparison of observed and synthetic SH waves. Synthetics are computed for a point source at 10 km depth in a halfspace. T/Q ratio for this case is 4.0 sec. Far-field time function is a trapezoid of 7 sec duration. Arrows indicate second arrival observed at several stations. Other notation is the same as Figure 1-6.

reasonable and that a point source is a good approximation for this earthquake at teleseismic distances. The seismic moment is found by matching the absolute amplitudes of the observed records to the amplitudes of the synthetics.

There are features of the waveforms, however, which suggest that the simple point source model may not be adequate. Note that observed P waves recorded at stations with easterly azimuths (GUA, PMG, RIV, MUN) tend to be longer in duration than the corresponding synthetics (Figure 1-6) while at stations to the west (AAE, MSH, IST, ATU), the synthetics are longer than the observed data. This can best be seen by comparing the width of the large upswing pulse at RIV and ATU, as examples. This pulse is primarily the sP ray. At RIV, the observed pulse width is much broader than the synthetic while the opposite is true at ATU. To anticipate later results, this azimuthal pattern of P-wave duration can be explained by fault propagation from the epicenter to the northwest.

The SH waves (Figure 1-7) also show an azimuthal variation. There is good agreement between observed and synthetic waveforms at eastern stations (ADE, GUA, AFI, COR). At western stations, however, the observed SH waveforms are somewhat long compared to the synthetics. The anomalously long duration of the observed SH waves at western stations (VAL, ATU, MSH, AAE, MUN) seems to be due to a second arrival which comes in on the first downswing, about 10 sec into the record (indicated by arrows in Figure 1-7). The arrival is especially prominent at station VAL, while at MUN, the arrival causes severe distortion of the waveform. At stations AAE, MSH and ATU, the arrival is seen as a

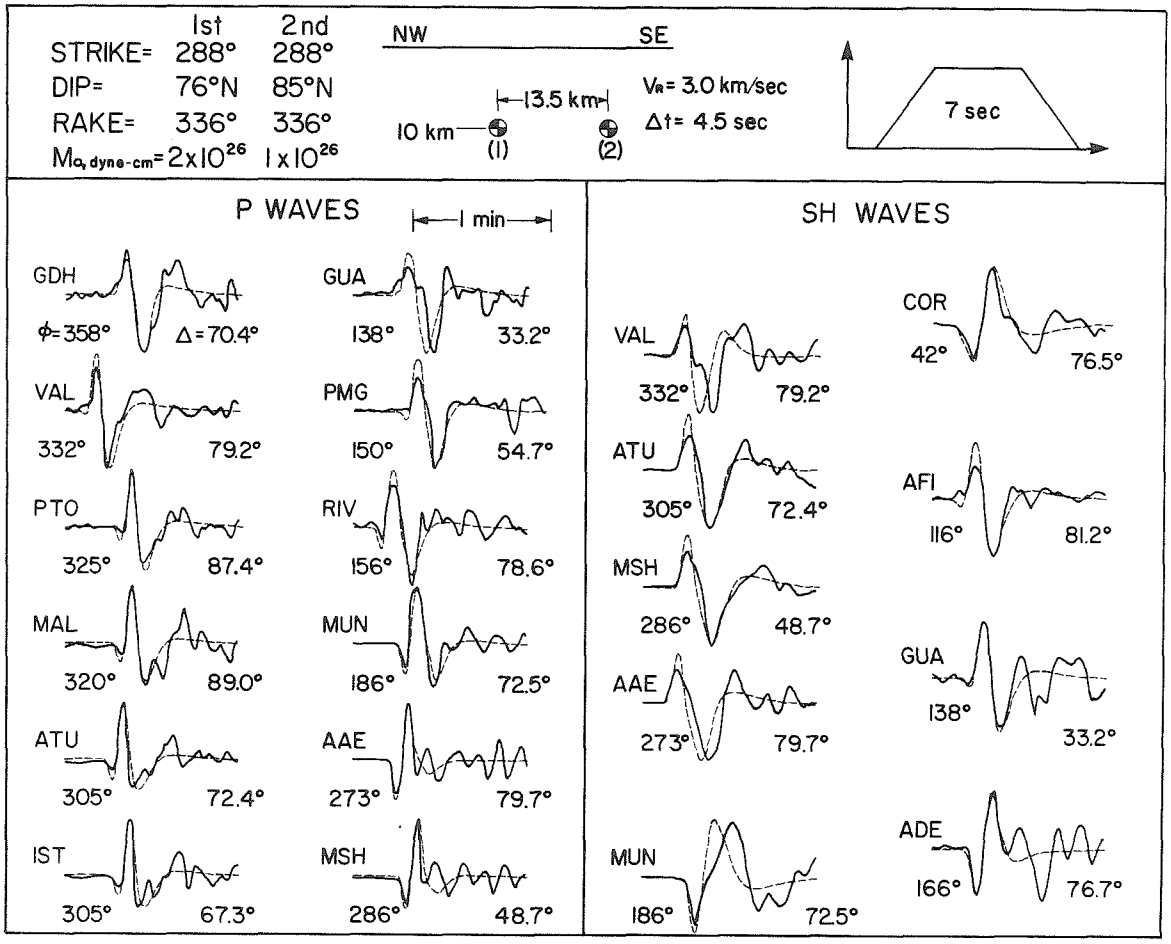

Figure 1-8. A model incorporating two point sources of radiation. The secondary source is one-half the size of the main source and is located 13.5 km to the southeast. The small star labeled (2) in Figure 1-4 indicates the location of the secondary source.

shoulder on the first downswing and greatly lengthens the pulse. No such arrival can be seen at the eastern SH stations (COR, AFI, GUA, ADE) nor is the arrival apparent in the P waves.

A possible explanation for this second arrival is the existence of a second source of radiation which occurred southeast of the original epicenter at a slightly later time. The position of this secondary source to the east or southeast would explain why the phase is visible at western stations but not at eastern stations where it is hidden in the SH pulse from the main source. Figure 1-8 shows a model for the Haicheng earthquake which consists of two such sources: the main source located at the teleseismic epicenter and a smaller, secondary source of radiation located 13.5 km southeast of the first and delayed in time 4.5 sec relative to the main source (see Figure 1-4). While this model improves the fits to the SH waves at ATU and MSH, it does not reproduce the SH waveforms observed at VAL or MUN nor are any P wave fits improved. The location of the mainshock epicenter near the southeast end of the aftershock zone indicates that the main part of rupture propagation was towards the northwest. While it is likely that there was faulting southeast of the epicenter (as indicated by surficial effects, Raleigh et al., 1977), this part of the fault was probably not a major contributor to the teleseismic radiation. Also, the fact that the second source is not observable in the P waves at western stations suggests that some other factor is affecting the SH waves at western stations.

An alternative explanation for the second arrival at western SH

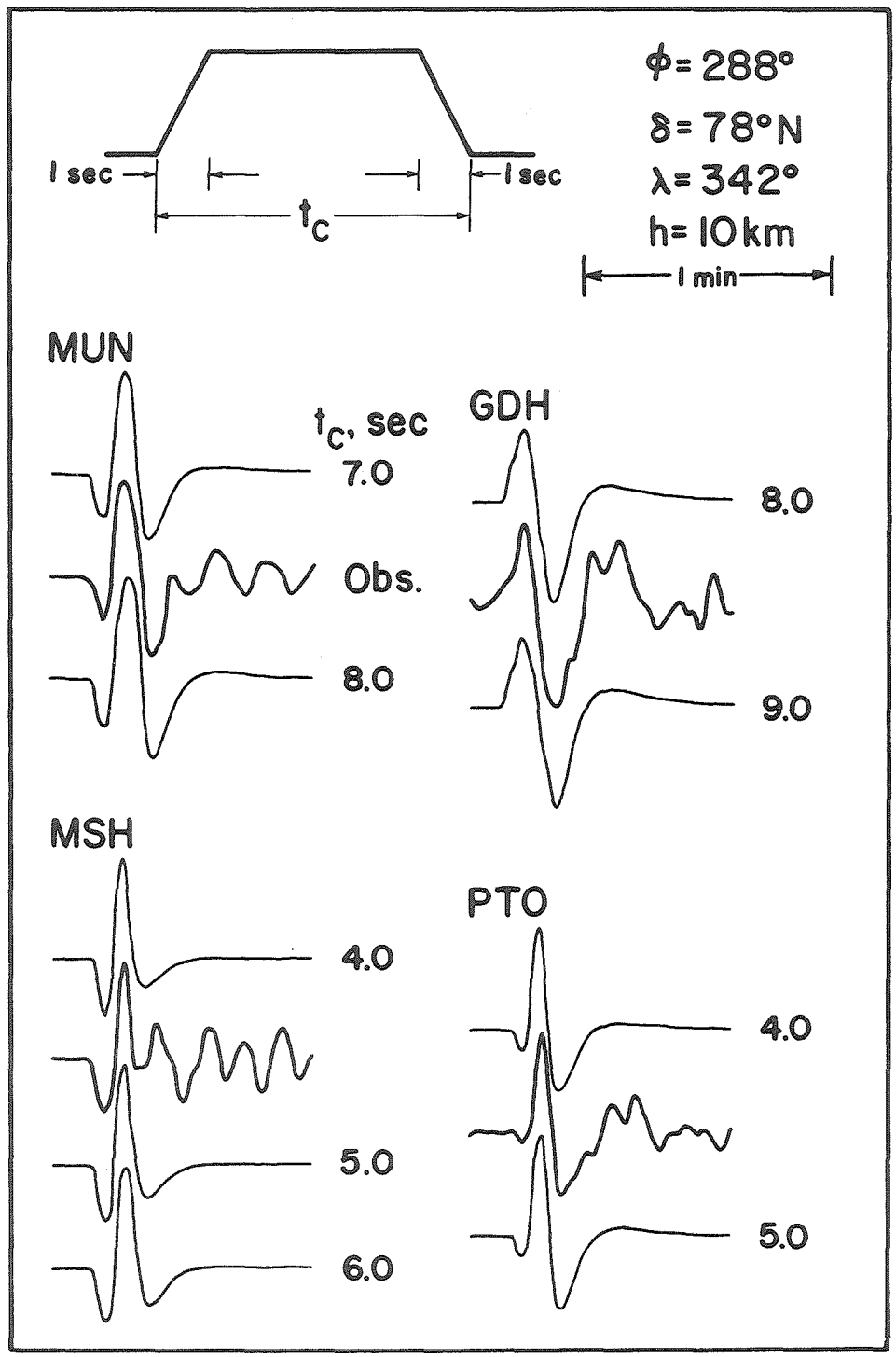

Figure 1-9. Comparison of observed P waves to synthetics computed using trapezoidal time functions of variable duration. Numbers after the synthetics give the total duration in sec.

stations is near source structural complications. Non-horizontal structures in the sedimentary basin to the west of the epicenter (Figure 1-3) could cause contamination of the SH records by P-SV contributions converted at the interface between the sediments and bedrock (Langston, 1977; Hong and Helmberger, 1978). To the east, there is no sedimentary basin and hence the SH records radiated in this direction are not disturbed. Such structures would not severely affect the first 10-20 sec of the P wave, the portion being modelled.

It was noted above that the P-wave duration seems to vary with azimuth in a regular way. Either a nonsymmetrical source time function or azimuthal variation of anelastic attenuation might account for the observations. Trial models using different values of T/Q showed that the variation of P-wave duration could not be explained with any reasonable T/Q ratios. In addition, the variation seems to be quite regular: short durations recorded to the west, long durations to the east. Perhaps the simplest way to account for these observations is by means of a propagating fault which would lead to the observed azimuthal variation in the apparent teleseismic P-wave time function.

To model a propagating source, a set of synthetics for each station was computed for time functions with durations ranging from 4.0 to 11.0 sec; for each set, the source depth and fault mechanism were kept fixed. At each station, a synthetic was chosen which best fit the observed record. Note that for the point source model (Figure 1-6), a single time function was used for all the records. For the propagating source case, the time function was variable from station to station.

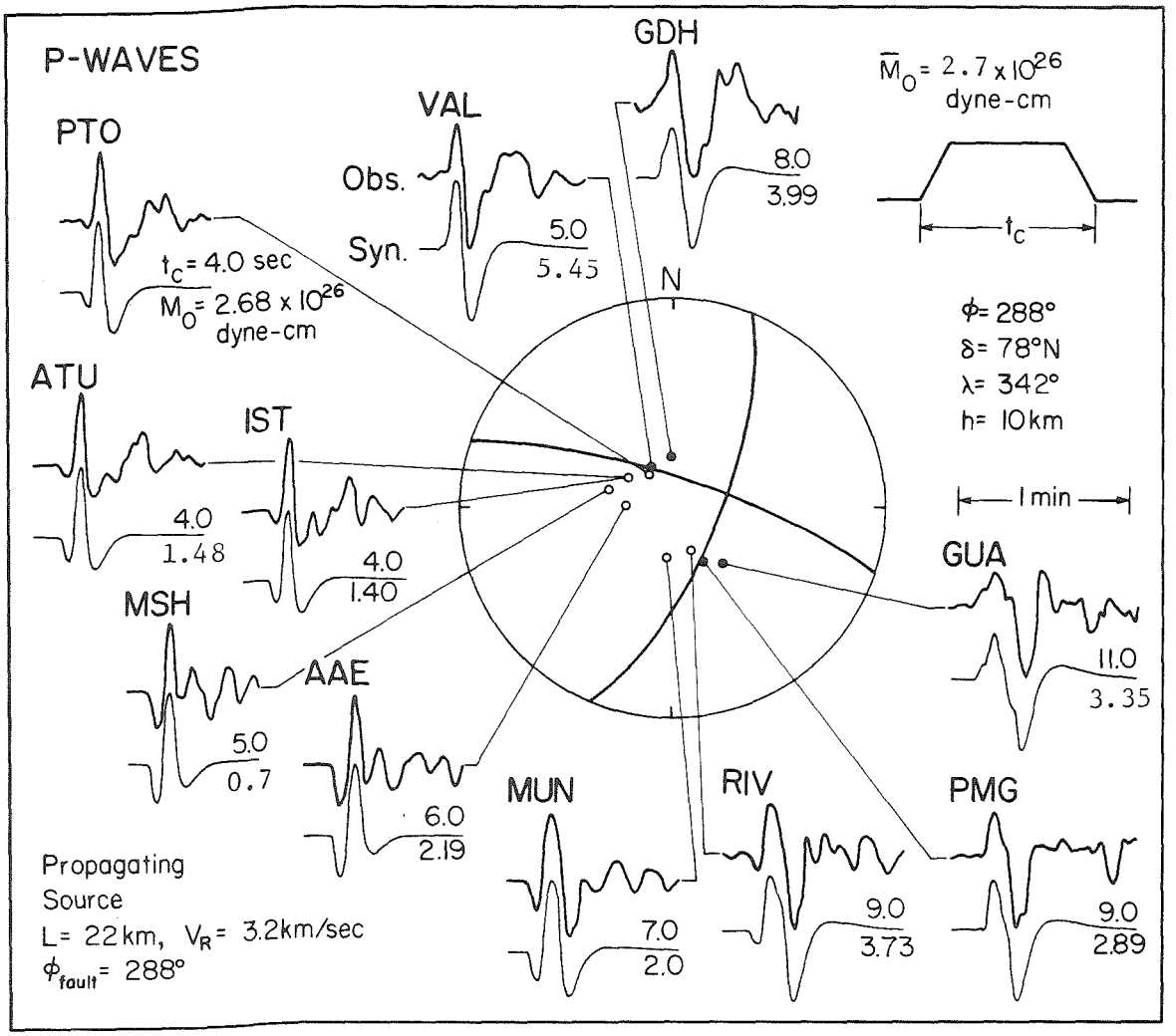

Figure 1-10. Comparison of observed P waves to synthetics for a propagating source. The duration, t_c, of the far-field time function (upper number after each synthetic) is different for each station. Other notation is the same as Figure 1-6.

Examples of the fitting process at several stations are shown in Figure 1-9.

The observed P waves along with the best fitting synthetics are shown in Figure 1-10. Note that the duration of the synthetic time function (the upper number after each synthetic) varies with azimuth and is shorter for P waves at western stations (VAL, PTO, ATU, IST, MSH) than at eastern stations (GDH, GUA, PMG, RIV, MUN). In general, the fit of the synthetics to the observed records is excellent. Even relatively minor details of the records are reproduced by the synthetics. The average seismic moment for this model is 2.72×10^{26} dyne-cm (Figure 1-10).

The variation of apparent P-wave time function with azimuth can be easily interpreted as the effect of a propagating source. The apparent duration of the faulting process at any azimuth from a unilaterally propagating fault can be expressed as:

$$t_c = (L/V_R) - (L/c)\cos\theta$$

where: V_R = fault rupture velocity

L = fault length

c = wave velocity in source region

θ = angle between rupture direction and ray vector

Using this relationship, we can interpret the observed variation of the time function with azimuth as an effect of a horizontally propagating fault as shown in Figure 1-11. Here the data are the observed P-wave time function durations (solid circles) for each station plotted versus azimuth. The solid line connects theoretical values (open circles)

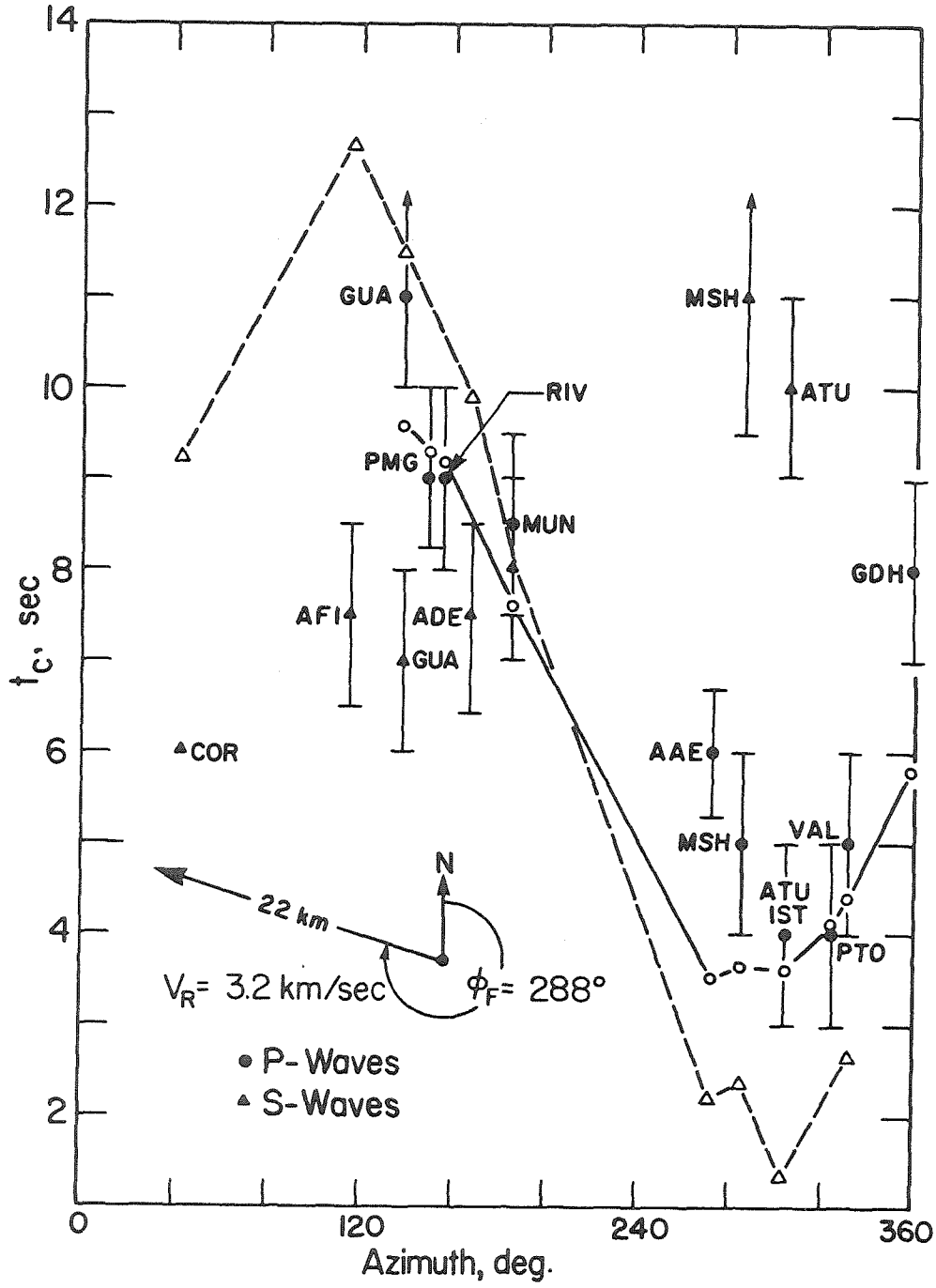

Figure 1-11. Observed time function duration plotted versus azimuth for P waves (closed circles) and SH waves (filled triangles). Open circles and triangles are theoretical time function durations for a fault propagating 22 km to the northwest at 3.2 km/sec. Solid and dashed lines show the overall form of the theoretical pattern. Error bars are estimated in the manner illustrated in Figure 1-9.

computed using the above equation with V_R = 3.2 km/sec, L = 22 km, c = 6.0 km/sec and fault azimuth of 288°. Since the rupture is assumed to propagate horizontally and the variation of ray take-off angle with distance is small at the ranges used (less than 15°), we can plot the points as a function of azimuth. The agreement between the theoretical and observed values for P waves is quite good.

The same procedure was applied to the SH waves with poor results, as might be expected from simply looking at the observed records. In Figure 1-11, the closed triangles are the observed SH-wave time functions and the dashed line connects theoretical values (open triangles) calculated with the source model described above. The observed SH pattern is exactly opposite the predicted pattern.

Discussion

In the previous section, it was shown that the P waves radiated by the Haicheng earthquake could be explained quite well by a northwesterly propagating point source. Despite the gross simplification of approximating the earth by a halfspace, synthetic seismograms matched the observed P waves in considerable detail. Agreement between synthetic and observed SH waves was much poorer. One possibility is that the complexities of the western SH waves (VAL, ATU, MSH, AAE, MUN) are due to a secondary source of radiation located to the southeast of the main epicenter. Another plausible explanation is complex interference and mode conversion effects in the deep sedimentary basin west of the earthquake. Based on the limited data at hand, it is not

possible to conclusively assess the relative importance of either structure or source complexities on the observed waveforms.

Perhaps more disturbing is the relatively short durations of SH waves recorded at eastern stations (COR, AFI, GUA, ADE). At these azimuths, the propagating fault model predicts SH waves of long duration. Intuition might suggest that earth structure would lengthen waveforms and make them more complex, but it is hard to imagine a structural configuration which would decrease the duration of a pulse. One might appeal to a drastic change in fault mechanism as propagation proceeded. For instance, the mechanism could change from predominantly strike-slip in the southeast, near the epicenter, to more dip-slip in the northwest. This would preserve the observed P-wave and SH-wave first motions, but would reduce overall S-wave radiation relative to P for the latter part of fault propagation. We might expect to see this effect reflected in the observed surface wave mechanism since the period of surface waves is considerably longer than the time of the whole faulting process. However, the surface wave mechanism reported by Stewart et al. (1976) is consistent with the mechanism determined from body waves (Figure 1-5) indicating that there was no appreciable change in fault orientation during rupture. Also, aftershock focal mechanisms over the length of the zone (Gu et al., 1976) are, for the most part, consistent with the mechanism determined for the mainshock (Figure 1-5). Gu et al. (1976) report several aftershocks with nodal planes similar to those of the mainshock but with reversed polarity. In contrast to the mainshock and the majority of the aftershocks which are left-lateral,

these right-lateral events are interpreted by Gu et al. (1976) as the response of the fault zone to overshoot during the mainshock. Difficulties in interpreting the S-wave records preclude an unequivocal observation of fault propagation in the body waves of the Haicheng earthquake. The P-wave data, however, strongly suggest that this effect is present in the seismograms. The value of the propagating source model is that while it is a simple extension of the point source case, it leads to visible improvement in the synthetic P waves.

The 40 km length of the aftershock zone northwest of the epicenter (Figure 1-4) is somewhat longer than the 22 km long fault predicted by the propagating source model. An M_S = 4.1 aftershock (time marked on Figure 1-4) occurred near the northwest end of the aftershock zone within two hours of the mainshock. This suggests that the extra 15 km of aftershocks were triggered soon after the main event and are not the normal slow diffusion of aftershocks with time (Mogi, 1968). Perhaps some kind of aseismic creep event propagated along the fault. Slow deformation during the main earthquake would probably not radiate significant energy in the body wave frequency band but might affect long-period surface waves (e.g., Kanamori and Stewart, 1976). However, the seismic moment computed by Stewart et al. (1976) from surface waves is 3×10^{26} dyne-cm, the same as the moment computed from body wave amplitudes. Perhaps the extra 10 to 15 km of aftershocks were triggered by an aseismic rupture event after the main episode of brittle faulting recorded by the body and surface waves. Burdick and Mellman (1976) report similar observations for the Borrego Mountain, California

earthquake. They show that the aftershock zone is considerably larger than the region of the fault which radiated the body waves.

The average dislocation, D_o, of the Haicheng earthquake can be estimated from the formula for seismic moment, M_o (see Kanamori and Anderson, 1975): $M_o = \mu L w D_o$ where L is the fault length, w is the fault width and μ is the rigidity (= 3.6×10^{11} dynes/cm^2). The average value for M_o is 2.7×10^{26} dyne-cm (Figure 1-10), L is about 25 km and w is estimated to be 12 km from the depths of aftershocks. Using these values, D_o is about 2.5 meters. The stress-drop for a strike-slip fault is given by the formula (e.g., Kanamori and Anderson, 1975): $\Delta\sigma = (2/\pi)\mu(D_o/w)$ and is found to be 48 bars. Gu et al. (1976) estimate M_o and $\Delta\sigma$ from field observations. Maximum horizontal offset of 55 cm was measured at Shiaokushan District (Hsu, 1976). The aftershock distribution, which presumably outlines the maximum size of the fault plane, was taken to be 70 km by 20 km. Using these values, Gu et al. (1976) determined the moment and stress drop to be 2.1×10^{26} dyne-cm and 4.8 bars respectively. The discrepancy between the value of D_o estimated in this chapter and the value computed by Gu et al. may be due to the dying out of the dislocation as it reached the surface. Ground cracking and related phenomena were reported in only one locality (Figure 1-2). The low stress drop value computed by Gu et al. (1976) is a consequence of the low value of D_o they use. The value of stress drop (48 bars) computed in this paper is well within the range of stress drops compiled by Kanamori and Anderson (1975, their Figure 1) and is typical of intraplate earthquakes.

Regarding the prediction of the Haicheng earthquake, it seems that none of the parameters estimated in this paper indicate abnormal source behavior. In particular, the stress drop is within the range reported for other shallow earthquakes and the seismic moment computed from body waves is in excellent agreement with the surface wave moment. It is worth restating, however, several unusual features of this earthquake. First, the fault which broke during the earthquake was transverse to the regional tectonic and structural trends. Second, there was considerable aftershock activity within hours of the mainshock apparently not directly associated with the main episode of faulting. Third, it is somewhat surprising that there was only minor surface faulting considering the large size and shallow depth of the earthquake. At present, it is simply not clear whether these phenomena are related to the tilting and seismicity which preceded the Haicheng earthquake.

Chapter Two

Teleseismic Observations of the May 6, 1976 Friuli, Italy Earthquake Sequence

Introduction

One of the most damaging earthquakes in the European area in recent years struck the Friuli region of northeastern Italy on May 6, 1976. The mainshock caused heavy loss of life and a great amount of property damage and was followed by an aftershock sequence of unusual severity.

The seismograms written by the Friuli earthquake and its aftershocks present an opportunity to understand the dynamics of faulting in a continental environment. The mainshock and several aftershocks were well recorded teleseismically. Moreover, accelerograms were obtained for the mainshock and aftershocks from stations in the epicentral area. This data set provides an opportunity to view the earthquake in four spectral bands: long-period surface waves, long and short-period teleseismic body waves and near-field ground displacement. In addition, the large magnitude of several aftershocks relative to the mainshock is a feature of this earthquake sequence that is not commonly observed in other seismic zones. From a tectonic point of view, knowledge of the mechanism of the earthquake is important in elucidating the mechanics of the collision between Africa and Eurasia.

The next three chapters present an interpretation of the tectonics and source processes of the mainshock and two aftershocks of the Friuli

earthquake sequence. The three earthquakes occurred in northeastern Italy: the mainshock on May 6, 1976 (20h 00m GCT) and both aftershocks approximately four months later, on September 15, 1976 (03h 15m and 09h 21m). These aftershocks were the culminating events in a dramatic increase in seismic activity which began on September 11 and were by far the largest aftershocks of the sequence, approaching the mainshock in size and occurring within a few kilometers of the mainshock. This chapter discusses various features of the source properties of the mainshock and aftershock of September 15, 1976 (09h 21m) which can be inferred from teleseismic long-period body wave and surface wave data. Fault mechanism, source depth and nature of fault rupture can be deduced from body waves while additional data on the long-period nature of the source are available from surface waves. In Chapter Three, teleseismic short-period P waves and local strong-motion records are examined to elucidate details of the faulting process. The relation between source models, aftershock energy release and tectonics is discussed in Chapter Four.

Tectonic Setting

The Friuli-Venezia-Giulia Region of northeastern Italy extends from Austria on the north to the Adriatic Sea on the south and is bordered on the east by Yugoslavia. The region can be divided into several distinct topographic elements (Martinis, 1975). Along the Austrian border are the Carnic Alps, composed principally of Paleozoic rocks. South of the Carnic Alps are the largely Mesozoic Tolmezzo Alps in the western part

Figure 2-1. Geological and plate tectonic setting of the Friuli earthquake sequence. The upper figure shows the geology after Gwinner (1971). The star near the center of the figure shows the ISC location of the mainshock. The heavy dashed line along the Gail River is the Periadriatic Lineament (see text). Geological units are: (1) Quaternary; (2) Miocene molasse, (3) Eocene-Oligocene flysch, (4) Cretaceous carbonate, (5) Jurassic, undivided, (6) middle and upper Triassic, (7) Triassic and Permian, (8) Paleozoic of the Carnic Alps, (9) quartz phyllite, (10) crystalline rocks of the eastern Alps, (11) thrust fault. The lower figure shows the plate tectonic interpretation of Lort (1971) and McKenzie (1972). The dashed line represents the inferred southwestern boundary of the Apulian plate. Arrows indicate the direction of plate motion.

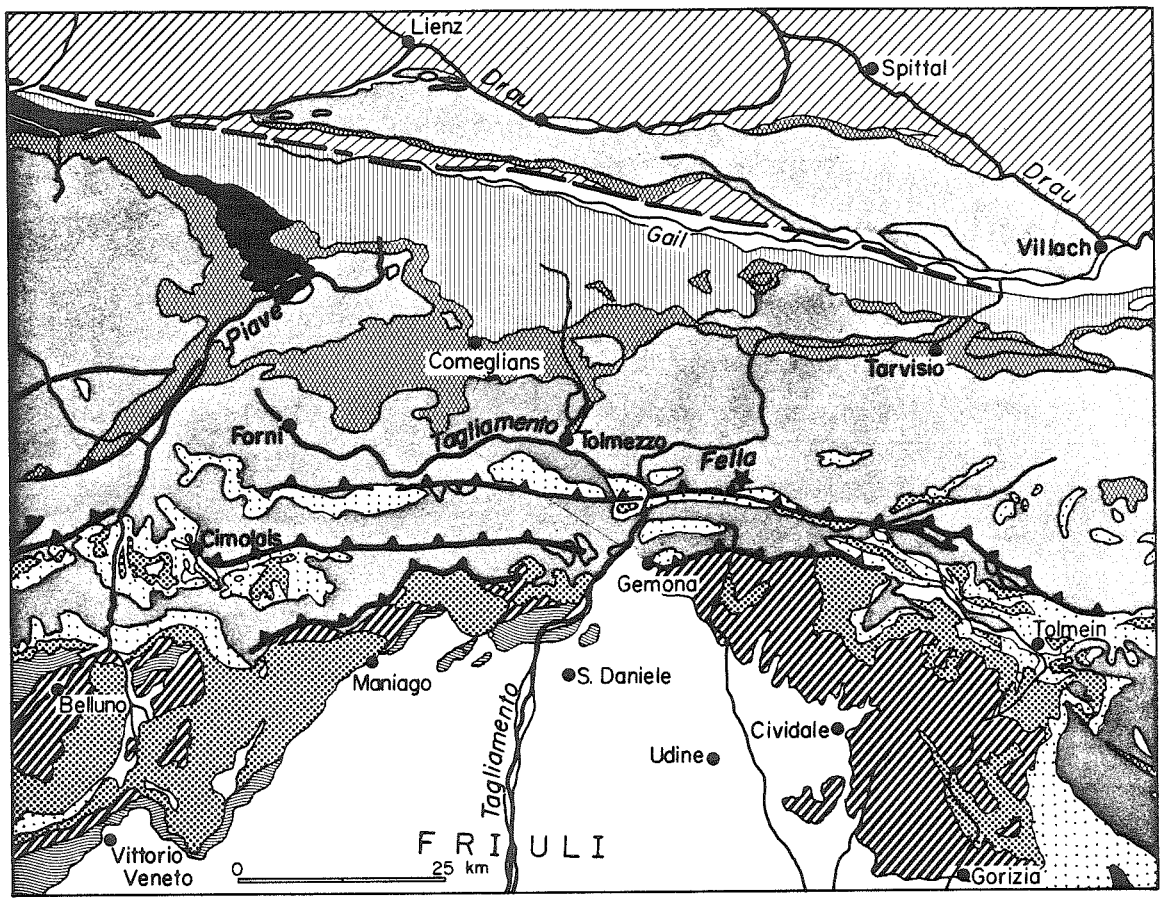

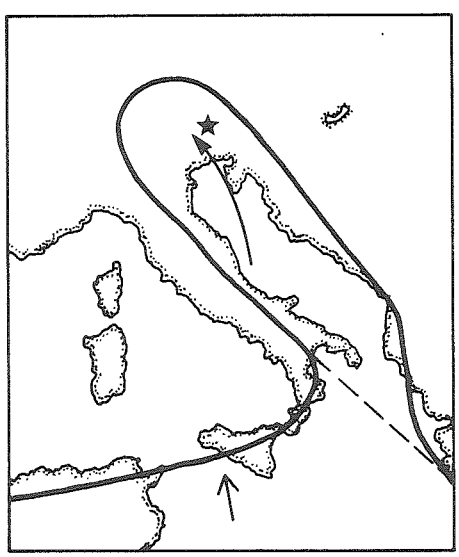

1
2
3
4
5
6
7
8
9
10
11

of the area and the Julian Alps in the east. South of the latitude of the Tagliamento River, the mountains become lower in elevation. These ranges, known as the Pre-Alps, are underlain by Cenozoic flysch and molasse deposits. Between the Pre-Alps and the Adriatic Sea is the extensive Friuli Plain of Quaternary sediments. To the east, in Yugoslavia, the Dinaric Alps trend southeastward down the Balkan Peninsula.

The Carnic, Tolmezzo and Julian Alps, together with the Pre-Alps, constitute the Southern Alps in a geological sense (Angenheister et al., 1972). The Southern Alps are separated from the Eastern Alps by an important structural boundary, the Periadriatic Lineament (heavy dashed line in Figure 2-1), which forms the northern boundary of the Carnic Alps (Angenheister et al., 1972; Martinis, 1975). In general, the Southern Alps have suffered less metamorphism and tectonism than the rocks north of the Periadriatic Line (Angenheister et al., 1972). In the Friuli region, the structural grain changes from northwest-southeast Dinaride trends near the border with Yugoslavia to more east-west trending structures of the Southern Alps in the west.

Throughout much of the Mesozoic, shallow water deposition of calcareous rocks occurred through the Friuli region (Martinis, 1975) although the presence of deep basins is indicated by pelagic sedimentation. Beginning in early Cenozoic times, the tectonic environment became more unstable. Eocene flysch deposits, which now outcrop at the edge of the Friuli plain, mark the beginning of the Alpine orogeny which culminated in the Upper Miocene and Pliocene (Amato

et al., 1976). A subaerial depositional environment has prevailed over the Friuli region from the Oligocene to the present.

The most important structural feature in the epicentral area is the so-called "Periadriatic Thrust" (Amato et al., 1976; Martinis, 1975) which is a complex zone of northward dipping thrust faults (Figure 2-1). The Periadriatic Thrust is not to be confused with the Periadriatic Line, (heavy dashed line in Figure 2-1) mentioned above, which structurally separates the Eastern and Southern Alps. In addition to the faults which are known in outcrop, a number of similar structures have been found in the subsurface of the Friuli Plain on seismic reflection profiles (Amato et al., 1976).

In a larger context, McKenzie (1972) suggests that the Adriatic Sea and the coastal areas of Italy and Yugoslavia form a tongue of the African plate which is underthrusting Eurasia in northeastern Italy and Yugoslavia. The African-Eurasian plate boundary is inferred from seismicity (Papazachos, 1973) to extend from Tunisia, through Sicily and the toe of Italy, up the Italian Peninsula, across the southern Alps and down the coast of Yugoslavia (Figure 2-1). Lort (1971), on the other hand, suggests that the Adriatic Sea is a separate microplate, the Apulian plate, which may move independently of the larger plates. Except for the existence of a plate boundary across the mouth of the Adriatic Sea, the interpretations of Lort and McKenzie are similar. In both cases, compressional tectonics would be expected in northeastern Italy and adjacent Yugoslavia.

Table 2-1. Significant Earthquakes of the Friuli Region

No.	Year	Month Day	h m	Latitude ^{o}N	Longitude ^{o}E	Depth (km)	m_b	M_S
	1348	Jan. 25*		46.5	13.4			
	1511	March 26*		46.2	13.6			
	1928	March 27*	08 32	46.41	13.08	25		5.8
	1936	Oct. 18*	03 10	46.04	12.40	15		5.7
	1975	March 24	02 33	46.29	13.13	21		
0	1976	May 6	19 59	46.201	13.262	33N	4.5	
1		May 6	20 00	46.36	13.28	9	6.0	6.5
13		May 11	22 44	46.27	12.99	11	5.2	
36		Sept. 11	16 31	46.28	13.16	16	5.2	5.5
37		Sept. 11	16 35	46.30	13.20	20	5.3	5.4
42		Sept. 15	03 15	46.30	13.20	10G	5.7	6.0
46		Sept. 15	09 21	46.32	13.13	17	5.4	5.9
	1977	Sept. 16	23 48	46.27	12.97	25	5.1	5.1

Data from Preliminary Determination of Epicenters, Monthly Listing

*Data from Ambraseys (1976)

Seismicity

Northern Italy, including the Friuli region, was characterized as an area of low to moderate seismicity by Gutenberg and Richter (1954), although Karnik (1971, p. 184) was impressed with the activity in the Friuli region. Reports of historical earthquakes before 1900 have been collected by Ambraseys (1976a) and Karnik (1971). The most notable earthquakes were the shocks of 1348 and 1511. While the amount of damage due to these shocks was severe, both authors believe that neither event exceeded magnitude 6-3/4. The great damage caused by earthquakes in this region is due not so much to the large magnitude of the events but more because of poor construction techniques (Ambraseys, 1976a). The seismic activity of Friuli can be characterized by the occurrence of infrequent moderate earthquakes ($M_S \leq 7$) separated by long quiescent periods, with only minor seismicity.

According to Ambraseys (1976a), there have been only two earthquakes since 1900 with surface wave magnitude greater than 5.0 prior to the 1976 events (Table 2-1). An $m_b = 4.2$ (USGS) shock occurred on March 24, 1975 and was followed by a series of shocks which were felt in the Tolmezzo region through April 25 (International Seismological Center). The ISC does not report any further events in the epicentral area until the foreshock of the Friuli earthquake on May 6, 1976.

The mainshock (May 6, 1976, 20h 00m) was preceded by an $M_L = 4.5$ foreshock at 19h 59m and followed by numerous aftershocks which decreased in magnitude and frequency until September, 1976. The normal decay of the aftershock sequence was shattered by two pairs of

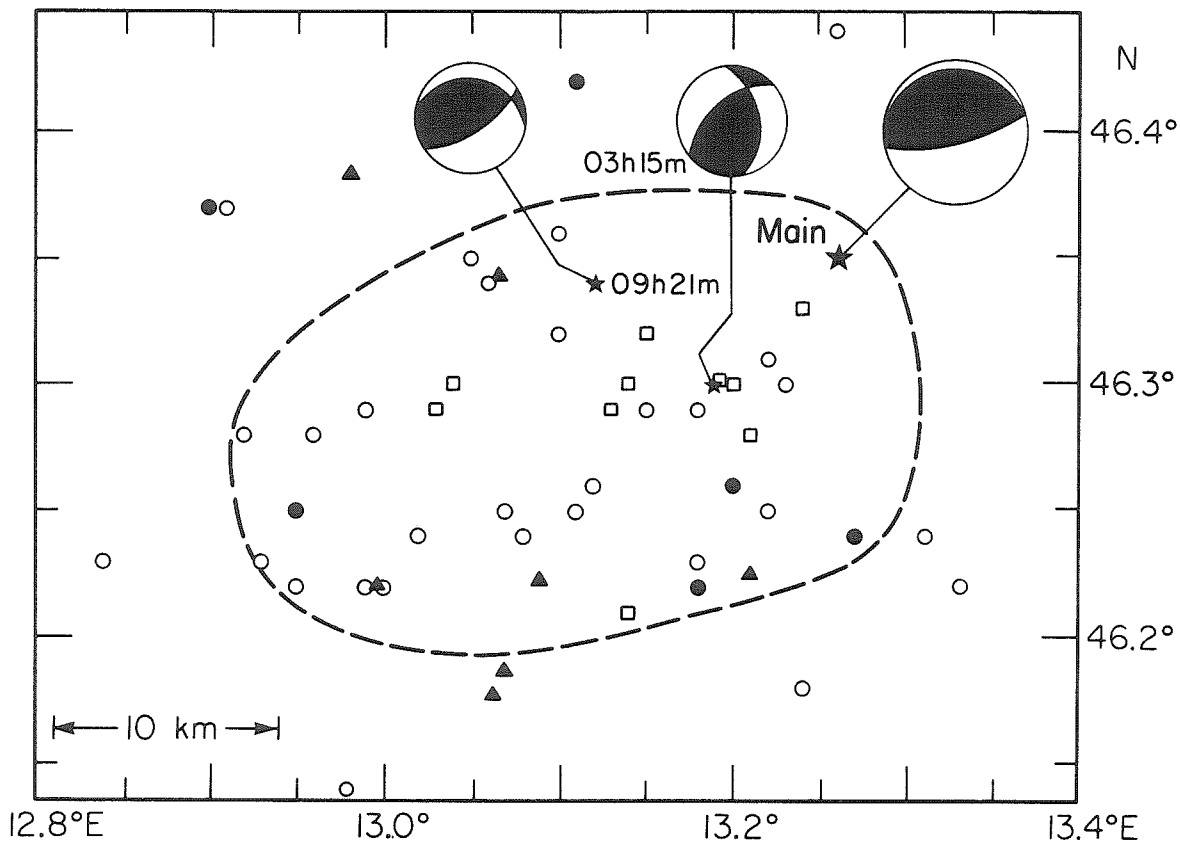

Figure 2-2. Epicenters of the mainshock and larger aftershocks of the Friuli earthquake sequence as reported by the ISC. Large star indicates the mainshock. Closed circles represent aftershocks which occurred within the first twenty-four hours and open circles are later aftershocks up to September 11. Smaller stars are epicenters of the two largest earthquakes on September 15. Open squares are aftershocks of these events. Focal mechanisms are shown with compressional quadrants shaded. Heavy dashed line denotes the approximate limit of aftershock concentration. Triangles are accelerograph stations.

strong earthquakes on September 11 (16h 31m and 16h 35m) and September 15 (03h 15m and 09h 21m). Seismic activity declined markedly after these earthquakes, although a magnitude 5.1 shock occurred one year later, in September 1977. Table 2-1 is a summary of the larger earthquakes of the Friuli area.

Unfortunately, there is some ambiguity concerning the location of the epicenter of the mainshock relative to the aftershock distribution. Table 2-2 gives the hypocentral determinations of various agencies (shown as stars in Figure 2-3). The ISC locations of the larger aftershocks are shown in Figure 2-2. While there is activity over a broad area, most aftershocks are concentrated within a roughly elliptically shaped region 30 km long by 18 km wide. Referring to Figure 2-3, note that most of the agencies place the mainshock near the eastern edge of the aftershock distribution (outlined by the dashed line), except Rome, which puts the epicenter in the center of the distribution. To see if there are any systematic differences between the Rome and ISC locations, the positions of several of the larger, and presumably better located, aftershocks as reported by each group are plotted in Figure 2-3. The arrows point from the ISC location to the Rome location. There seems to be no consistent shift of epicenters determined by one agency to the epicenters computed by the other.

To help resolve these discrepancies in locations, the mainshock and two aftershocks were relocated relative to a third aftershock. Note that the Rome and ISC epicenters of event 36 (September 11, 16h 36m) are quite close. This event was large and well recorded and was chosen as

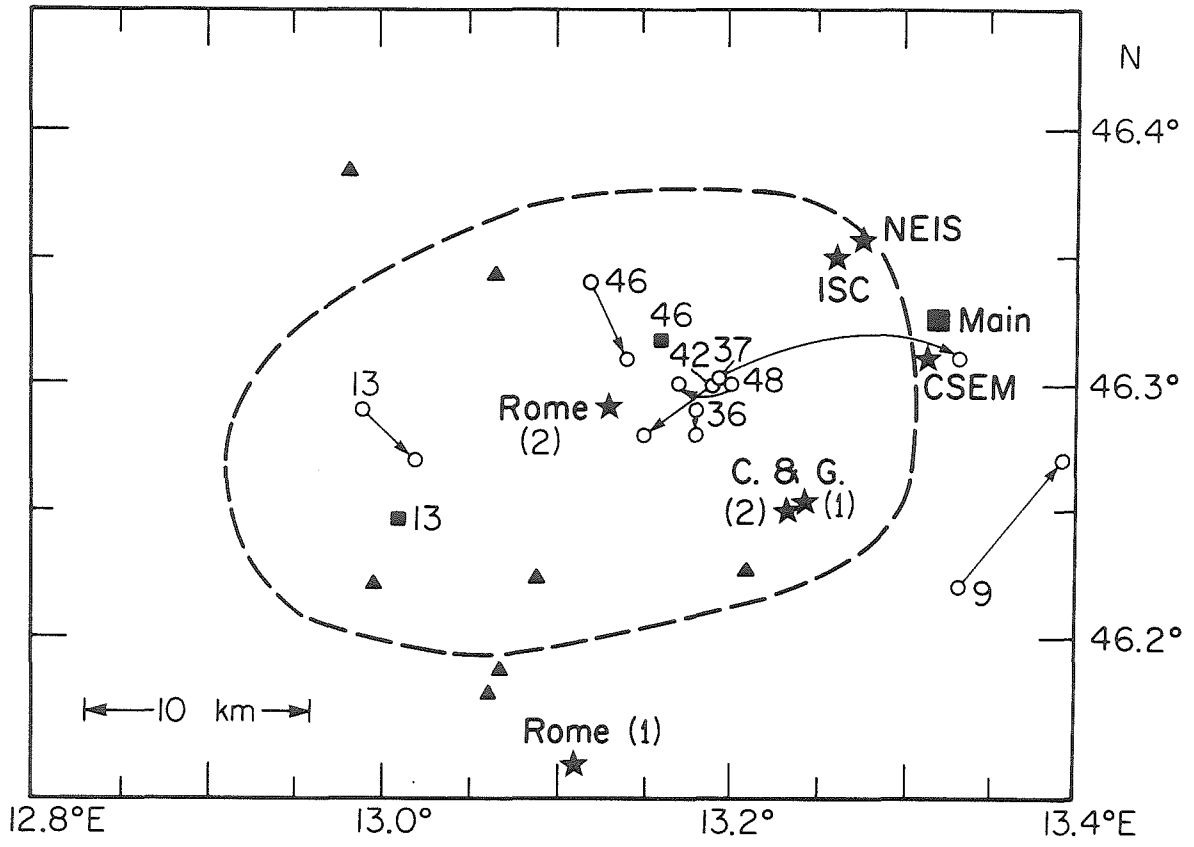

Figure 2-3. Locations of the mainshock and largest aftershocks. Mainshock epicenters determined by various agencies are indicated by stars (Table 2-2). Aftershock epicenters (numbers correspond to Table 2-1) calculated by ISC and Rome are indicated by open circles; arrows point from ISC location to Rome location. Filled squares indicate locations of mainshock and aftershocks 13 and 46 relative to aftershock 36 (see text).

Table 2-2. Mainshock Hypocenter Determinations

Agency	h	m	sec	Latitude ^{o}N	Longitude ^{o}E	Depth (km)	m_b	M_S	M_L
NEIS	20	00	11.6	46.356	13.275	9	6.0	6.5	
ISC			12.5	46.35	13.26	12	5.9		
Rome #1			12.2	46.15	13.11	26			6.2
Rome #2			8.6	46.29	13.13			Mag=6.4	
CSEM			14.7	46.31	13.31	10			
C.&G. #1			11.278	46.253	13.240	8.19			
c.&G. #2			12.585	46.250	13.231	9.995			

NEIS: National Earthquake Information Service, Preliminary Determination of Epicenters

ISC: International Seismological Centre, Edinburgh, Scotland

Rome: Instituto Nazionale di Geofisica, Roma

CSEM: Centre seismologique Europeo-Mediterranean

C.&G.: Console and Gasparini (1976)

the master event. Using the relative location method implemented by Chung and Kanamori (1976), the locations of the mainshock and aftershocks 46 and 13 were computed relative to the location of aftershock 36 (shown as boxes in Figure 2-3). There seem to be no gross errors in the method since in both cases, the relative location of the aftershocks are in the vicinity of the absolute locations determined both by Rome and by ISC. The relative location places the mainshock on the eastern edge of the aftershock distribution, nearer to the ISC location than to the epicenter determined by Rome.

There are several other points to be made about the aftershock distribution. First, the larger, first-day aftershocks (shown as solid dots in Figure 2-2) occur along the margins of the aftershock zone. Second, the September earthquakes (open boxes in Figure 2-2) occur within the aftershock zone of the main event. These observations are in agreement with the conclusions of a more complete study of aftershock locations by Cagnetti and Console (1977) who also show that the location of activity migrates during the course of the aftershock sequence. In Chapter Four, the temporal pattern of energy release during the aftershock sequence will be examined.

Data and Methods

A good set of WWSSN long- and short-period records is available for the mainshock and both aftershocks, although the long-period P waves for the 03h 15m event are obscured in many cases by the coda of an earlier teleseism. Stations used for body and surface wave analysis

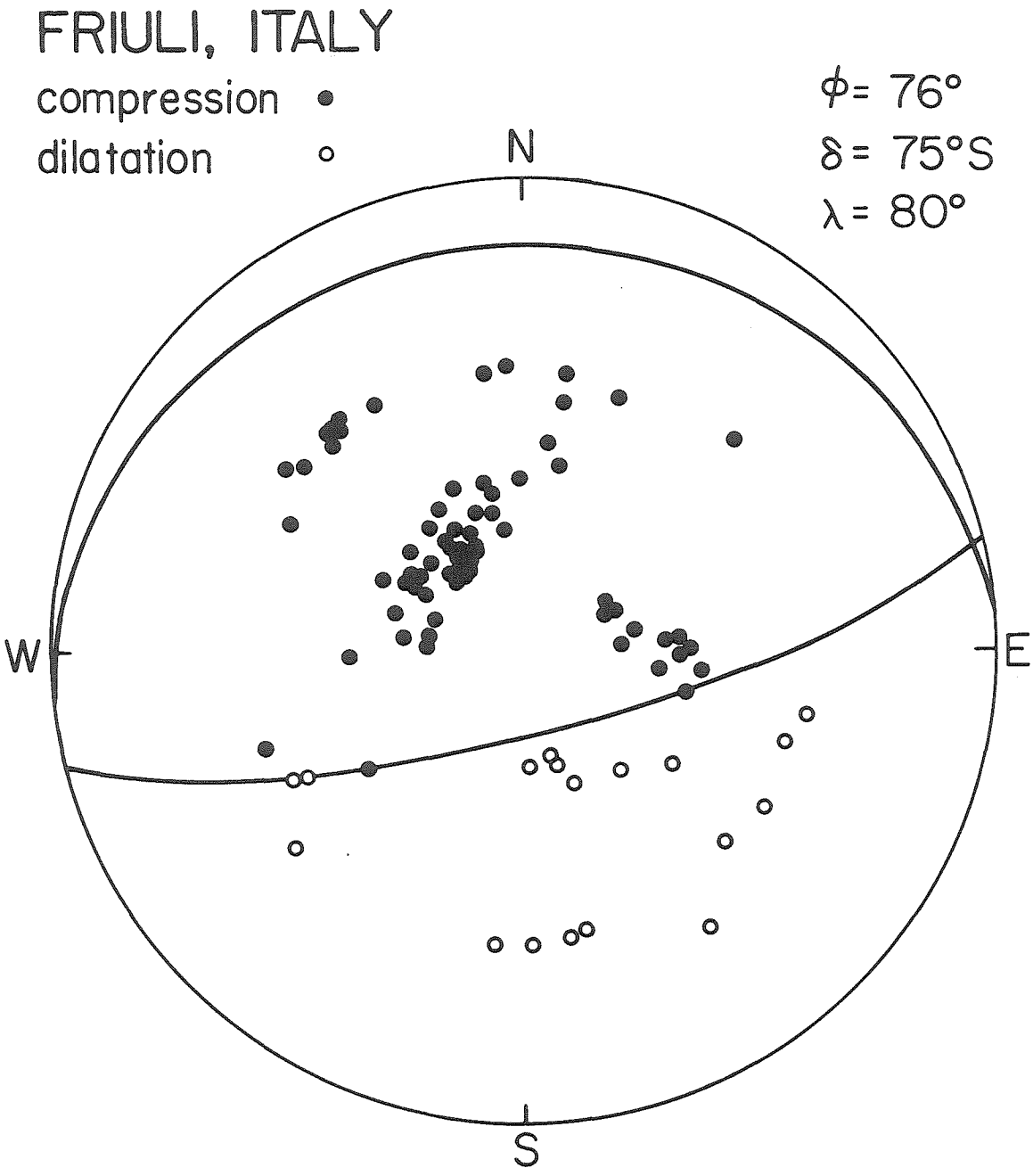

Figure 2-4. P-wave focal mechanism of mainshock (May 6, 1976). Data read on WWSSN long-period vertical seismographs and on other long-period stations in Europe and plotted on lower half of focal sphere. Shallowly dipping plane is constrained by S-wave data.

were chosen based on clarity of recording and absence of long-period noise. Distances and azimuths to each station are listed in Table 2-3. P-wave and Rayleigh wave portions of each seismogram were digitized on an electronic digitizing table and detrended and interpolated by computer. P and S waves were corrected for instrumental magnification and plotted at a uniform time scale. East-west and north-south components of the S waves were rotated to obtain pure SH and SV records. Rayleigh waves were digitized and interpolated within the group velocity window between 4.1 and 3.4 km/sec. They were then transformed to the frequency domain, corrected for instrument response, and equalized to a propagation distance of 90^{o}.

Long-Period Body Waves

The first step in computing synthetic body-wave seismograms is to determine the focal mechanism solution. P-wave first motions were read on long-period vertical seismographs of the WWSSN and other stations. For the mainshock (Figure 2-4), the available data define the steeply dipping nodal plane quite well, while the other plane is almost completely unconstrained.

In cases in which the orientation of one nodal plane is ambiguous, S waves can often be used to fix the location of the unknown plane. The technique of S-wave polarization is well known (e.g. Muller, 1977). In this paper, SV and SH synthetic seismograms were computed for various trial orientations and compared to the observed records. The trial mechanism which gives the most consistent fits is inferred to be the

Table 2-3. Station Data

Station	Delta (deg)	Azimuth (deg)	Back Azimuth (deg)	Station	Delta (deg)	Azimuth (deg)	Back Azimuth (deg)
AAE	43.1	141.5	334.2	KTG	29.6	336.8	125.9
ALQ	82.5	314.0	37.3	LON	79.3	330.5	29.8
ANP	83.7	59.8	318.7	LPB	96.0	252.7	43.6
ATL	71.4	299.1	46.4	MAT	83.8	41.5	325.3
BEC	59.6	286.4	51.7	MSH	35.7	89.4	301.0
BLA	66.5	299.8	48.8	MSO	76.3	325.8	34.5
BOG	84.9	271.5	44.0	NAI	51.8	149.4	339.4
BUL	67.6	164.4	348.6	NDI	52.4	86.0	308.2
CAR	75.7	270.4	44.7	PRE	73.0	165.9	349.2
CHG	73.7	79.6	314.1	QUE	44.3	91.9	307.0
COL	68.1	351.4	14.0	SHA	75.6	299.5	44.4
COR	81.6	330.3	28.7	SHI	34.7	104.7	309.8
DAV	99.9	68.6	319.5	SJG	69.8	275.4	46.5
DUG	81.3	321.3	34.4	SNG	83.0	86.8	315.9
GOL	78.3	316.4	38.3	TRN	71.7	266.4	44.7
HKC	81.3	66.8	316.6	WES	57.8	299.4	54.5
KBS	32.7	359.6	178.5				

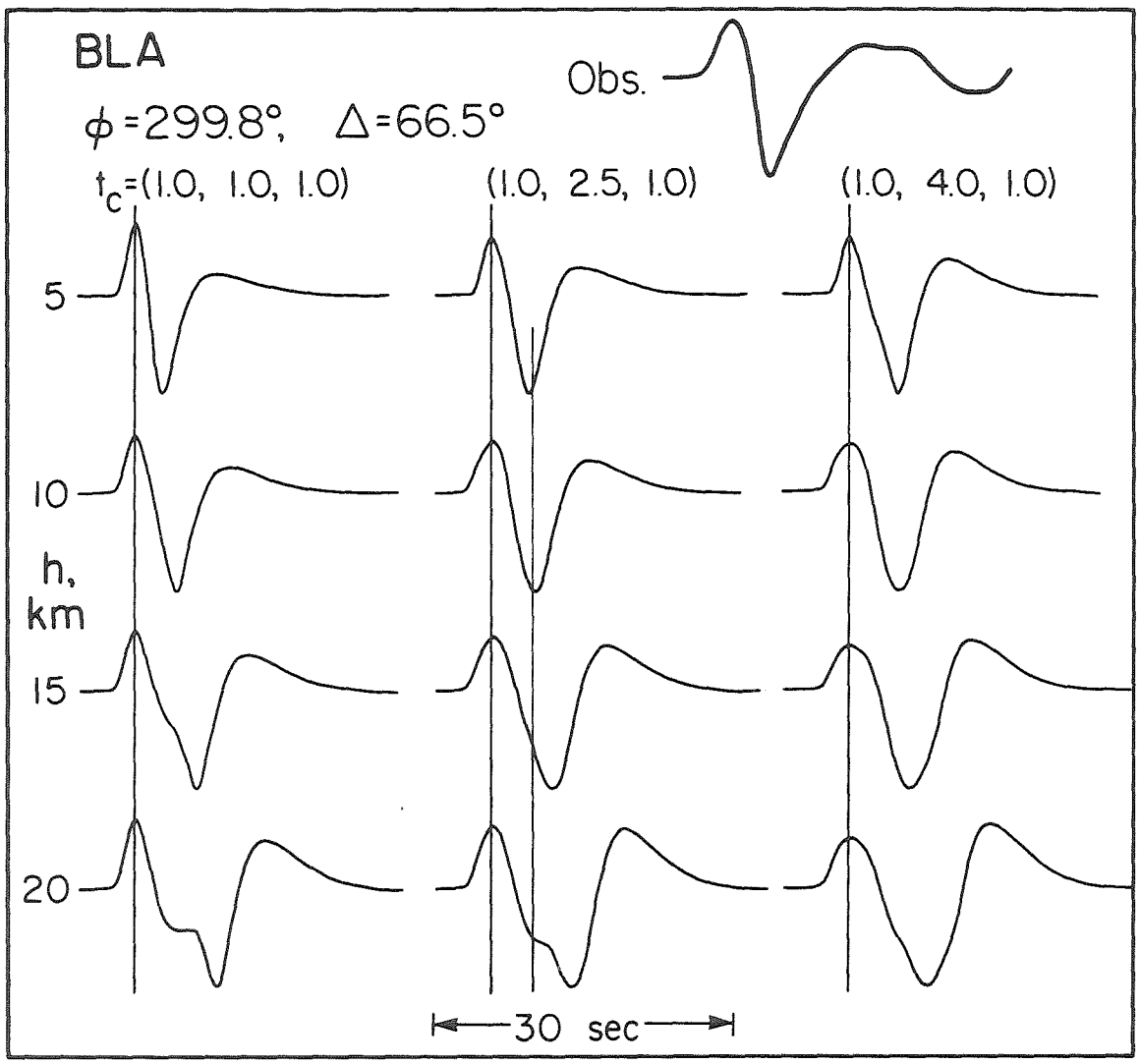

Figure 2-5. Examples of synthetic wave-forms computed for several combinations of source depth (h) and time function (t_c).

correct focal mechanism. This procedure is really an extension of the polarization method except that the whole waveform and not just certain amplitude measurements are used.

Because such factors as source depth and duration, in addition to focal mechanism, influence the waveforms of S, it is necessary to have some estimates of these parameters before S waves can be used to determine the mechanism. Fortunately, the focal mechanism and station distribution for the mainshock allow us to pick stations at which the P wave is not especially sensitive to the orientation of the shallowly dipping (and originally unknown) nodal plane. Examining the focal mechanism on Figure 2-9, we can see that stations such as MSO, BLA, and HKC will always be near the maximum of the P-wave radiation pattern for any possible orientation of the shallowly-dipping plane. By calculating synthetic P waves for various depth and time function combinations (an example is shown in Figure 2-5) we find that the observed records are best fit with a 4.5 sec trapezoidal time function at a source depth of 8 to 10 km.

With the source depth, time function and orientation of one nodal plane known, S waves can be used to determine the position of the second nodal plane in the manner described above. Figure 2-6 shows representative SH and SV waves for various rake angles corresponding to different orientations of the shallowly dipping nodal plane; the steep plane is fixed at strike = 76^{o} and dip = 75^{o}S. The best agreement is for a rake of about 80^{o}, corresponding to plane striking 86^{o} and dipping 15^{o}N.

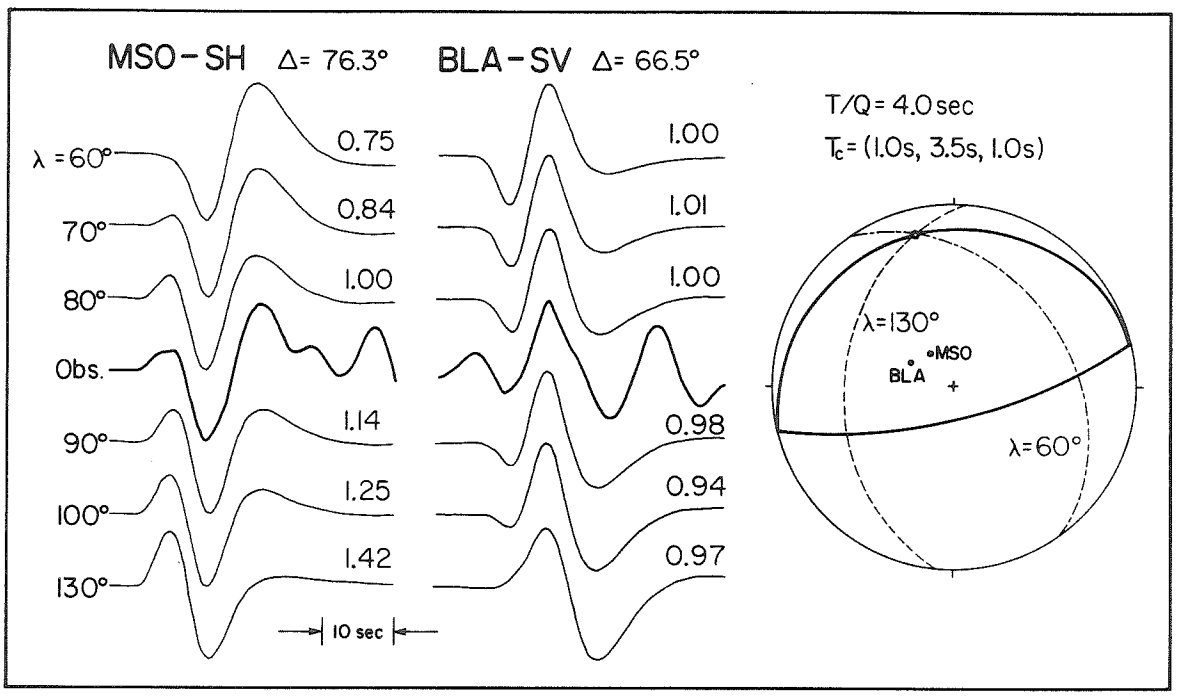

Figure 2-6. Determination of shallowly dipping nodal plane using S-wave data. Note variation of SH-wave synthetics at MSO and SV-wave synthetics at BLA with change in rake angle. Best estimate is that the rake angle lies between 80^{o} and 90^{o}, corresponding to almost pure dip-slip fault motion.

Console (1976) and Ebblin (1976) and Muller (1977) have also published mechanisms for the mainshock. In each mechanism, the position of the steep, southeast dipping plane is in good agreement with the results of this study. Muller used S-wave polarization techniques to determine the orientation of the second plane which he finds dips shallowly to the northwest. In Ebblin's mechanism, the second plane dips shallowly west-northwest, constrained by a single nearby station. In contrast, the results of this paper indicate that the fault plane dips almost due north at a very shallow angle.

After the mechanism and depth of the earthquake have been determined, the next step is to include the effect of crustal structure in the synthetic waveforms. Angenheister et al., (1972) have published a north-south velocity profile for the southern Alps based on nearby refraction lines. Their structure has an upper crustal velocity of 6.0 km/sec extending to about 23 km, interrupted by a low velocity layer from 12 to 20 km. This low-velocity zone, prominent near the Alpine axis, is not well developed in the Friuli region. Below 23 km, the velocity increases to 6.8 km/sec at 30 km, to 7.0 km/sec at 36 km and finally to 8.0 km/sec at about 44 km. A model based on an unreversed refraction profile through the epicentral area has been published by Finetti and Morelli (1972). Their model has an upper crustal velocity of 5.85 km/sec to 12.4 km, below which 6.2 km/sec material extends to 28 km. The lower crust has a velocity of 7.0 km/sec. Mantle velocity of 8.0 km/sec is reached at 45 km. In most important respects, this model is similar to the model of Angenheister et al. (1972). In particular,

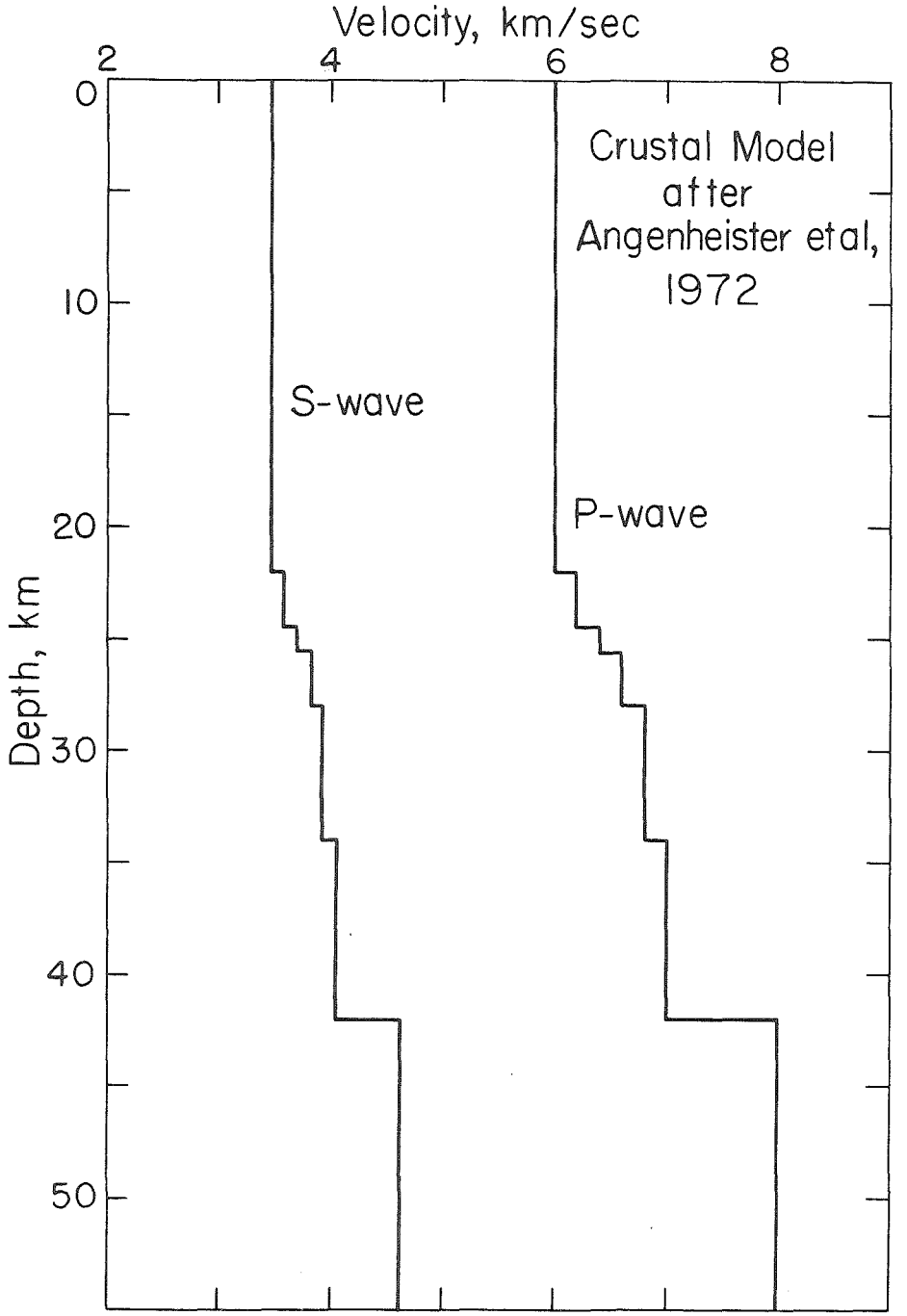

Figure 2-7. Layered crustal structure derived from the profile reported by Angenheister et al. (1972).

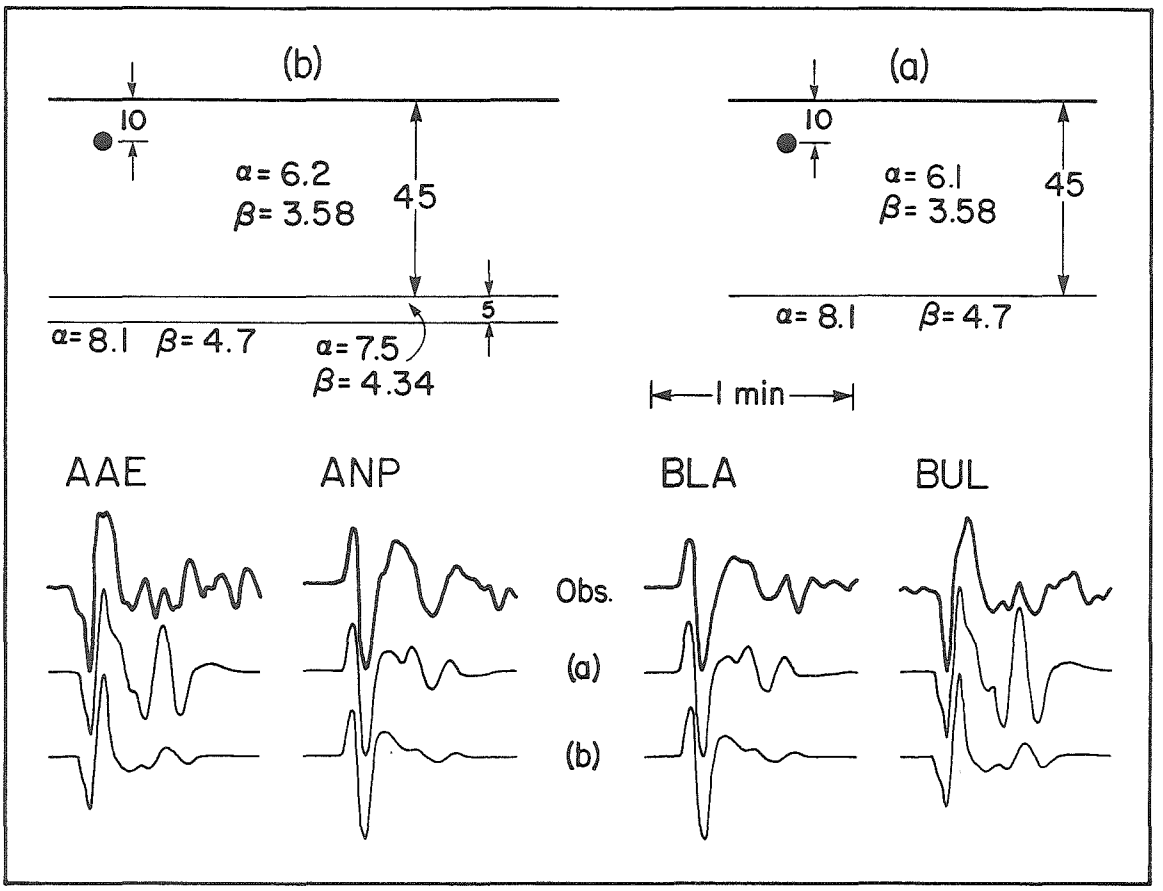

Figure 2-8. Synthetics computed for a layer over halfspace (a) and layer over halfspace with a high velocity layer at base of the crust (b). Note diminution of large reverberation phase between cases (a) and (b). Source is at 10 km depth.

the presence of rather high velocity (7.0 km/sec) material just above the Moho in both models is required to reduce strong phases reflected between the Moho and the free surface which are then radiated to teleseismic distances. These phases arise on synthetic records when there is too large a velocity contrast across the Moho; they are not observed on the real seismograms (Figure 2-8). The Angenheister et al. (1972) model was divided into discrete layers for use in the synthetic seismogram program and the low-velocity zone, which is not very pronounced in the Friuli region, was eliminated. S-wave velocities were calculated from the P-wave velocities by assuming a Poisson's ratio of 0.25. The resulting model is given in Table 2-4 and Figure 2-7.

The matrix method of Haskell (1962) was used to compute the response of the layered crust to an embedded point source. By convolving the crustal response with a Q-operator, far-field source time history and instrument response, realistic synthetic seismograms are created which can be compared directly to the observed records.

Figure 2-9 shows the observed records (heavy lines) and synthetics (light lines) computed for a source at 8 km depth in the Angenheister et al. (1972) structure. The overall agreement between synthetic and observed records is quite good indicating that the basic parameters of the model are reasonable. Rather significant discrepancies occur for stations near nodal lines (AAE, BUL, SHI) and for most stations after the first 15 sec. Nodal stations are especially sensitive to radiation pattern and undoubtedly some of these discrepancies are due to the simple point source model used to compute the synthetics. It is easy to

Table 2-4. Crustal Models

Layer	P-wave Velocity (km/sec)	S-wave Velocity (km/sec)	Density (gm/cm^3)	Thickness (km)	Depth (km)
		Angenheister et al. (1972)			
1	6.0	3.47	2.60	22.0	0.0
2	6.2	3.58	2.66	2.4	22.0
3	6.4	3.70	2.72	1.2	24.4
4	6.6	3.81	2.78	2.4	25.6
5	6.8	3.93	2.84	6.0	28.0
6	7.0	4.05	2.90	8.0	34.0
7	8.0	4.62	3.20	-	42.0
		Halfspace			
1	6.0	3.50	2.78	-	-

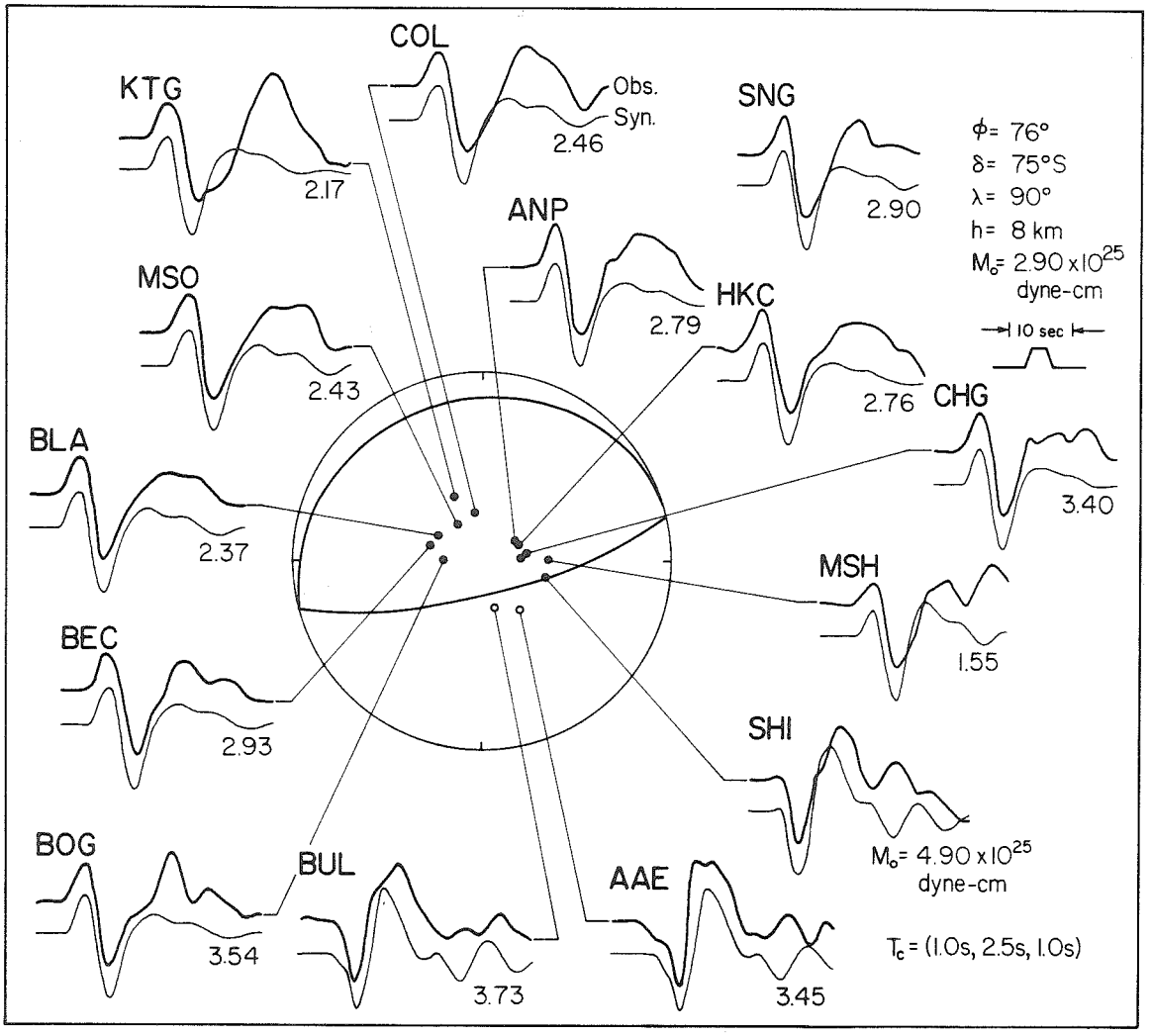

Figure 2-9. Observed P waves (dark line) for mainshock compared to synthetics (light line) computed for a point source at 8 km depth within the structure shown in Figure 2-7. Strike (ϕ), dip (δ), rake (λ), depth (h), average moment (M_o) and time function (t_c) are indicated. Number after each synthetic is the seismic moment at that station.

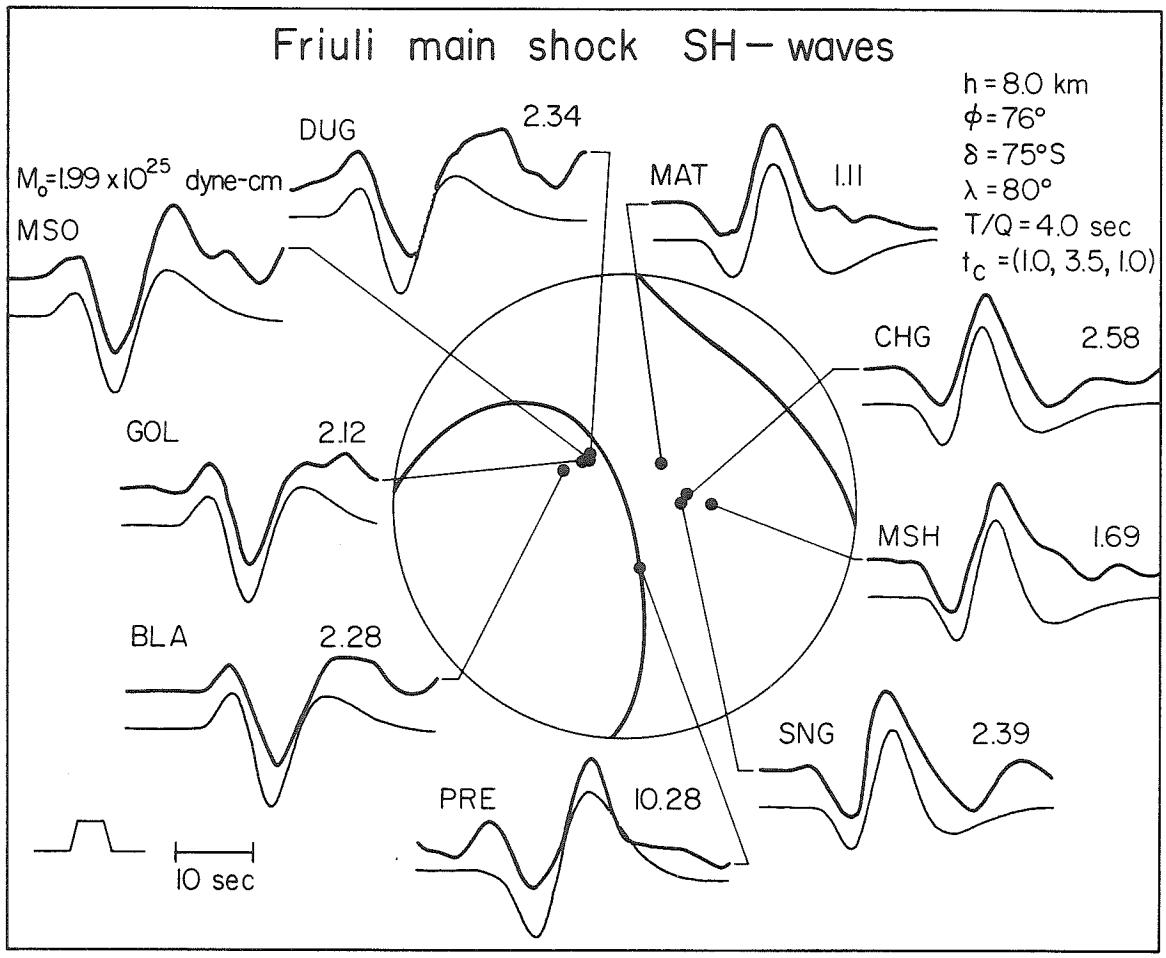

Figure 2-10a. SH waves recorded from the Friuli mainshock compared to synthetics computed for a point source within a halfspace. Note that T/Q_S and t_c are 4.0 sec and 5.5 sec, respectively. Other notation is the same as Figure 2-9.

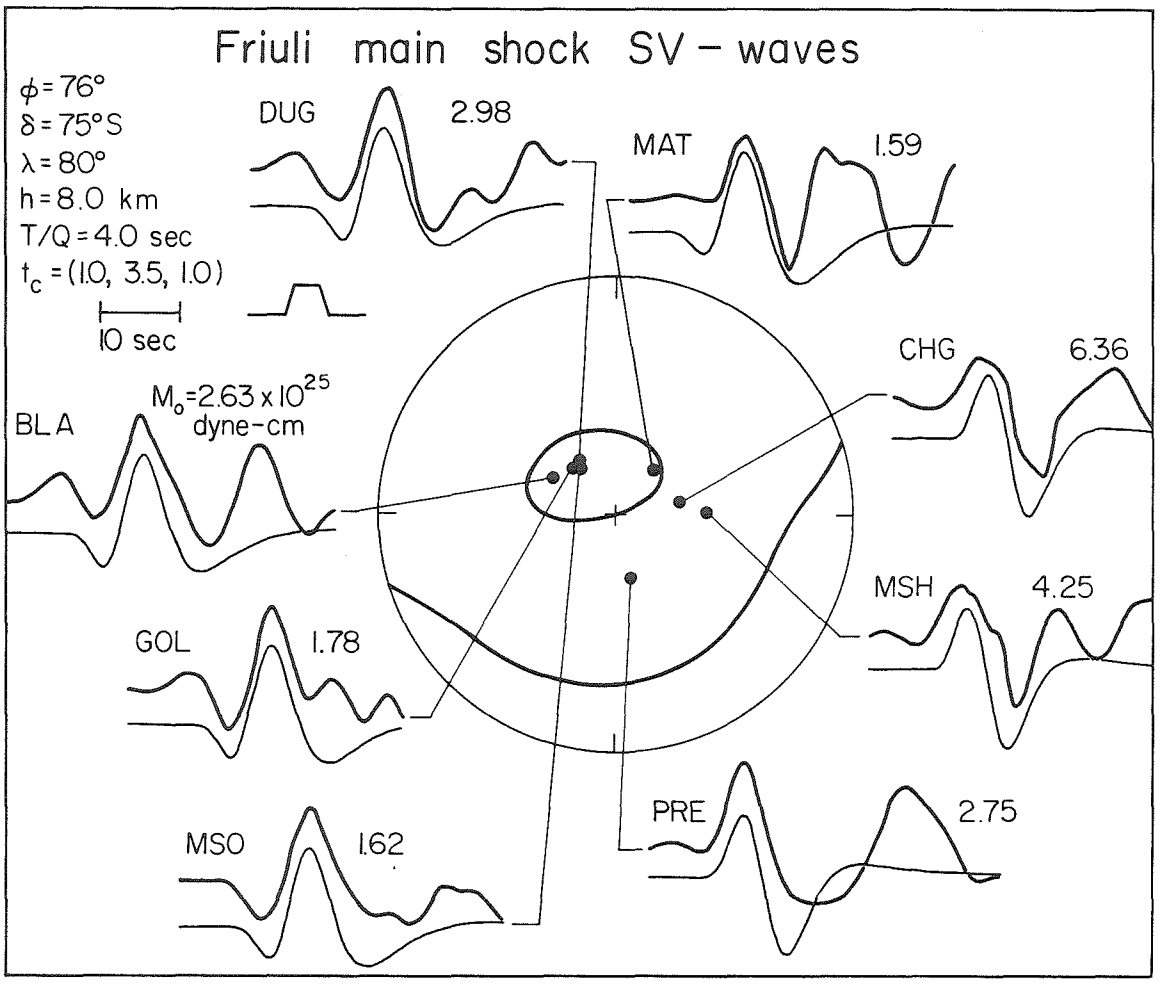

Figure 2-10b. Mainshock SV waves compared to synthetics. See Figures 2-10a and 2-9 for notation.

imagine irregular fault propagation with the fault orientation changing as rupture proceeds. In addition, the real earth is certainly not as simple as the structure used nor have any effects of the crust at the receiving station been taken into account.

S-wave data have already been used to constrain the focal mechanism. Figures 2-10(a, b) show the observed and synthetic SH and SV waves for the mainshock. The synthetics have been computed for the same model used for the P waves except that the length of the time function has been increased to 5.5 sec to better match the observed S-wave duration. The overall fit between observed S waves and synthetic records is good, indicating that the source model is reasonable. With the exception of the SH wave at PRE (Figure 2-10a), which is on a nodal line, the seismic moments calculated from the SH data are somewhat low compared to the P-wave moments. The above calculations were done assuming T/Q = 4.0 sec. Burdick and Mellman (1976) and Burdick (1978) have suggested that T/Q for S waves should be 5.3 sec from their study of the Borrego Mountain, California earthquake. S-wave synthetics for the model with T/Q = 5.3 sec and t_c = 4.5 sec (the P-wave value) are almost indistinguishable from the model presented in Figure 2-10a (T/Q = 4.0 sec, t_c = 5.5 sec), except that the SH moments for the T/Q = 5.3 sec model are in somewhat better agreement with the P-wave moments.

The interpretation of the body wave seismograms of the aftershock of September 15, 1976 (09h 21m) proceeds in the same manner as for the mainshock. Like the mainshock, the orientation of the steeply dipping plane of the aftershock was fixed by P-wave observations while the

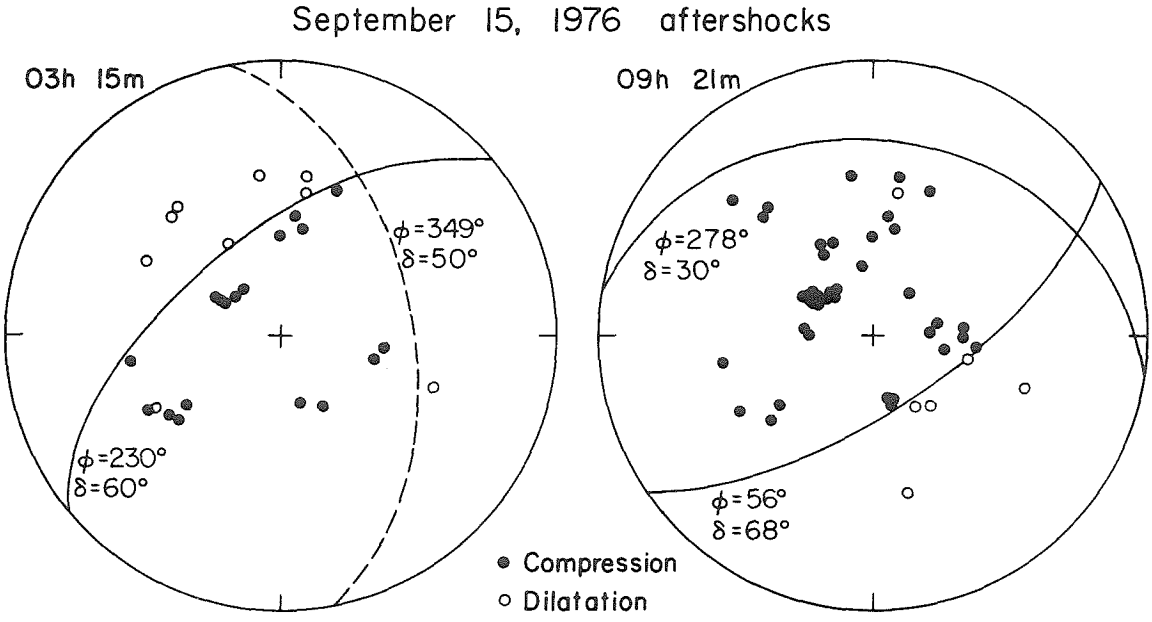

Figure 2-11. P-wave nodal diagram for the September 15, 1976 aftershocks at 03h 15m and 09h 21m. Data was read from WWSSN long-period vertical records along with some auxiliary stations and plotted on the lower half of the focal sphere.

orthogonal plane was determined from S waves. The mechanism is shown in Figure 2-11. The strike and dip of the steep plane are 56° and 67°S, respectively. The shallowly dipping plane shown in Figure 2-11 corresponds to a rake of 70°. Observed and synthetic P and S waves are compared in Figures 2-12 and 2-13. The mechanisms of the mainshock and aftershock are similar, as are the depths, around 8 km. The far-field time function of the aftershock has a duration of 3 to 3.5 sec whereas the mainshock is about 4.5 sec in duration. The aftershock P-wave moment is 1.0×10^{25} dyne-cm compared to 2.9×10^{25} dyne-cm for the mainshock.

The regional tectonics, in particular the mapped east-west striking thrust faults (Figure 2-1), suggest that for both the mainshock and aftershock the shallow, northward dipping nodal plane is the fault plane. In the case of the mainshock, the roughly elliptically shaped aftershock distribution (Figure 2-2) also suggests that the shallowly dipping nodal plane is the fault plane (Cagnetti and Console, 1977). In this case, the fault motion is nearly pure dip-slip with the northern block (Alps) overthrusting the sedimentary basin. The shallowly dipping plane of the 09h 21m aftershock mechanism is similar in orientation to that of the mainshock, although the slip vector is more oblique.

A focal mechanism has also been prepared for the large aftershock which occurred at 03h 15m on September 15 (Figure 2-11). Because the P waves are small to begin with and because they are somewhat obscured by noise from a previous event, good first motion readings are rare. Nevertheless, it is clear that the mechanism of this earthquake is

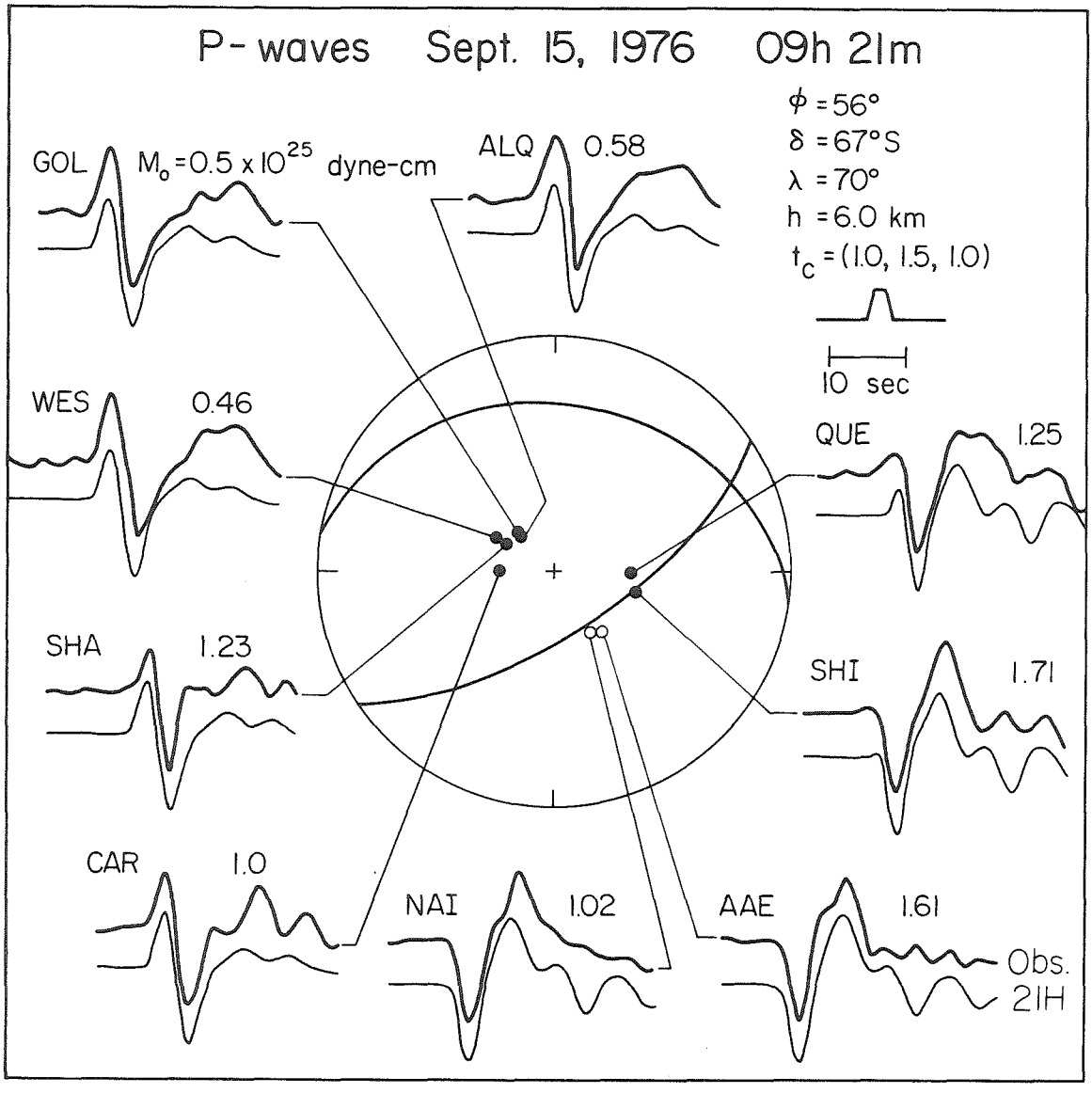

Figure 2-12. Observed and synthetic P waves for the aftershock of 09h 21m, September 15, 1976. Synthetics are computed for a point source at 6 km depth in the Angenheister et al. (1972) structure (Table 2-4). Other notation is the same as Figure 2-9.

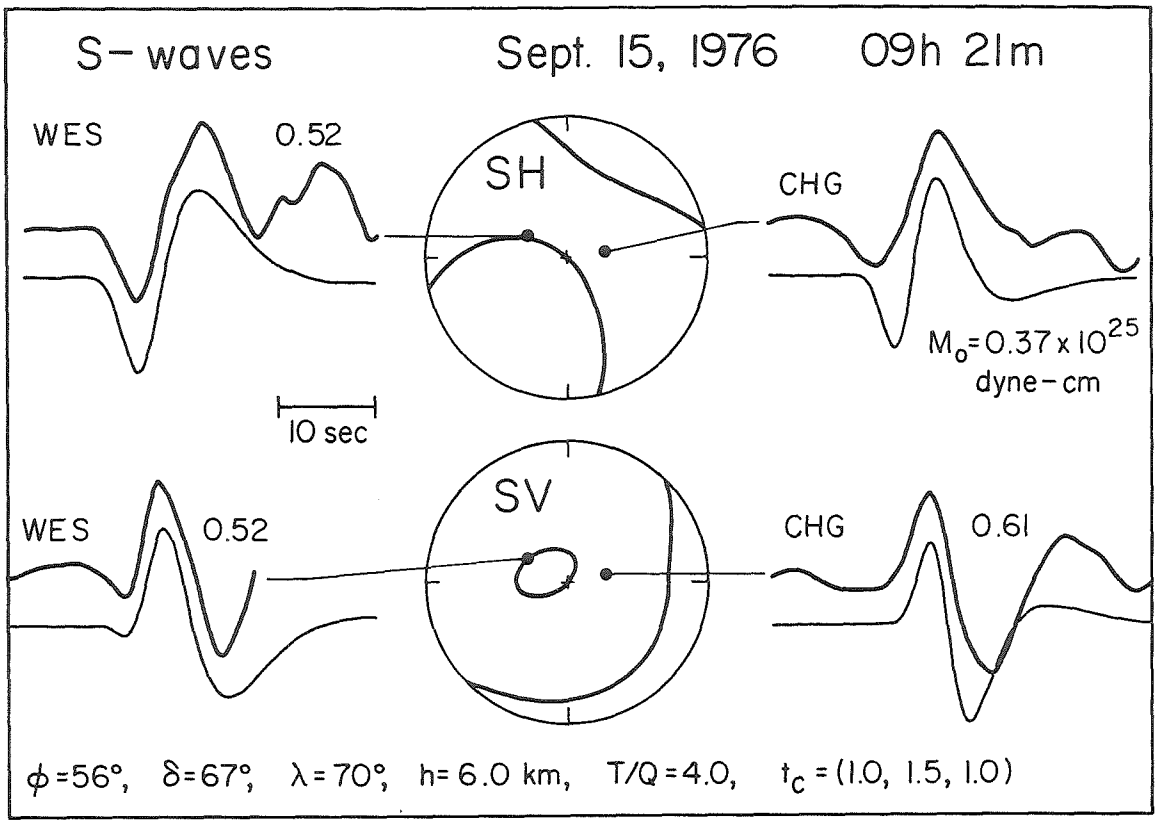

Figure 2-13. S waves for the aftershock of 09h 21m showing observed and synthetic records and SH and SV radiation patterns.

somewhat different than the mechanisms obtained for the mainshock and 09h 21m aftershock. Certain stations are clearly reversed. An important observation was made by Ritsema (1976) on the long-period, vertical seismographs at de Bilt, The Netherlands. He observed a clear change in polarity between the mainshock and 09h 21m aftershock on one hand and the 03h 15m shock on the other. The mechanism of the 03h 15m aftershock appears to represent predominantly dip-slip fault motion, but with a considerable strike-slip component. In contrast to the other aftershock, which has the nodal planes that strike nearly east-west, the focal planes of this aftershock strike north and northeast. There are no major northeast-southwest striking structures in the area, although Martinis (1975, his Figure 13) does indicate several minor north-south trending lineations.

The mechanisms determined in this paper are somewhat different from mechanisms published for earlier earthquakes in the Friuli region. McKenzie (1972) suggests that the event of October 18, 1936 had a normal faulting mechanism, although Ahorner et al. (1972) present a strike-slip mechanism for this earthquake. Mayer-Rosa et al. (1976) studied the mechanism for the event of March 24, 1975 (m_b = 4.2, U.S.G.S.). Because it was quite small, there is considerable ambiguity in the solution. The event is either strike-slip or, as Mayer-Rosa et al. prefer, thrust on an almost east-west striking fault plane.

Finite Fault

Up to this point, the body wave records have been interpreted using

synthetic seismograms computed for a point source in a layered halfspace. Two assumptions are made in computing point source synthetics. The first is that the same time function is used for each ray (e.g., P, pP, sP, etc.) and the second is that the same time function is used for all azimuths and take-off angles. For an arbitrarily oriented, propagating shear fault, these assumptions are invalid. In the first place, P and S rays each require a different time function and secondly, the time function observed at any point is dependent on the angle between the direction of rupture propagation and the take-off angle (Savage, 1966).

It is the purpose of this section to investigate the nature of rupture propagation during the Friuli mainshock using the formulation of Heaton (1978) which allows arbitrarily complex faulting histories. In the present discussion, we will try to place constraints on the fault area and mode of rupture propagation, either unilateral or bilateral. To simplify the problem, it is assumed that the shallowly dipping nodal plane of Figure 2-4 is the fault plane, that the dislocation is uniform over the entire fault surface and that the rupture velocity is 3.0 km/sec. Furthermore, the shape of the fault plane is a square and the dislocation rise time is 1 sec. The six cases investigated are shown in Figure 2-14; the heavy broken line is the approximate limit of aftershock concentration from Figure 2-2, and the stars represent the epicenters as determined by various agencies (refer to Figure 2-3). In the upper part of Figure 2-14, the square fault planes are centered on the epicenter determined by Rome which is near the middle of the

Figure 2-14. Fault models used for the finite fault calculations. Six cases are shown corresponding to square faults of length 8, 16 and 24 km. In the upper part of the figure, the theoretical fault planes are centered on the hypocenter determined by Rome which lies near the center of the aftershock distribution. The lower part shows the same fault planes, now aligned so that the upper right corner (northeast) is near the NEIS and ISC epicenters. Dashed line indicating the limits of the aftershock concentration gives a sense of scale.

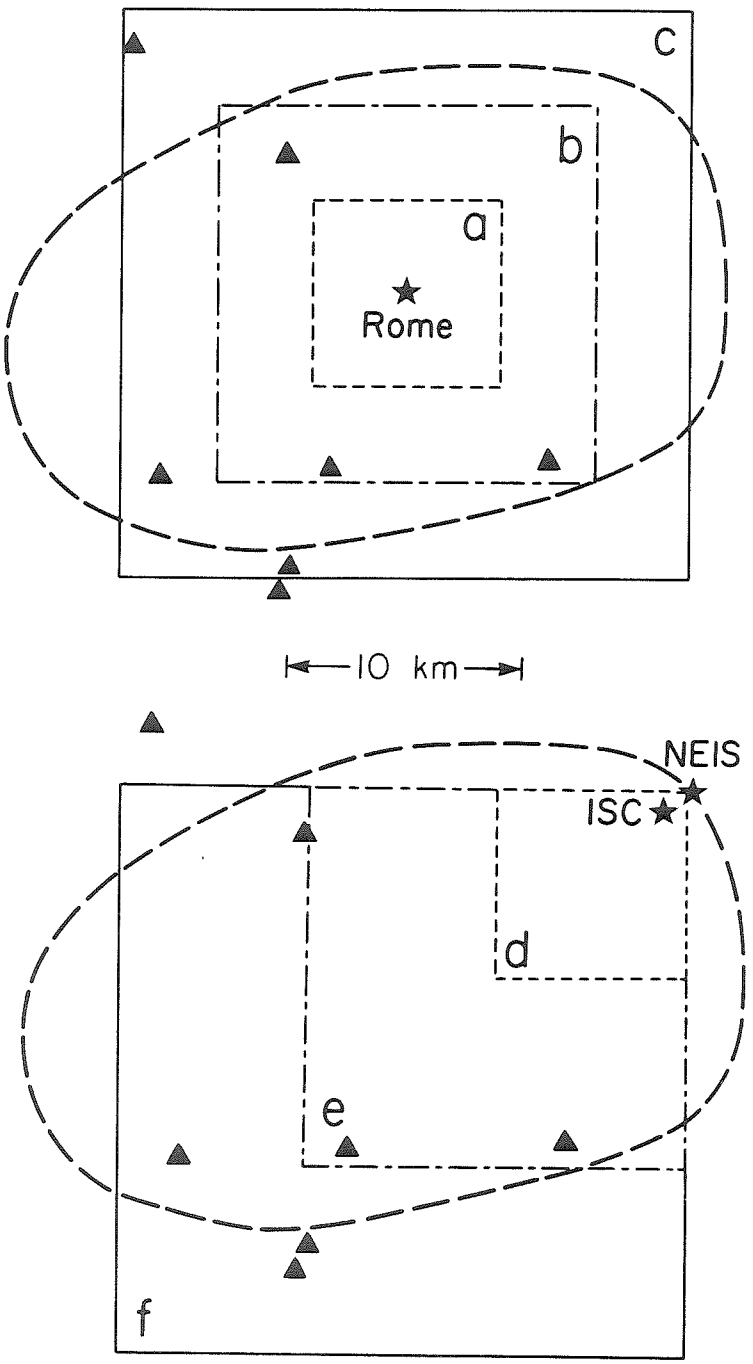
c
b
a
Rome
10 km
NEIS
ISC
d
e
f

aftershock distribution. Three cases, fault lengths of 8, 16 and 24 km, are computed. The superposition of the theoretical fault planes on the aftershock distribution is rather arbitrary, but it does give a sense of scale. The lower part of Figure 2-14 shows three cases in which the fault originates at one corner of the fault plane and propagates unilaterally updip and towards the west. The NEIS and ISC epicenters are near the northeast (down-dip) corner of the aftershock distribution.

Synthetics for the six cases are shown in Figures 2-15 and 2-16. The model which best fits the P waves seems to be case c. The observed data do not change very much with azimuth and, as expected, the symmetrically expanding cases (a, b, c) reproduce this effect quite well. In contrast, the unilateral faults, especially case f, exhibit strong azimuthal variation. Unilateral propagation cannot be ruled out, however. For instance, case e fits the P-wave data almost as well as case c. What can be said, instead, is that there cannot be a strong propagation effect. Nor can the fault plane be substantially smaller than the aftershock area. Cases a and d give rise to synthetic seismograms which are much too narrow in duration compared to the observed data. From these results, the probable fault length is 16 to 24 km, but whether faulting initiated at the center or edge of the zone cannot be determined.

Additional constraint on the rupture mechanism is provided by SH waves (Figure 2-16). Again, case f with strong azimuthal variation is ruled out by the data as are the cases with small fault planes (cases a, d). It must be kept in mind that the uncertainty in the value of

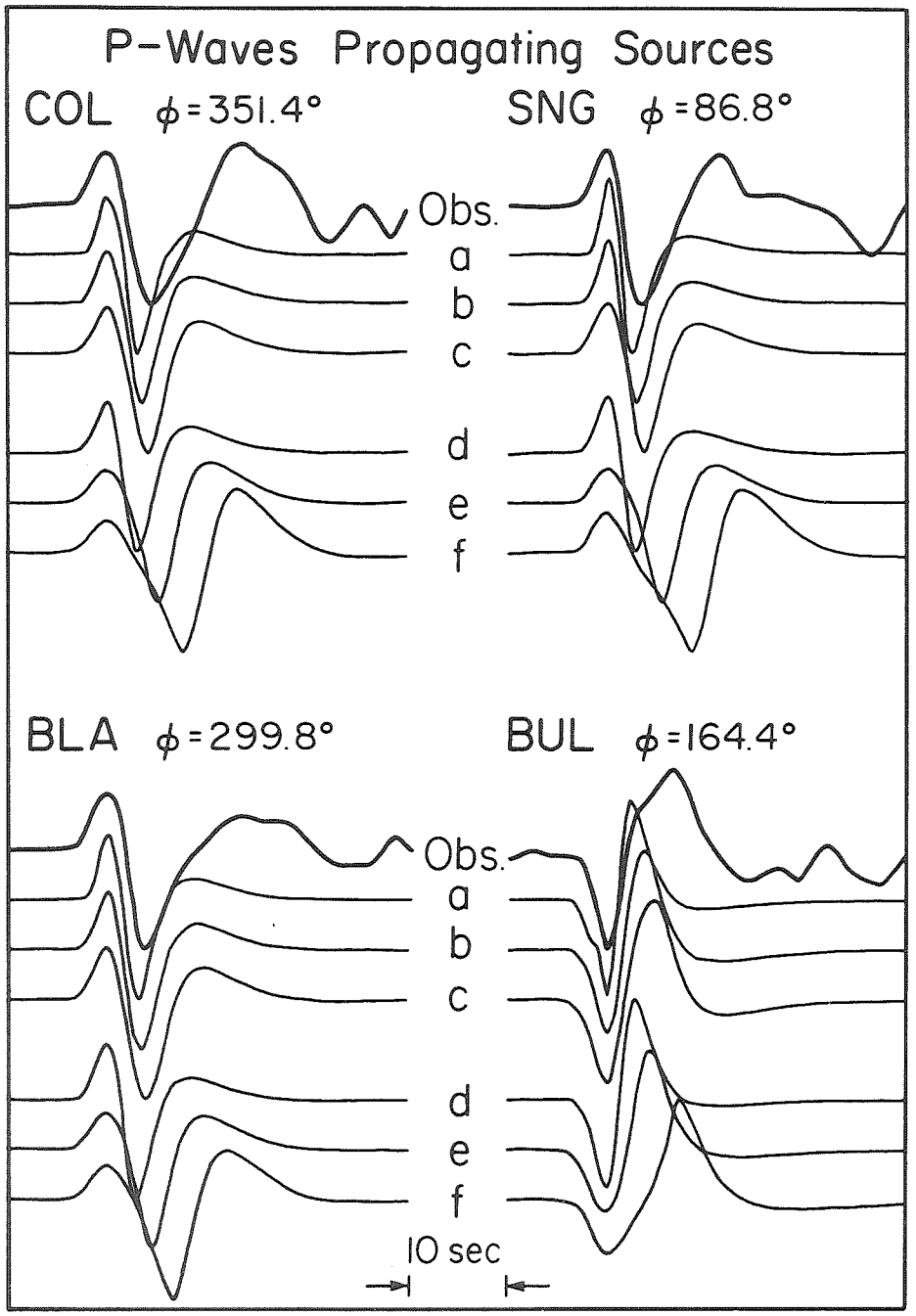

Figure 2-15. Observed P waves for four stations compared to synthetics computed for finite fault models (a) through (f).

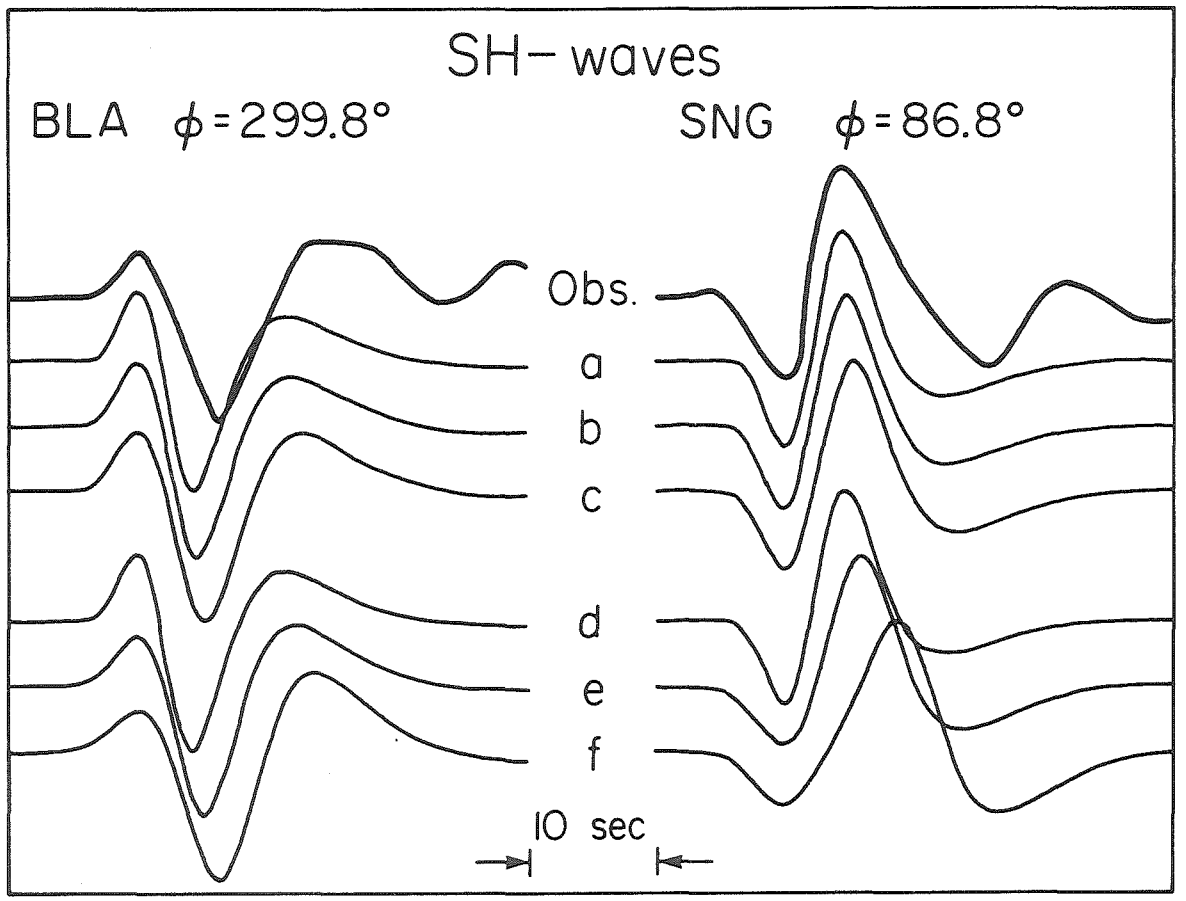

Figure 2-16. Observed SH waves compared to synthetics computed for the finite fault models.

attenuation for S waves can have considerable effect on pulse width and hence the estimate of fault size.

Rayleigh Wave Data

An independent estimate of the focal mechanism and seismic moment is provided by surface waves. In this study, the observed values of spectral density of 100 sec Rayleigh waves are compared to theoretical values calculated using the tables published by Ben-Menahem et al. (1970). The observed data were prepared by first digitizing the seismograms in a group velocity window between 4.0 and 3.5 km/sec, then detrending and interpolating to a uniform time interval. The spectral density was obtained by a fast Fourier transform program. The spectrum was corrected for instrument response according to the formulation of Hagiwara (1958) and normalized to a propagation distance of 90^{o} using the equation:

$$[\sin(\Delta/a)/\sin(\Delta_o/a)]^{1/2} \exp\{\gamma(\Delta/\Delta_o)\}$$

where Δ = epicentral distance

Δ_o = normalized distance ($= 90^{o}$)

a = Earth radius

γ = attenuation coefficient

The attenuation coefficients determined by Ben-Menahem et al. (1970) are used.

In Figure 2-17, the observed values of spectral density for 100 sec Rayleigh waves are compared to the theoretical radiation pattern computed for the source model found using body waves (strike = 76^{o}, dip

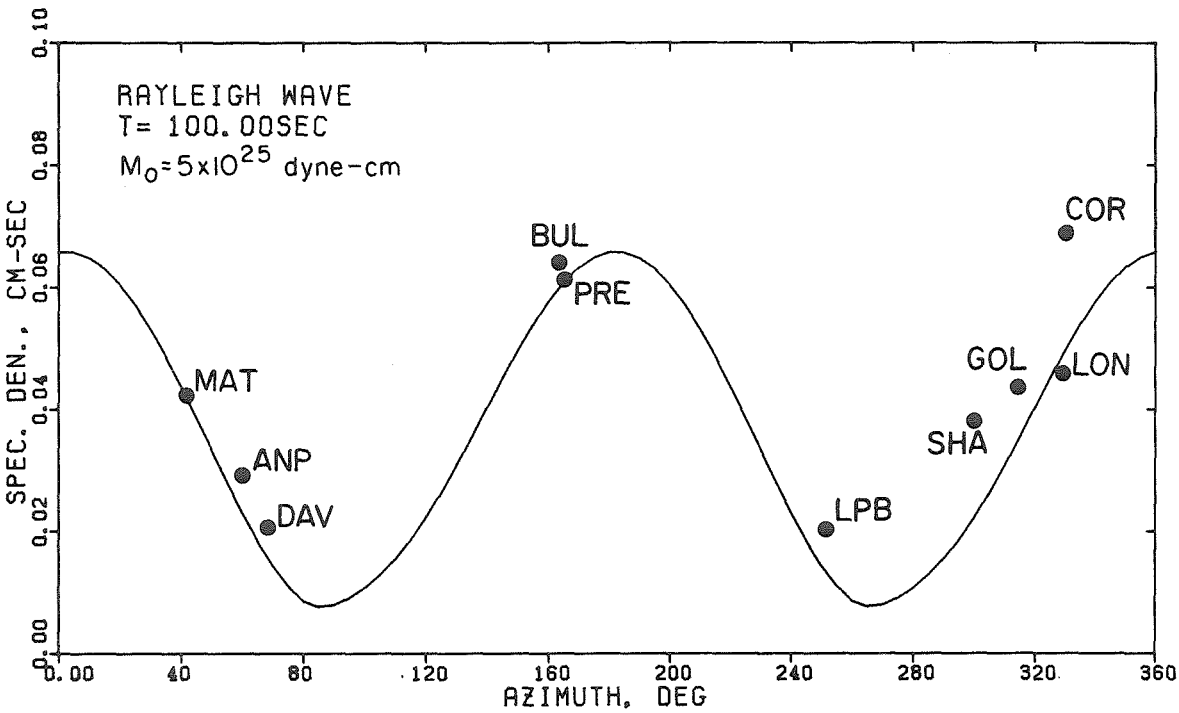

Figure 2-17. Observed spectral density of 100 sec Rayleigh waves radiated by the mainshock compared to the theoretical pattern for the focal mechanism shown in Figure 2-4. Seismic moment is found to be 5 x 10^{25} dyne-cm.

= 75°S, rake = 80°, depth = 10 km). The good agreement between the observed data and theoretical calculations indicate that the overall deformation recorded by 100 sec surface waves is the same as that recorded by ~15 sec body waves. However, the seismic moment determined from 100 sec surface waves is 5 x 10^{25} dyne-cm, somewhat higher than the value of 2.9 x 10^{25} dyne-cm found for body waves.

Chapter Three

Broad-Band Time Domain Modeling of Earthquakes from Friuli, Italy

Introduction

Recent years have witnessed considerable advances in understanding earthquake source processes by detailed investigation of body waves. Most studies done to date have concentrated on P and S waves recorded by WWSSN long-period seismographs. A partial list of contributors includes Burdick and Mellman (1976), Ebel et al., (1978), Langston and Butler (1976), Langston (1976b, 1978), and Wyss and Hanks (1972).

Less attention has been paid to teleseismic short-period records. This is due, no doubt, to the rather complex appearance of these seismograms resulting from the sensitivity of short-period waves to the vagaries of the seismic source and propagation medium. Burdick and Mellman (1976) used a long-period-short-period deconvolution technique to obtain a more detailed time function for the Borrego Mountain, California earthquake. Somerville et al. (1976) used the Savage (1966) source model and an inversion scheme to obtain fault parameters for two short duration earthquakes. Langston (1976b) found that crustal effects were important in time domain modeling of the short-period records of the Koyna, India earthquake. Langston (1978) used short-period observations to fix the hypocentral depth and infer a small amount of down-dip rupture propagation during the 1971 San Fernando earthquake.

Ebel (1980) argued for localized high stress drop in the Borrego Mountain earthquake. Hartzell (1980) modeled the long-period and short-period body waves from the 1976 Gazli, U.S.S.R. earthquake, finding evidence for upward rupture propagation initiated by massive, localized faulting at the hypocenter. Simultaneous modeling of short- and long-period records led Bache et al. (1980) to a similar conclusion regarding the 1975 Pocatello Valley, Idaho earthquake. Wyss and Hanks (1972) employed short-period observations to extend their source spectra measurements.

In the previous chapter, source models for the mainshock and 09h 21m aftershock were developed based on long-period body and surface wave data. Focal mechanisms show that these earthquakes represent shallow angle thrusting of the Alps over the Friuli Plain (Figures 2-4 and 2-11). Source depth, seismic moment and time function duration are found to be 8 km, 2.9×10^{25} dyne-cm and 4.5 sec for the mainshock; and 6 km, 1.0×10^{25} dyne-cm and 3.5 sec for the aftershock. The fault area which radiated the long-period body waves is estimated by comparing the observed records to synthetics computed for finite fault models and is found to be 400 km^2 and 100 km^2 for the mainshock and aftershock respectively. Surface wave observations at 100 sec period confirm the long-period body wave focal mechanism and seismic moment for the mainshock. In this chapter, short-period seismograms are modeled in the time domain to obtain a more detailed estimate of the source time function. The short-period models are then tested against the long-period observations to obtain a picture of the source in the period

range 1 to 100 seconds.

Modeling Short-Period Records

Modeling the short-period P-wave seismograms of the three Friuli earthquakes proceeded in two distinct phases. The initial part of the work involved a lengthy attempt to model the records by trial and error. Reasonable models were obtained for each earthquake and were used as starting models for a waveform inversion routine (Mellman, 1978). The primary advantage of the inversion program is that it is a fast, unbiased method of assessing the agreement between observed and synthetic records for a portion of the model space around the starting model. The program attempts to find a path through the model space along which the discrepancies between observed and synthetic records decrease. The inversion procedure was stopped when there was little or no further improvement in the cross-correlation, N_i, of the synthetic and observed seismograms (Burdick and Mellman, 1976). Overall goodness-of-fit for each model was computed using the formula

$$\sum_i \{(1-N_i)/w_i\}$$

where w_i (≥ 1) is the weight of each station with w_i = 1.0 implying full weight. Best-fitting models are those with the lowest overall goodness-of-fit whereas the best stations have the highest correlation coefficients. These quantities are given in Table 3-4 for the starting and final models for the September 15 aftershocks. The stations used in

the inversion runs are marked by asterisks after the station abbreviation in Figures 3-2, 3-6 and 3-8. There is no guarantee of uniqueness in this procedure, but the source models thus obtained are reasonable in all cases.

All the inversion runs were made using three rays (P, pP, sP) in a half-space, while the synthetics presented below (Figures 3-2, 3-3, 3-5, 3-7, 3-8) were computed with the Angenheister et al. (1972) crustal model (Table 2-4). The calculations were done using the same source time function for each ray, irrespective of wave type or take-off angle. The source models derived from inverting short-period data were tested against long-period seismograms with varying success as will be shown below.

09h 21m Aftershock

The earthquake of September 15, 1976 at 09h 21m will be discussed first because the interpretation of its source properties is the most straightforward. The long-period records for this earthquake were studied in Chapter Two where the thrust mechanism shown in Figures 2-2 and 2-11 was obtained. Geological considerations suggest that the northward dipping plane is the fault plane, indicating southward thrusting of the Alps over the Friuli plain. Focal depth, time function duration and seismic moment were found to be 6 km, 3.5 sec and 1.04×10^{25} dyne-cm respectively (Table 3-1).

In the trial and error stage of modeling the short-period records, considerable attention was paid to three stations in the western United

Table 3-1. 09h 21m Source Models

	Chapter Two	Starting Model SP35		Final Model SP53	
		1st	2nd	1st	2nd
Strike (deg)	56	56	56	56	56
Dip (deg)	67	67	67	67	67
Rake (deg)	70	70	70	70	70
Depth (km)	6.0	6.75	6.75	7.5	5.9
M_o (10^{25} dyne-cm)	1.04	0.17	0.68	0.18	0.59
Time Lag (sec)	0.0	0.0	1.5	0.0	1.3
Rise (sec)	1.0	0.5	0.5	0.72	1.15
Top (sec)	1.5	1.0	1.0	0.82	0.0
Fall (sec)	1.0	1.0	1.0	0.10	1.15

States: GOL, ALQ, and DUG. Examining the observed seismograms in the upper left corner of Figure 3-2, note that the overall waveforms at these stations are quite similar. This suggests that the records are dominated by source properties and crustal structure in the focal region and that receiver crustal structure has only a minor role in shaping the waveforms.

From early modeling efforts, it soon became apparent that the long-period source model of Chapter Two would not fit the short-period seismograms and that two sources, a small event followed by a larger one, were necessary to fit the western U.S. records. After numerous attempts, a model called SP35 (Table 3-1) was found which did reasonably well in predicting the seismograms at GOL, ALQ and DUG, but not so well for other stations (AAE and GOL are shown in Figure 3-1). Next, SP35 was used as a starting model for the inversion program. A number of runs were made, each inverting for different combinations of the parameters listed in Table 3-1. Model SP53 was adopted as the final model, when, after 18 iterations, the inversion program could not make any further improvement to the fit. As can be seen in Table 3-1, the major differences between SP35 and SP53 are in the depths and time functions of the two sources. There seems to be no azimuthal variation in the relative timing of the sources, suggesting that both are very close together on the fault plane. Results of several inversion runs indicate that the mechanisms of both events are similar. Note the considerable improvement in the fit to station AAE (Figure 3-1).

A comparision of SP53 computed for the half-space and Angenheister

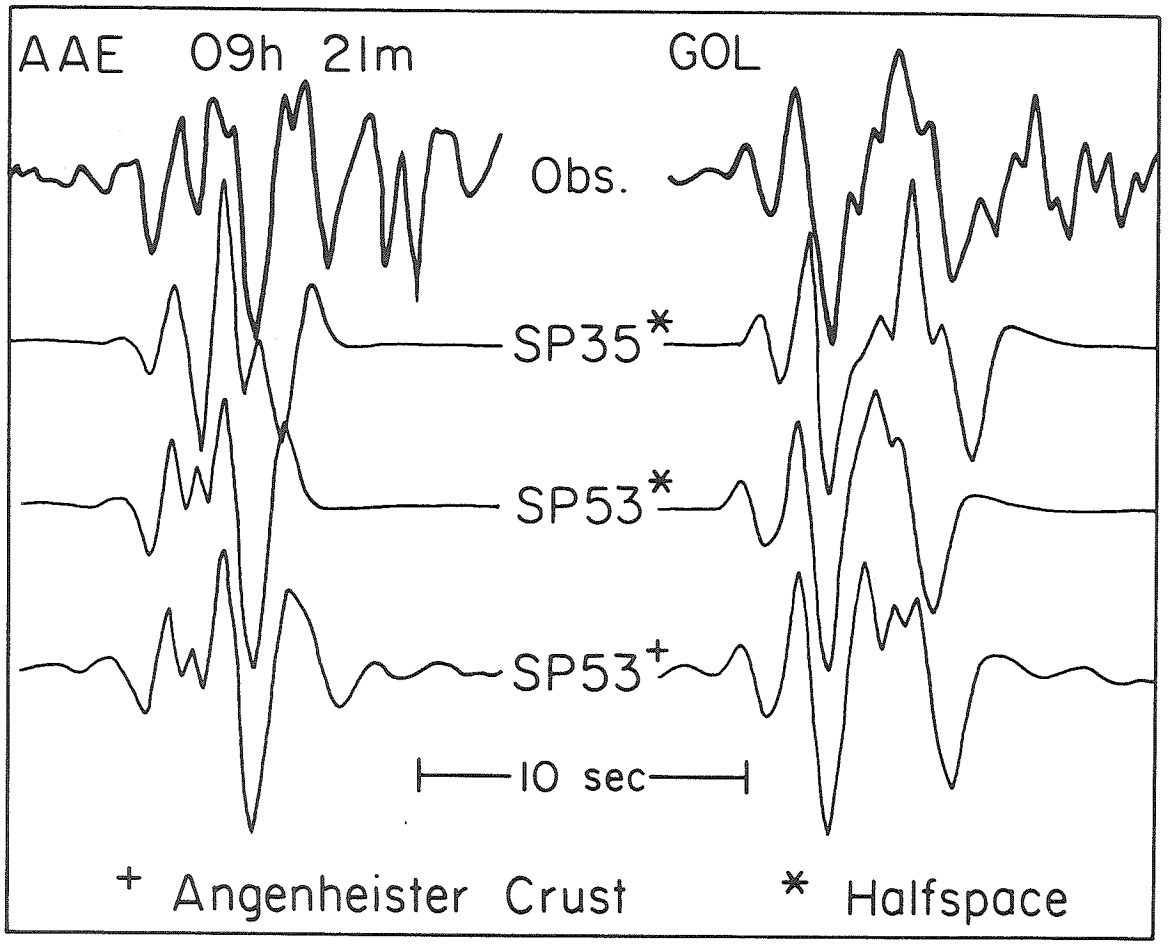

Figure 3-1. Comparison of observed short-period seismograms (heavy line) of the 09h 21m aftershock recorded at AAE and GOL to synthetics (light line) computed for models SP35 (half-space) and SP53 (half-space and Angenheister crustal model).

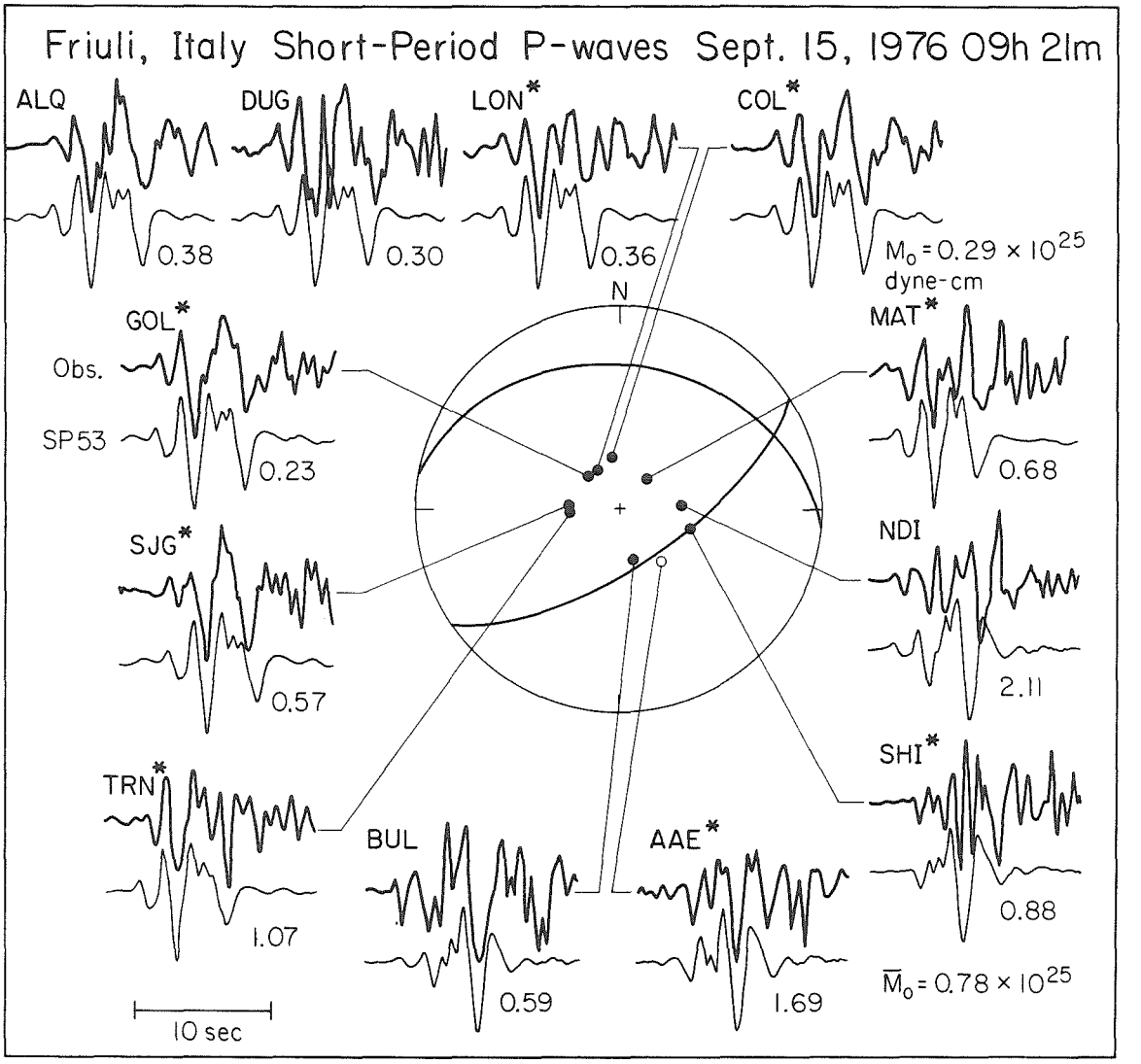

Figure 3-2. Observed short-period seismograms (heavy line) of the 09h 21m aftershock compared to synthetics (light line) computed for model SP53 (Table 3-1) in the Angenheister crustal model (Table 2-4). Numbers below each synthetic are the seismic moments; the average seismic moment (M_o) is 0.78×10^{25} dyne-cm. Asterisks after station abbreviations indicate stations used in the inversion program.

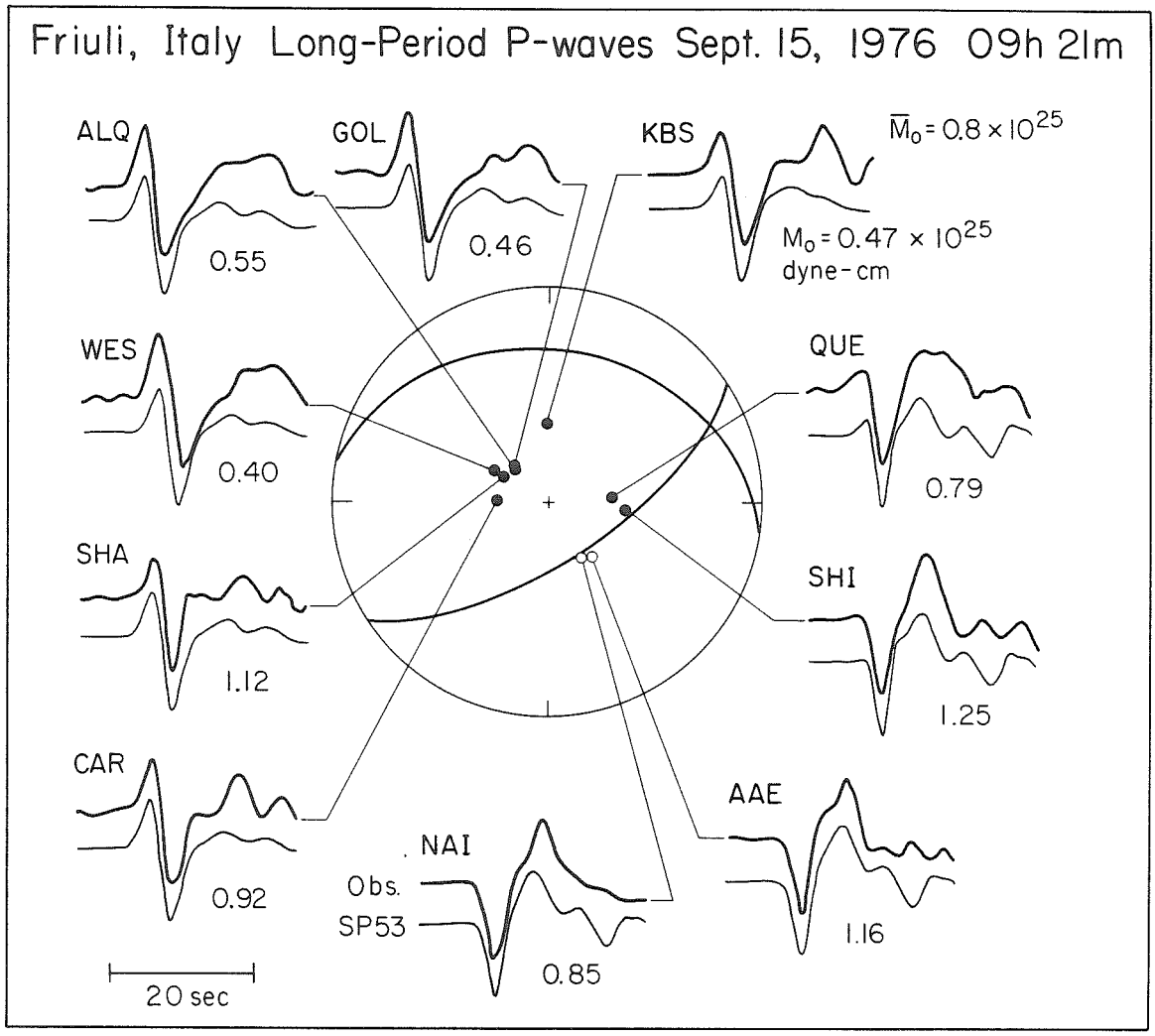

Figure 3-3. Observed long-period seismograms (heavy line) of the 09h 21m aftershock compared to synthetics (light line) computed for model SP53 (Table 3-1) in the Angenheister crustal model (Table 2-4). Numbers below each synthetic are the seismic moment; the average moment is 0.8×10^{25} dyne-cm.

crust (Table 2-4) is shown in Figure 3-1. There is little difference in the first four to five seconds of record, but the crust does noticeably affect the latter portion. Overall, the Angenheister crustal model improves the fit between observed and synthetic seismograms compared to the half-space case. At most stations, the agreement between observed records and synthetics is quite good (Figure 3-2). Using SP53 to compute long period seismograms also yields good agreement with the observed data (Figure 3-3). Even such elusive features as the shoulder on the upswing at stations AAE, NAI, and SHI are reproduced in the long-period synthetics. The overall seismic moment derived from the short-period P-waves is 0.78×10^{25} dyne-cm, in excellent agreement with the value of 0.8×10^{25} dyne-cm obtained from long-period body waves. The attenuation operator was computed using $T/Q = 1.0$ sec for both long- and short-period synthetics.

It is of interest to compare the model derived from short-period data, SP53, to the model derived solely from long-period observations in Chapter Two. Both models produce long-period synthetic seismograms which are very similar, yet SP53 is the more adequate model in that it also correctly predicts the short-period records. The source depths and focal mechanisms for both models are similar; it is the far-field source time functions which differ. The total duration of both time functions, the parameter which controls the long-period waveforms, is also the same (3.5 sec) but the rather complicated structure of the SP53 time function is necessary to explain the short-period records. Note that the seismic moment of SP53 (0.8×10^{25} dyne-cm) is in reasonable

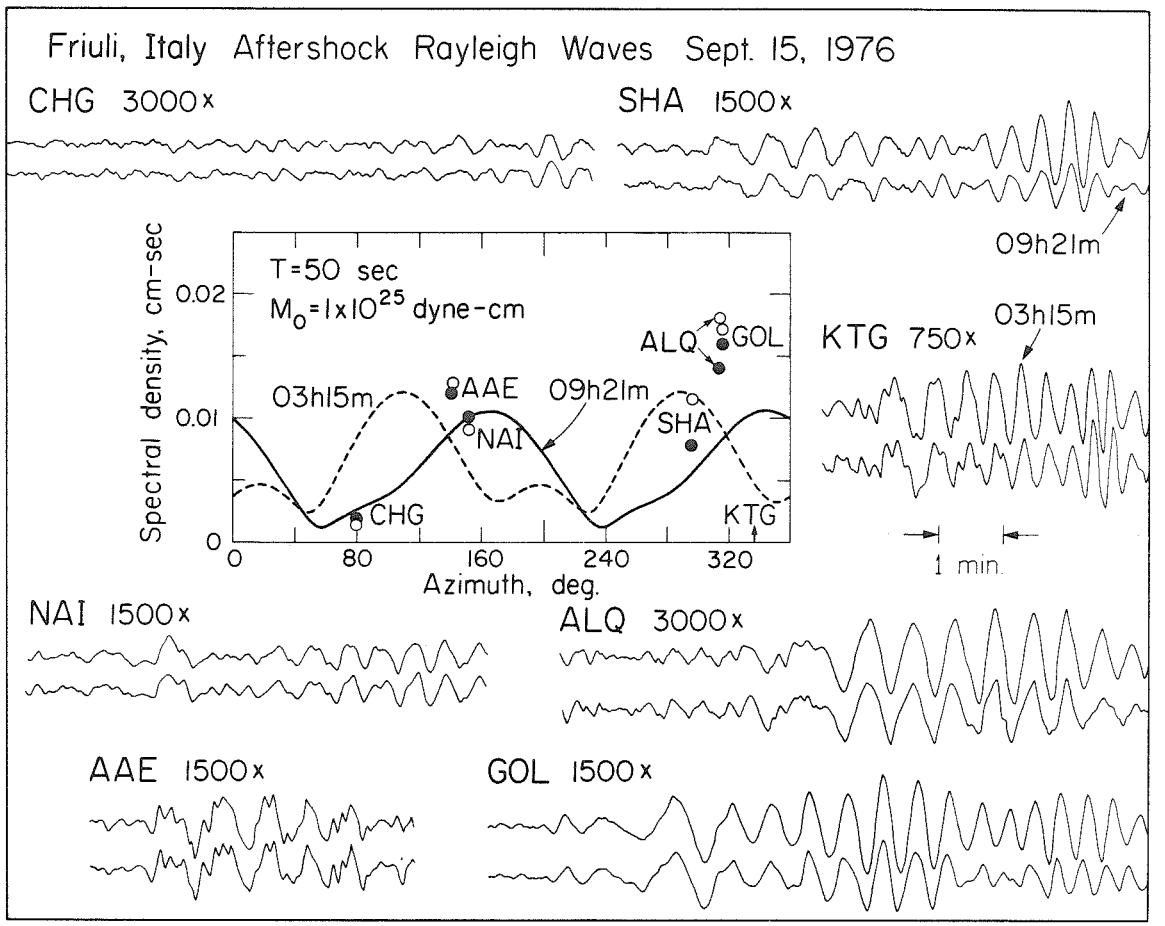

Figure 3-4. Rayleigh wave observations of the 03h 15m aftershock (upper trace for each station) and the 09h 21m shock (lower trace) are compared for a number of WWSSN stations. Numbers after station abbreviation indicate long-period instrument magnification. Inset shows the observed spectral density (points) versus theoretical calculations (lines). Filled points and solid lines are for the earthquake of 09h 21m, open circles and broken lines are for the 03h 15m shock. Data are equalized to 90 degrees and theoretical calculations made assuming a moment of 1 x 10^{25} dyne-cm.

agreement with the value obtained in the previous chapter (1×10^{25} dyne-cm).

An estimate of the moment for the 09h 21m earthquake was also made from the spectral density of 50 sec Rayleigh waves equalized to a distance of 90^{o}. The filled circles of Figure 3-4 show the observed spectral density at 50 sec for the records shown. The solid line is the theoretical radiation pattern computed from the tables of Ben Menahem et al. (1970) for a source at 10 km depth in their continental structure and having the mechanism shown in Figure 2-11. The moment inferred from these calculations is $1\text{-}1.5 \times 10^{25}$ dyne-cm, in reasonable agreement with the estimates made from body waves. These results show that the source spectrum is nearly flat in the period range 0.5 sec to 50 sec.

03h 15m Aftershock

We now turn to a discussion of the aftershock at 03h 15m on September 15. The focal mechanism (Figure 2-11) is quite different from those of the mainshock and 09h 21m aftershock. The nodal lines strike north and northeast instead of east-west as for the other events and the mechanism exhibits much more strike-slip character.

The body waves for this earthquake are also somewhat anomalous in that the amplitudes of long-period P waves are considerably smaller than those of the 09h 21m shock whereas the short-period P waves for both earthquakes are comparable in amplitude. These characteristics are illustrated in Figure 3-5 which shows observed long- and short-period P waves for both aftershocks recorded at GOL and CAR and Rayleigh waves

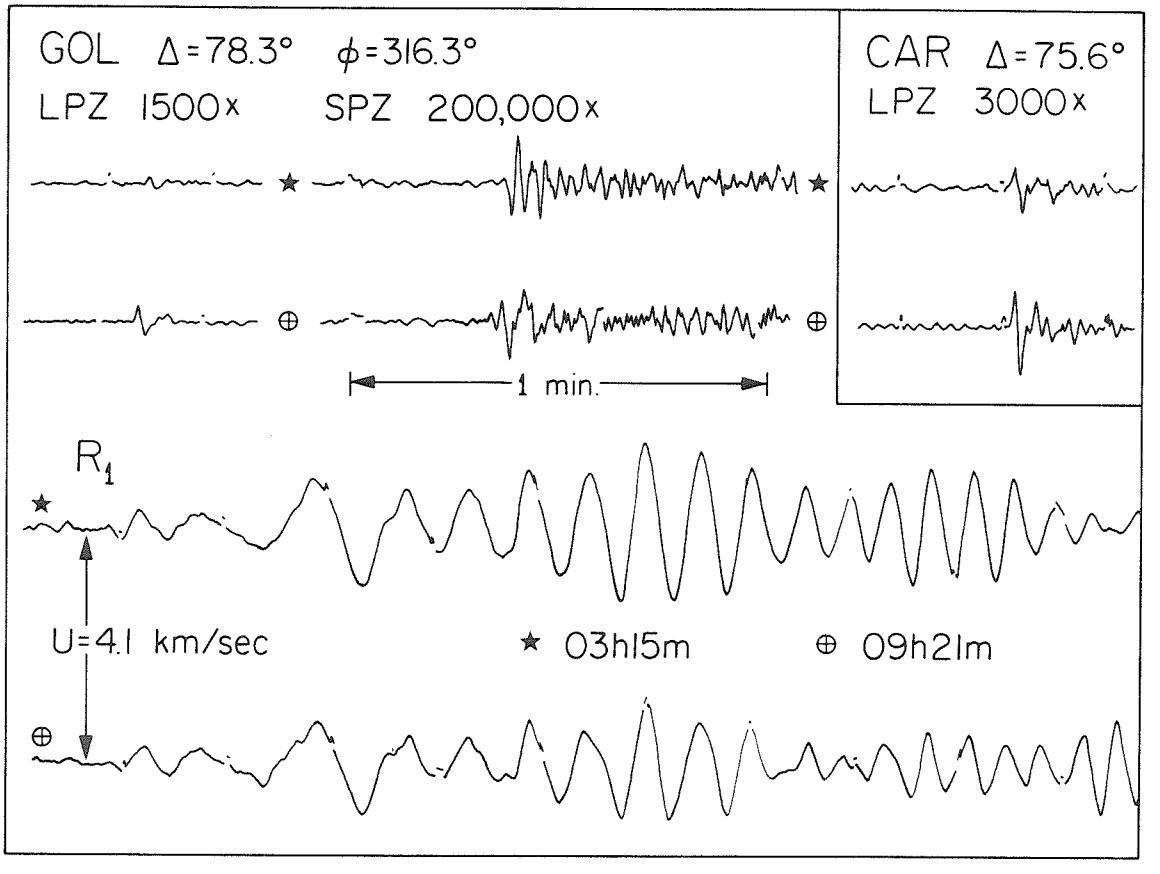

Figure 3-5. Short-period and long-period P waves and Rayleigh waves for the 03h 15m and 09h 21m aftershocks (denoted by stars and circles with cross respectively) recorded at GOL and CAR. Numbers after station abbreviations are instrument magnifications. Minute marks are indicated on long-period records along with group velocity of 4.1 km/sec on the Rayleigh wave trace.

of GOL. Note that for both earthquakes, the GOL short-period P waves have almost the same amplitude, whereas the long-period P wave of the 09h 21m event is about 2-1/2 times larger than the long-period P of the 03h 15m aftershock. A similar difference in amplitude is seen for the long-period P waves recorded at CAR. On the other hand the Rayleigh waves recorded at GOL are nearly equal in amplitude, especially at longer periods. Examining Figure 3-4, note that the P-wave focal mechanisms (Figure 2-11) predict almost identical Rayleigh wave amplitude at GOL (solid line is 09h 21m, broken line is 03h 15m). This implies that the seismic moments of the two earthquakes are nearly equal since the observed amplitudes are almost the same. The remainder of this section will be concerned with explaining these anomalies.

A number of preliminary source models were made in order to gain a feeling for the nature of the short-period records. As in the case of the 09h 21m event, it soon became apparent that two sources were necessary to account for the observed records. A rather successful model, SP25, was found by trial-and-error (Table 3-2) and used as a starting model for the waveform inversion program. After 10 iterations, the program could not significantly improve the fit, and the procedure was stopped (Table 3-4). The final model, SP27, is given in Table 3-2 and a comparison of observed records to synthetics computed for SP27 in the Angenheister crust is shown in Figure 3-6. The agreement between observed and synthetic is quite good for the first 5-7 seconds of record for most stations.

The right side of Figure 3-6 shows observed long-period records

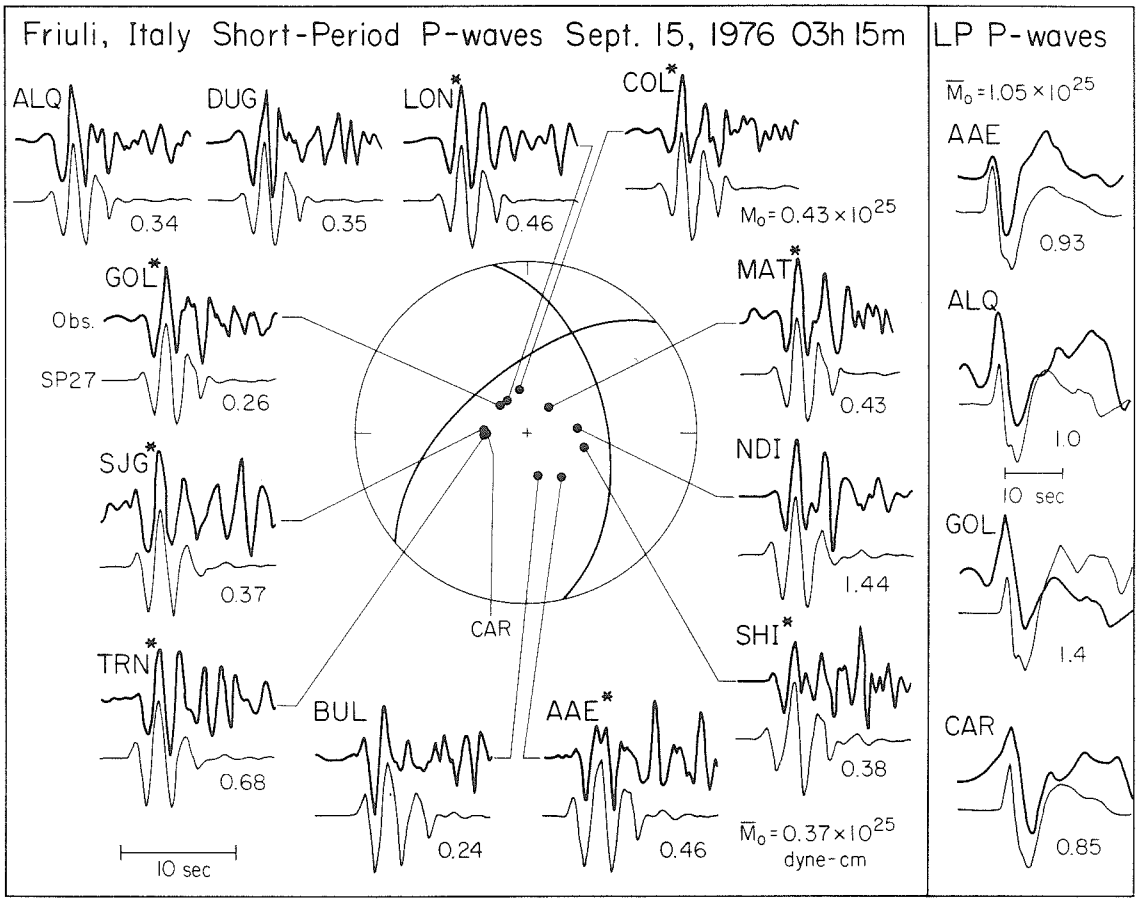

Figure 3-6. Observed seismograms (heavy line) of the 03h 15m earthquake compared to synthetics (light line) computed for model SP27 (Table 3-2) in the Angenheister crustal model (Table 2-4). Numbers below each synthetic are the seismic moments. Asterisks after the station abbreviations indicate that the station was used in the inversion program. Left side of the diagram shows the short-period data, right side, the long-period. Note the change of time scale.

Table 3-2. 03h 15m Source Models

	Starting Model SP25		Final Model SP27		SP30 LP
	1st	2nd	1st	2nd	Source
Strike (deg)	230	230	230	230	56
Dip (deg)	60	60	60	60	67
Rake (deg)	133	133	133	133	70
Depth (km)	4.5	4.5	3.77	4.23	4.0
M_o (10^{25} dyne-cm)	0.25	0.12	0.24	0.12	0.3
Time Lag (sec)	0.0	2.5	0.0	2.1	0.0
Rise (sec)	0.8	0.5	0.92	0.48	1.0
Top (sec)	0.2	0.3	0.0	0.78	2.0
Fall (sec)	0.5	0.5	0.84	0.26	1.0

compared to long-period synthetics computed using SP27. As can be seen, there is considerable discrepancy in phase and relative amplitude of the waveforms. In particular, the "glitch" on the downswing of GOL and ALQ is not found in the observed seismograms, and the first upswing at AAE is much too large on the synthetic. Also, the seismic moment computed for the short-period records (0.37×10^{25} dyne-cm) is about 2-1/2 times smaller than the amount inferred from long-period body waves (1.0×10^{25} dyne-cm). It appears that the short-period instrument has recorded only a fraction of the total radiation of the earthquake.

A closer examination of the Rayleigh data presented in Figure 3-4 suggests a way to improve the fit to the long-period body waves. Note that at each station, the Rayleigh waves written by both earthquakes are very similar in phase and amplitude, especially the long-period portion of the wavetrain. Bearing this out, the spectral density determinations at 50 sec period are quite consistent at each station. The available Rayleigh wave data do not allow an unambiguous determination of the mechanism, although the solution of the 09h 21m event seems to be favored. These observations suggest that the surface waves for both shocks were radiated by sources with similar mechanisms and seismic moments (about 1×10^{25} dyne-cm).

The long-period body waves also suggest that the mechanism of the two aftershocks are similar. In Figure 3-5, note the close correspondence between the waveforms recorded at CAR. Comparing the AAE records in Figures 3-3 and 3-6, one can see that except for the initial upswing for the 03h 15m shock, the long-period P waves are nearly

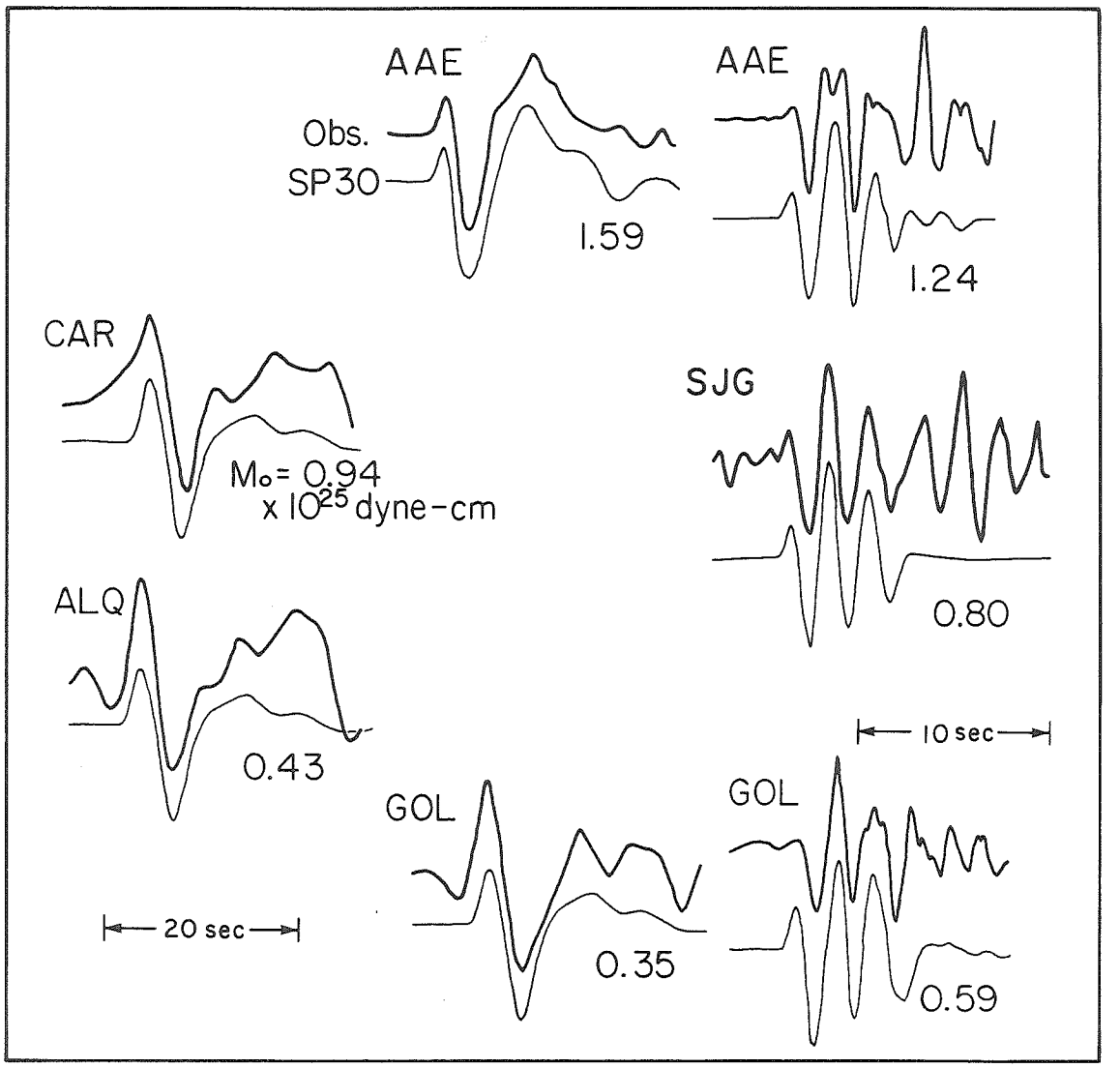

Figure 3-7. Observed seismograms (heavy line) of the 03h 15m earthquake compared to synthetics (light line) computed for model SP30 (Table 3-2) in the Angenheister crustal model, except station SJG which is calculated for a half-space (Table 2-4). Numbers under each synthetic indicate the seismic moment. Long-period data is on the left, representative short-period data is on the right. Note change of time scale.

identical. These observations suggest that although P-wave first motions for the 03h 15m event give the mechanism shown in Figure 2-11, the complete body waveforms and the surface waves are more consistent with a mechanism like that of the 09h 21m aftershock.

Taking the above observations into account, several trials were made to fit the long-period and short-period records simultaneously by adding a long-period component to model SP27. The mechanism of the 09h 21m event was adopted as the mechanism for the long-period component in order to fit the overall shape of the long-period body waves and the surface wave radiation pattern. A plausible model, SP30, is shown in Figure 3-7 and Table 3-2. Comparing Figure 3-7 to Figure 3-6, note that there is considerable improvement in the long-period fits. The short-period component (SP27) was not readjusted for model SP30 and consequently, quality of fit for the short-period records is somewhat diminished. The average seismic moments for both the long-period (0.83×10^{25} dyne-cm) and short-period (0.99×10^{25} dyne-cm) data are in reasonable agreement with each other and with the surface wave moment ($1\text{-}1.5 \times 10^{25}$ dyne-cm). Model SP30 preserves the observed long-period first motions of Figure 2-11, again note station AAE. However, the long-period source by itself predicts the wrong polarity at AAE (see Figure 3-3). Both the long-period and short-period components of model SP30 are necessary to fit the complete data set of the 03h 15m aftershock.

Table 3-3. Mainshock Source Models

	Chapter Two	Starting Model 15SP			Final Model 25Sp		
		1st	2nd	3rd	1st	2nd	3rd
Strike (deg)	76	76	76	76	76	76	76
Dip (deg)	75	75	75	75	75	75	75
Rake (deg)	80	80	80	80	80	80	80
Depth (km)	8.0	8.0	8.0	8.0	8.0	8.0	8.0
M_o (10^{25} dyne-cm)	2.9	0.14	0.29	0.57	0.12	0.27	0.3
Time Lag (sec)	-	-	1.4	2.8	-	1.15	2.25
Rise (sec)	1.0	0.7	0.7	0.7	0.5	0.67	0.72
Top (sec)	2.5	0.0	0.0	0.0	0.0	0.0	0.0
Fall (sec)	1.0	0.7	0.7	0.7	0.5	0.35	0.94

Mainshock

Compared to the records of the aftershocks, the short-period seismograms written by the May 6, 1976 mainshock are quite complex. It is interesting to note (Figure 3-8) that the records radiated in the P-wave loop direction (GOL, MSO, KTG, MAT) are quite similar in appearance, suggesting that receiver crustal structure has relatively little effect on P waveforms and that the principal influences are source properties and crustal structure.

The now familiar procedure was repeated for the mainshock: many trial-and-error models were constructed until a suitable starting model was found for use in the inversion program. The forward problem for the mainshock was time-consuming and laborious since it became apparent that to fit the waveforms, three or four point sources were required. With up to eleven parameters for each source, investigating the model space for a three source model becomes impossible to do manually. Model 15SP (Table 3-3) was found to reproduce the salient features of the GOL record, in particular, the number, timing and to a lesser extent, relative amplitude of the main pulses present on the seismogram. The observed record and synthetic are shown in the upper left corner of Figure 3-8. The inversion program was used to fine tune the parameters of the later, larger sources. The parameters of the first source were then refined by trial and error, keeping the other sources unchanged. The result is model 25SP (Table 3-3 and Figure 3-8). While this model is not completely successful in fitting the mainshock short-period records, the synthetics do reproduce the number and relative timing of

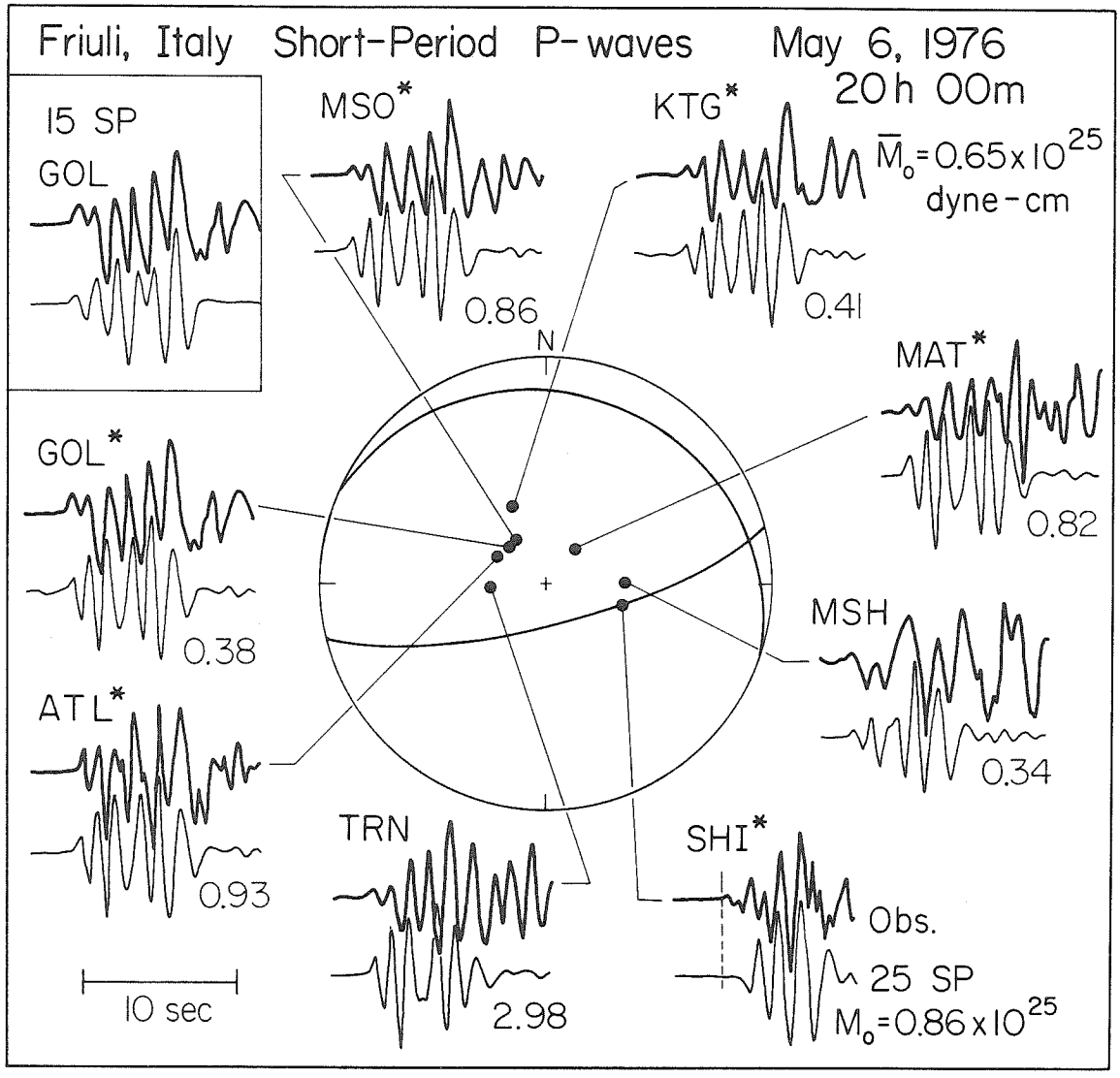

Figure 3-8. Observed short-period P waves for the mainshock (heavy line) compared to synthetics (light line) computed for model 25SP (Table 3-3) using the Angenheister crustal model (Table 2-4). Numbers below each synthetic indicate the seismic moment. Asterisks after the station abbreviation indicate that the station was used in the inversion program. The synthetic for GOL for the starting inversion model, 15SP, is shown in the inset at upper left.

the pulses observed on the real seismograms.

It is instructive to examine several stations in which the model does not work so well. Since the original model was made to fit the GOL records as was the final fine-tuning, seismograms at other azimuths would be expected to have the greatest discrepancies. For instance, the observed record at SHI begins too early relative to the synthetic. In preliminary models, the relative timing between sources (time lag in Table 3-3) was greater, causing the synthetic to be stretched in time, producing a better fit at SHI. In order to improve the fit at GOL, these original time lags were reduced by 0.46 sec; the dashed line in Figure 3-8 indicates the discrepancy. A reasonable explanation for this effect is that the sources are not at the same location on the fault plane (as is assumed in the calculation) but are at different geographical positions causing different time lags at each station. Considering that the aftershock zone and presumably the fault area is roughly 30 km by 15 km, in good agreement with the area which radiated the long-period body waves (Chapter Two), it is not surprising that each point source is in a different part of the fault plane.

The moment estimated from short-period records is about 0.65×10^{25} dyne-cm compared to 2.9×10^{25} dyne-cm determined from long-period body waves (Chapter Two). In addition, the agreement between the long-period synthetics computed for model 25SP and the observed data is poorer compared to that obtained in Chapter Two. As in the case of the 03h 15m aftershock, it appears that the short-period instruments have recorded only a portion of the energy radiated by the earthquake.

Table 3-4. Correlation Coefficients, N_i

Station	09h 21m		03h 15m	
	SP35	SP53	SP25	SP27
AAE	0.571	0.759*	0.691	0.658
COL	0.443	0.842	0.812	0.870
GOL	0.553	0.806	0.825	0.875
LON	0.327	0.845	0.817	0.923
MAT	0.491	0.557	0.858	0.840
SHI	0.383	0.509*	0.469	0.585
SJG	0.341	0.743	0.747	0.930
TRN	0.463	0.770	0.502	0.744
Overall	2.509	0.404	0.809	0.432

* All weights = 1.0 except stations AAE and SHI for 09h 21m aftershock.

Attenuation and Inversion

The effect of anelastic attenuation on synthetic waveforms has been discussed in general terms in the Introduction. The interaction between the Q-operator and time function can now be examined more closely in the light of the short-period inversion results. Figure 3-9 shows the GOL record for the 09h 21m aftershock compared to synthetics computed for various values of T/Q ratio in both the Angenheister crustal model and halfspace. Three features can be noted. First, synthetics computed with lower values of T/Q have enhanced high frequency characteristics. This is expected from the discussion of Figure I-2. Secondly, the seismic moment, inferred by comparing the observed and synthetic amplitudes, becomes smaller with lower T/Q. Finally, the duration of the waveforms does not change with different values of T/Q (note, in particular, the halfspace synthetics). This last result suggests that the time function cannot be lengthened significantly for the lower T/Q cases. A longer time function would reduce the amplitude thereby increasing the inferred seismic moment. Thus, the long-period versus short-period moment discrepancy found for the mainshock and 03h 15m aftershock cannot be attributed to an incorrect choice of T/Q, but must be a property of the source. To reduce this discrepancy using attenuation, the short-period T/Q ratio would have to be increased, contrary to recent measurements in the short-period band (Frasier and Filson, 1972; Der et al., 1980).

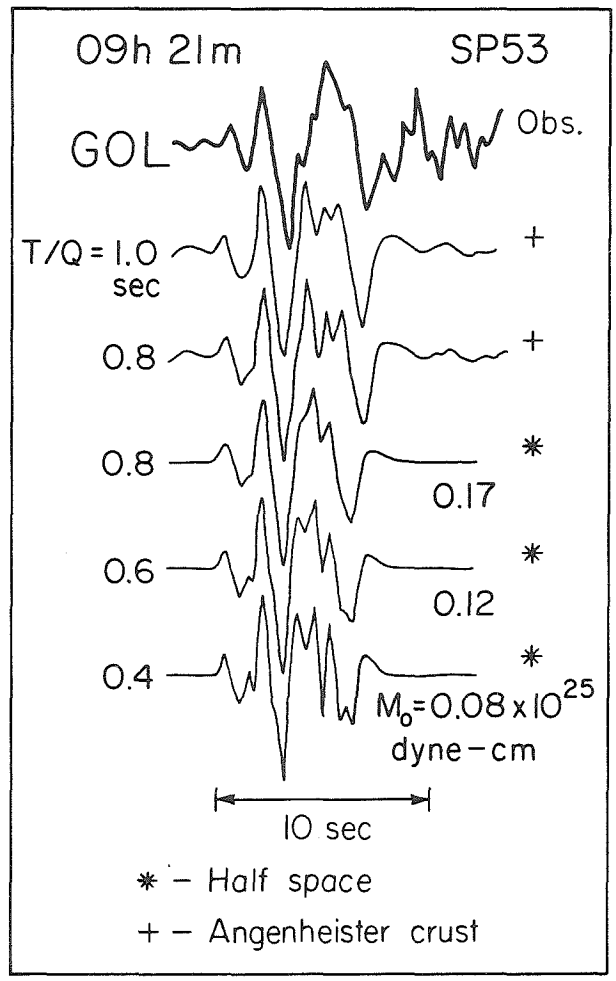

Figure 3-9. Observed short-period seismogram at GOL compared to model SP53 synthetics computed for various values of T/Q ratio.

Local Observations of the 09h 21m Aftershock

Local records of earthquakes have long been used by engineers to aid in the design of earthquake resistant structures. In recent years, seismologists have begun to exploit this kind of data to study seismic source properties (e.g., Heaton, 1978). This section will describe initial modeling work on accelerogram data obtained from the Friuli aftershock of September 15 at 09h 21m. This earthquake was chosen because of its relatively uncomplicated source and good set of local observations.

Following the May 6th mainshock, a number of accelerographs were deployed in the epicentral area (CNEN-ENEL, 1976) and these were in operation in September to record the major aftershocks. Records were obtained at several sites, two of which, Forgaria-Cornino and San Rocco, were selected for study. These stations, denoted as F and S respectively on Figure 3-10, are approximately 16 km southwest of the Rome epicenter of the 09h 21m aftershock (open circle). Three components of acceleration were recorded on Kinemetrics SMA-1 accelerographs and are available as Volume I Data: "Uncorrected Accelerograms" (CNEN-ENEL, 1977). The acceleration records were subjected to a parabolic base-line correction (Brady, 1966) before further processing. The first procedure was to integrate the accelerograms directly assuming zero initial velocity and displacement (Berg and Housner, 1961). This method seemed to enhance long-period noise present in the data. A second technique, that of first deconvolving out the original instrument response and then convolving in

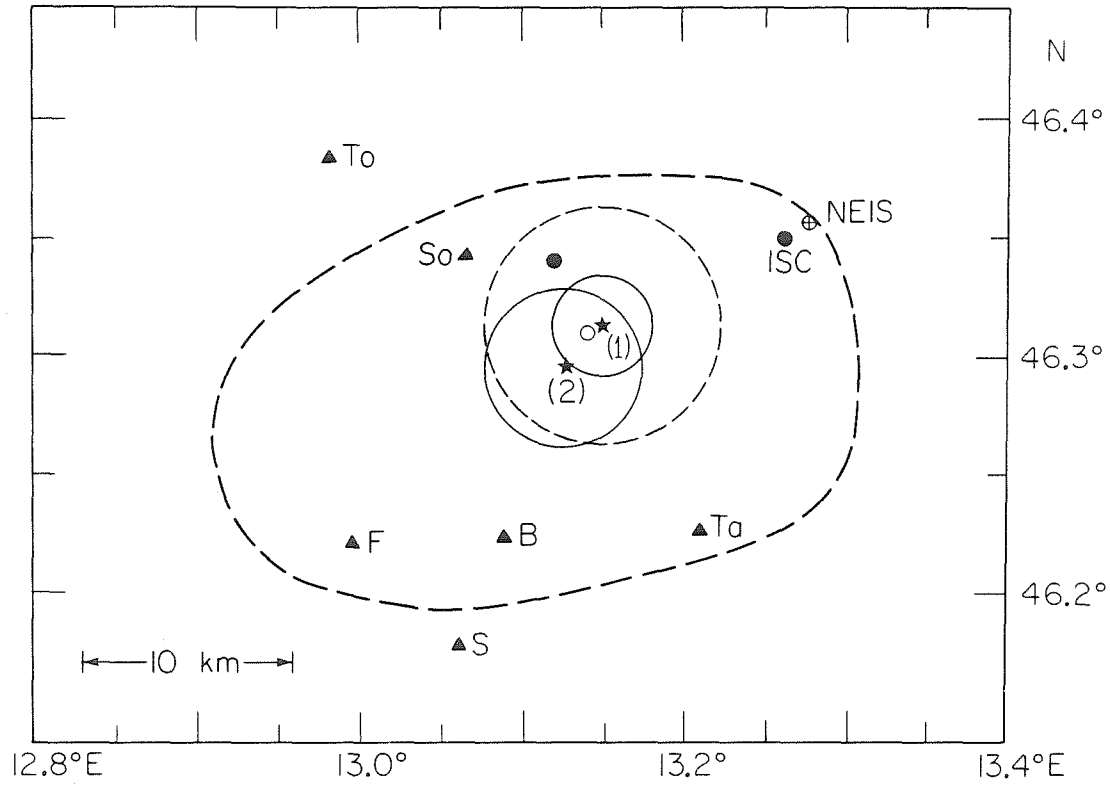

Figure 3-10. Locations of accelerograph stations (triangles) relative to Rome and ISC epicenters of the 09h 21m aftershock (open and filled dots). ISC and NEIS epicenters for the mainshock are indicated in the northeast corner of the aftershock distribution (heavy dashed line). Stars mark the position of the two sources inferred from waveform modeling. Solid circles drawn concentrically around the stars indicate the fault area of each source estimated in Chapter Four. Stations: B = Buia, F = Forgaria-Cornino, S = San Rocco, So = Somplago, Ta = Tarcento, To = Tolmezzo.

a long-period hypothetical response, had somewhat better success (referred to as D-R technique). Each instrument was approximated as a damped harmonic oscillator (Trifunac, 1972) of appropriate natural period and damping. These quantities are 0.04 and 50-60 percent critical and 3.0 sec and 70 percent critical for the original and hypothetical responses, respectively. Notice that the D-R record of the east-west component at Forgaria (Figure 3-11) is essentially a filtered version of the velocity trace above it. Horizontal records were rotated to SH and SV components assuming the Rome epicenter and the station locations shown in Figure 3-10 (CNEN-ENEL, 1977). There is some uncertainty in the location of the San Rocco station. Personal communication from Prof. M. Basili relates that the station is within 1 km of the Forgaria-Cornino site, in agreement with the location given in CNEN-ENEL (1976). This is contrary to the location listed in CNEN-ENEL (1977). Similarity between synthetics computed for both sites indicate that this uncertainty is not critical.

Synthetics were computed for a point shear dislocation source in a layered halfspace. The Cagniard-de Hoop formalism was used to compute the medium response for the appropriate generalized rays (Helmberger, 1968; Helmberger and Malone, 1975; Helmberger and Harkrider, 1978). The high frequency approximation (Helmberger, 1974) was assumed since the records are essentially in the far-field range of the earthquake (see Heaton, 1978, for a detailed discussion). Ground displacement was computed by convolving the far-field source time history with the medium response. The hypothetical instrument response was convolved with the

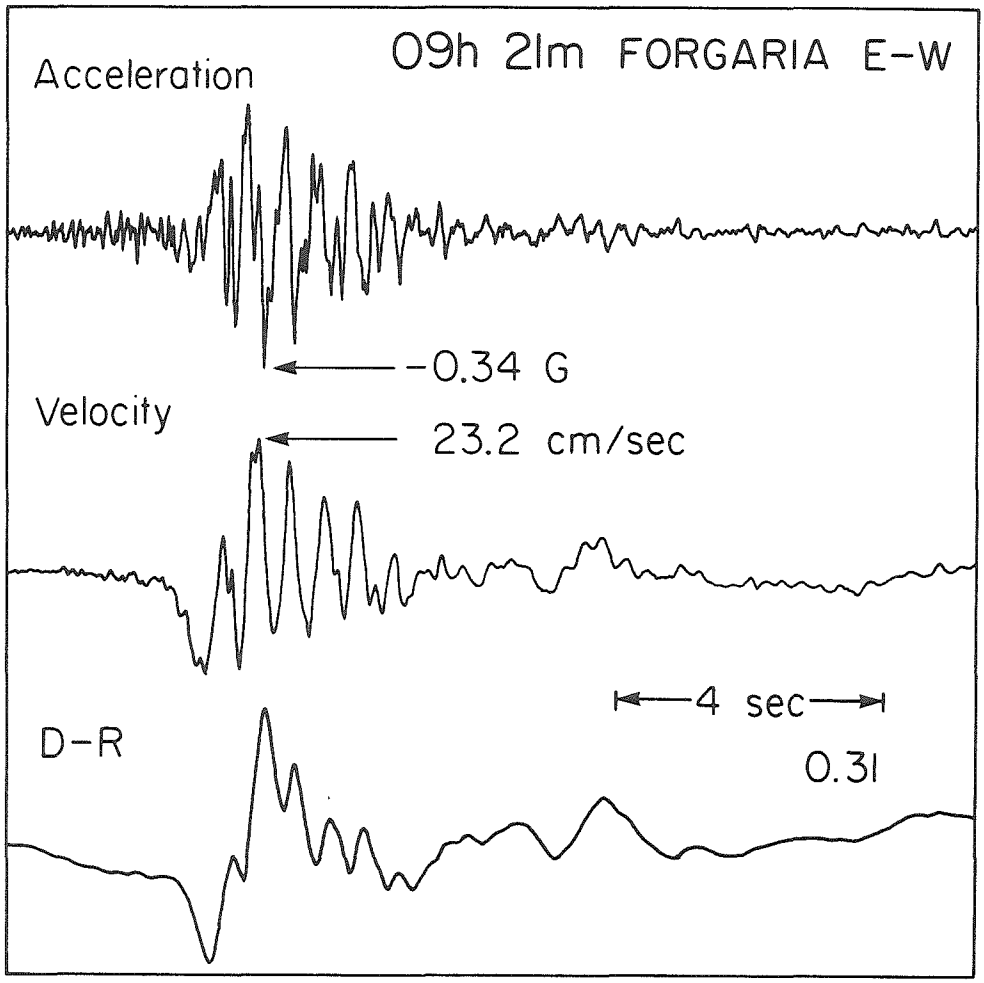

Figure 3-11. Acceleration, velocity and D-R records of the east-west component at Forgaria-Cornino.

synthetic ground displacement to produce D-R synthetics.

The first experiment was a direct test of model SP53, which was obtained by modeling teleseismic short-period records of the 09h 21m aftershock (Table 3-1). To simplify calculations, model SP53 was modified by placing both point sources at 6 km depth; all synthetics were computed at a range of 16 km. Model SP53 predicts the correct first motions but produces synthetics which are much too long compared to the observations. To remedy this, the time separation between the sources was decreased from 1.3 sec to 0.6 sec, keeping the other parameters of SP53 unchanged. This new model is designated as SP53E and synthetics at Forgaria and San Rocco are shown in Figure 3-12. Model SP53E has certain successes and some obvious shortcomings. It correctly predicts the observed first motions of the S phase (denoted by arrows) and also the duration of the vertical and SH components. Note that the observed SH components at both stations are similar to each other. The model is most successful in fitting the waveform and duration of these records. The prominent, pulse-like Rayleigh wave on the vertical component at Forgaria is also correctly predicted. There is, however, considerable waveform disagreement for the vertical component at San Rocco indicating variability in local crustal structure. The overly long duration of the SV synthetics is particularly troublesome. The SV and vertical waveforms are controlled by the Rayleigh wave and an arrival arising from SV to P conversions at the free surface (Kawasaki et al., 1973). Several attempts to modify this phase by changing the crustal structure were unsuccessful. In fact, structures other than a

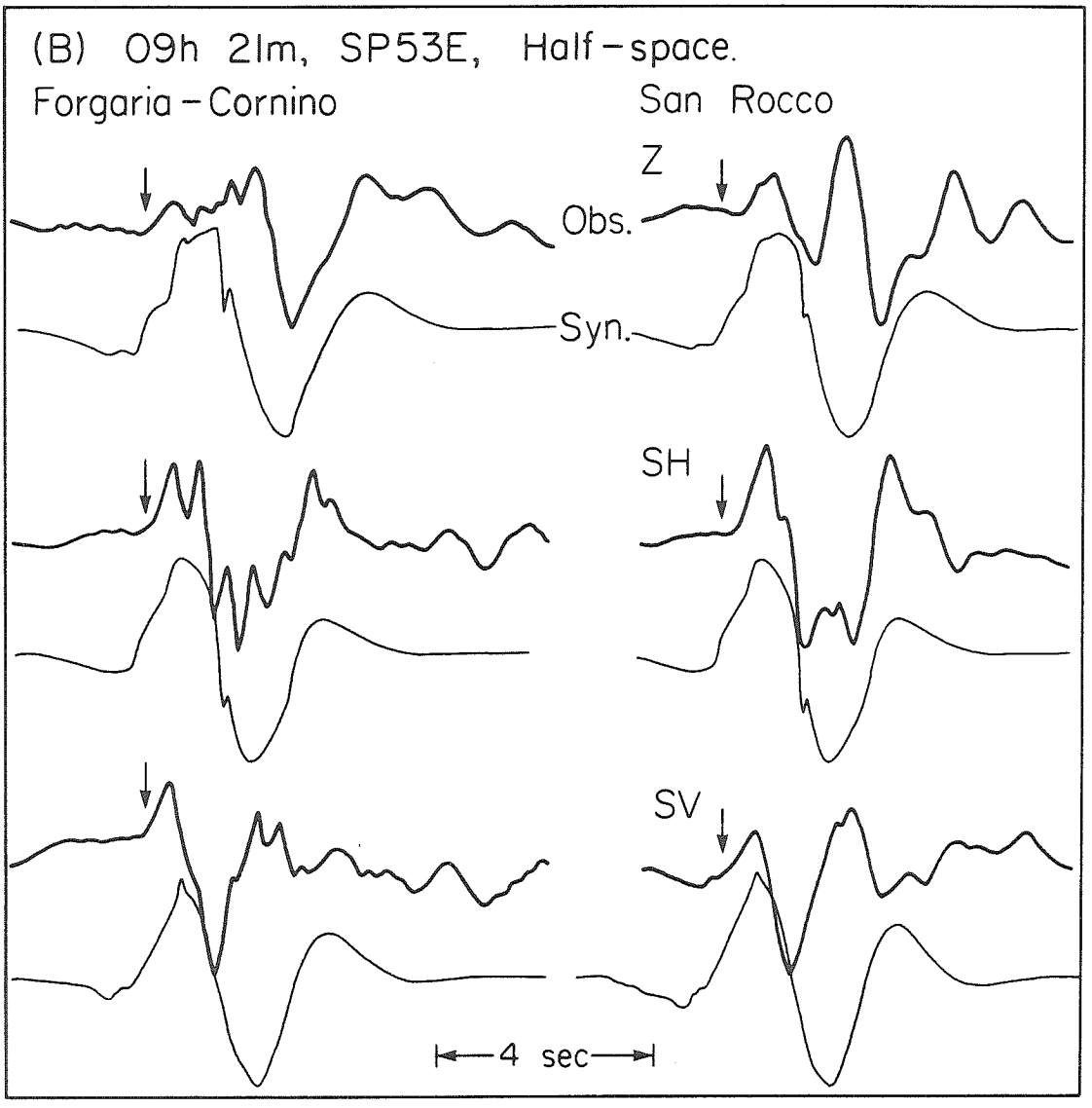

Figure 3-12. Observed and synthetic D-R records at Forgaria-Cornino and San Rocco for model SP53E. From top to bottom, vertical, transverse and radial components are shown. S-wave arrival is indicated by arrows.

halfspace usually resulted in poorer agreement between the observations and synthetics. Model SP53E is successful to the extent that it reproduces the basic long-period characteristics of the observed records. On the other hand, the synthetics leave much to be desired in terms of fitting the high frequency details of the waveforms.

The location of the second point source relative to the first can be inferred from the time lag between sources observed at each accelerograph site (0.6 sec for both stations). These rays travel almost horizontally. The time lag (1.3 sec), inferred from teleseismic body waves which exit the source region at nearly vertical take-off angles, is approximately the absolute time difference between sources. Triangulation can be used to find the relative location of the two sources using the relation for each station:

$$\Delta_2 = \Delta_1 + (\delta T - \delta T_o)\beta$$

where: Δ_1 = distance to first source (Table 4-2)

δT = time lag at station (0.6 sec)

δT_o = absolute time separation (=1.3 sec)

β = shear velocity (=3.5 km/sec)

These locations are plotted as stars in Figure 3-10. The second source is 2.7 km south southwest of the first, 13 km from Forgaria. The rupture velocity is found to be 2.08 km/sec, a minimum estimate since there may have been a pause between the sources. Further discussion of the implications of the teleseismic and local modeling in terms of source processes and tectonics will be presented in Chapter Four.

Chapter Four

Earthquake Source Processes and Tectonics

Friuli Earthquake Source Parameters

A comparison of the long-period and short-period time functions of the Friuli earthquakes is shown in Figure 4-1. The time function of each short-period event determined in Chapter Three is shown as a solid line. The dashed lines represent the long-period time functions found in Chapter Two for the mainshock and 09h 21m aftershock and the inferred "long-period" source for the 03h 15m aftershock (Chapter Three). The starting time of the later time functions conform to the time lags found from teleseismic data. Each individual time function is drawn in such a way that the area under the curve is proportional to seismic moment. All three earthquakes are drawn to a common time and moment scale. Note that the moment of the short-period events in each case amounts to only a fraction of the moment inferred from the long-period observations. As was pointed out in Chapter Three, the good agreement in moment and waveform for both long- and short-period data for the 09h 21m event suggests that the source, and not a propagation effect, is responsible for the long-period versus short-period moment discrepancy observed for the other earthquakes.

Following the procedure outlined by Ebel et al., (1978), an estimate can be made of the radius of a circular fault which radiates the far-field time function. Total duration, t_c, is the sum of the rise

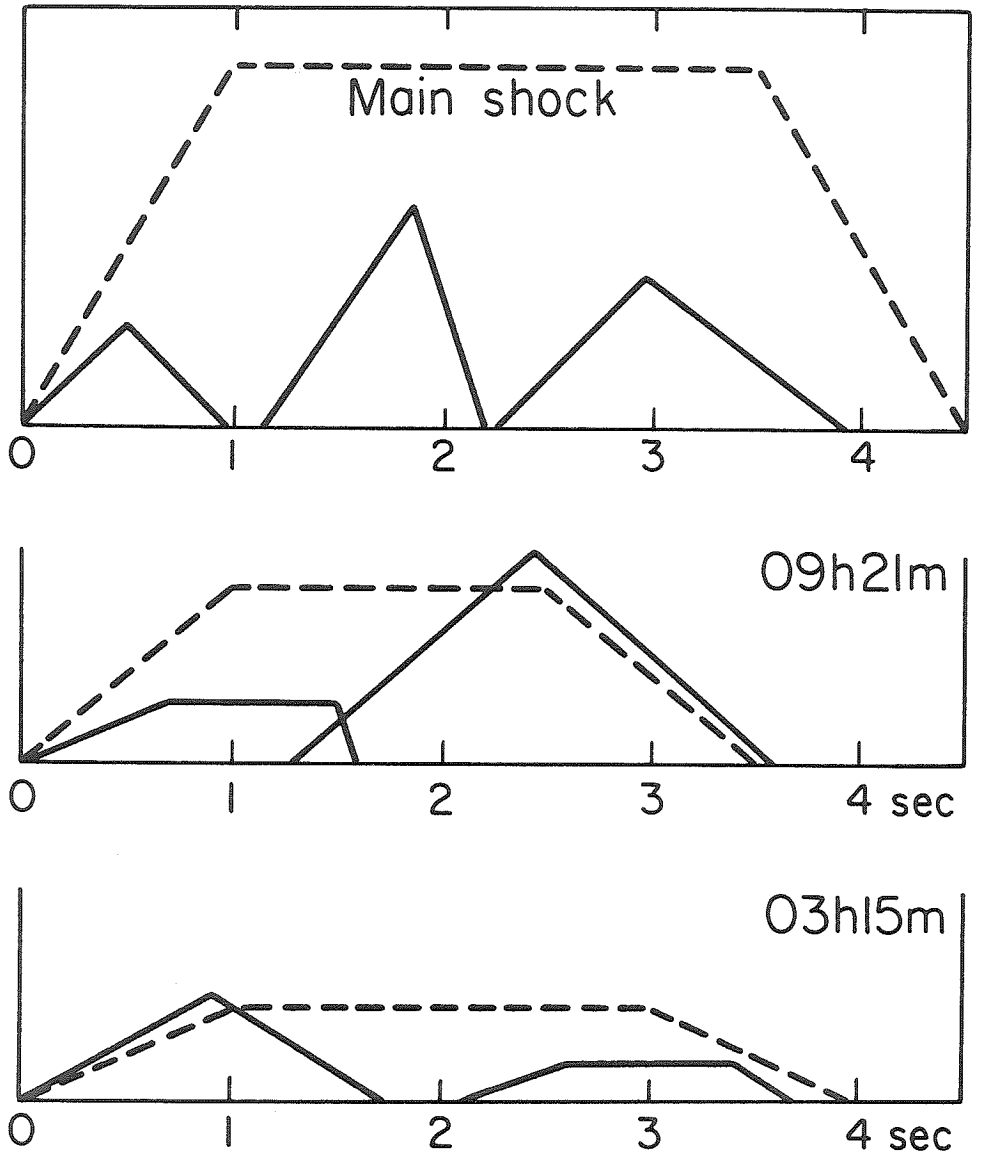

Figure 4-1. Comparison of observed far-field time functions. Areas under the time functions are scaled to the seismic moment of each event. Note time scale in seconds. Solid lines represent the time functions derived from modeling short-period records. Dashed lines are the long-period time functions found in Chapter Two for the mainshock and 09h 21m aftershock and the long-period source for the 03h 15m earthquake (Chapter Three).

time (first term) plus the rupture time (last two terms):

$$t_c = 16a/7\pi\beta + a/V + (a/\alpha)\sin\theta$$

where a is the radius of a circular fault, V is the rupture velocity, α and β are the P-wave and S-wave velocities in the source region and θ is the angle between the normal to the fault plane and the ray take-off angle. Chung (1978) discusses the derivation of this expression; Geller (1976) derives the form of the rise time term. t_c is a measured quantity found by summing the rise, top and fall times of the source time function. The circular fault radius, a, can be calculated assuming values for α (= 6.0 km/sec), β (= 3.5 km/sec) and V (=3.0 km/sec). For the 09h 21m aftershock and the mainshock, the inferred fault planes dip gently northward (15^o-30^o); thus the normal to the fault plane is nearly vertical. The take-off angles to the observing stations are in the range 20^o-40^o from the downward vertical; hence θ is small (set to 30^o for the calculations). For the 03h 15m earthquake, the nodal planes dip at a much steeper angle and it is unclear which plane is the fault plane. For this earthquake, θ was arbitrarily set at 45^o. The expression for seismic moment (a measured quantity), $M_o = \mu D_o S$, where S is the fault area (= πa^2), allows calculation of the average dislocation (D_o) assuming a value for the rigidity ($\mu = 3 \times 10^{11}$ dyne/cm^2). The stress drop for a circular fault, $\Delta\sigma = (7\pi/16)\mu D_o/a$, can then be estimated (Kanamori and Anderson, 1976). These quantities, calculated for each earthquake, are listed in Table 4-1.

Source dimensions for the mainshock and 09h 21m aftershock have been estimated in Chapter Two by comparing observed records to

Table 4-1. Source Parameters

	Source Duration (sec)	Seismic Moment x 10^{25} (dyne-cm)	Fault Radius (km)	Fault Area (km^2)	Dislocation (cm)	Stress Drop (bars)
			09h 21m			
Chap. 2	3.5	1.0	5.6	100.0	33	24
SP53 1st	1.64	0.18	2.6	21.6	28	44
2nd	2.30	0.59	3.7	42.6	43	35
			03h 15m			
SP27 1st	1.76	0.24	2.7	22.4	36	56
2nd	1.52	0.12	2.3	16.7	24	43
			Mainshock			
Chap. 2	4.50	4.0	11.3	400.0	33	12
25SP 1st	1.00	0.12	1.6	8.0	49	126
2nd	1.02	0.27	1.6	8.4	107	276
3rd	1.66	0.30	2.7	22.2	45	51

synthetics computed for a finite fault and are found to be 400 km^2 and 100 km^2 respectively. For the 09h 21m aftershock, the combined source area of the two events inferred from the short-period records is about 65 percent of the area obtained from long-period data (Table 4-1). Given the assumptions involved in both calculations, this discrepancy is probably not significant. The short-period source area for the mainshock, on the other hand, is a factor of 10 smaller than the long-period area. Allowing for the uncertainties in these results, it appears that the short-period radiation comes primarily from limited regions of the fault plane whereas the long-period seismograms record the overall motion of the earthquake.

The salient point of Table 4-1 is that the overall stress drop estimated from long-period records, which presumably sample the whole faulting process, is consistently lower than the stress drops calculated for each individual short-period event. The first two events of the mainshock had quite high stress drops but overall, the earthquake was characterized by low stress drop. While the stress drops quoted in Table 4-1 must be regarded as rough estimates due to the assumptions involved, it seems clear that these earthquakes are made up of a number of episodes of high stress drop from limited regions of the fault plane superimposed on an obbligato of smooth rupture.

There is a growing body of observations which suggest that massive failure at the initiation of faulting is a feature common to many shallow earthquakes. Burdick and Mellman (1976) found that most of the body waves radiated by the 1968 Borrego Mountain, California earthquake

came from a small patch on the fault plane which had a radius of 8 km. The stress drop in this zone was estimated to be 96 bars. Ebel (1980) concludes that the short-period seismograms of this earthquake record radiation from two regions, one of 7.7 km and the other of 4.0 km diameter, having stress drops of 436 bars and 366 bars respectively. Other observations of this phenomenon have been made by Hartzell and Brune (1979) for the 1975 Horse Canyon, California earthquake and Bache et al., (1980) for the Pocatello Valley, Idaho shock.

Circles representing the fault areas calculated above for the 09h 21m aftershock (Table 4-1) are plotted in Figure 3-10. The solid circles represent the fault area of each short-period source drawn concentrically about the epicenters obtained by modeling local records. The dashed circle indicates the fault area determined from long-period data (Chapter Two). The geometry depicted in this diagram suggests that the first short-period source initiated the earthquake and by its failure put additional stress on the impending fault plane of the second event which broke in short order. That the faulting of the first event ended suddenly is suggested by the sharp fall of its time function (=0.1 sec, Table 3-1). While this value is subject to considerable uncertainty, it is still nearly an order of magnitude less than the other time function parameters and thus seems to indicate abrupt termination of event one faulting.

Of particular interest is the result that the time function obtained from teleseismic modeling also fits the accelerograph data. This observation has implications for the nature of rupture propagation

Figure 4-2. (a) Far-field radiation from a circular fault surface in which rupture begins at the center. The figures in the left column represent the P wave and those in the right column the S wave. The time required for the rupture to travel from the center to the edge of the fault surface has been chosen as the unit of time. The solid lines represent the signal if the fault displacement is constant over the fault surface and the dashed lines represent the signal if the fault displacement varies as given by Eshelby (1957). (b) Far-field radiation from an elliptical fault surface of eccentricity 0.6 in which rupture begins at a focus. Sketch in the upper left-hand corner represents this ellipse; the vertex of the angle is the point of initial rupture. The unit of time is the time required for the rupture to travel a distance equal to the semi-minor axis of the ellipse. Several cases of the variable $\chi = (V/c)\sin\theta$ are shown where V and c are the rupture and wave velocities respectively (after Savage, 1966).

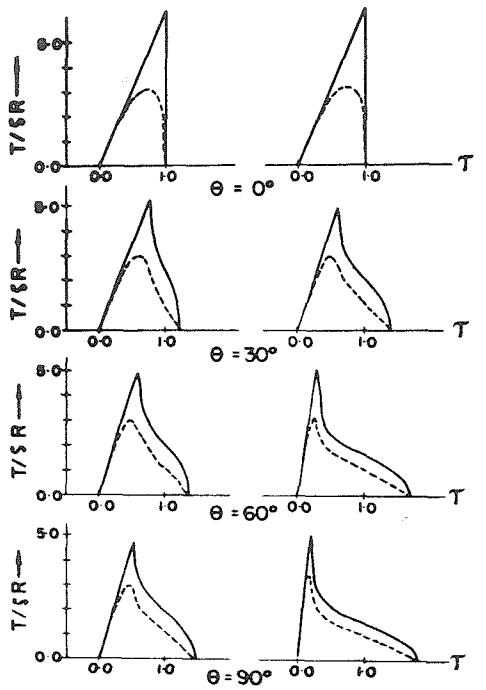
(a)
T/ρR
θ = 0°
θ = 30°
θ = 60°
θ = 90°
τ

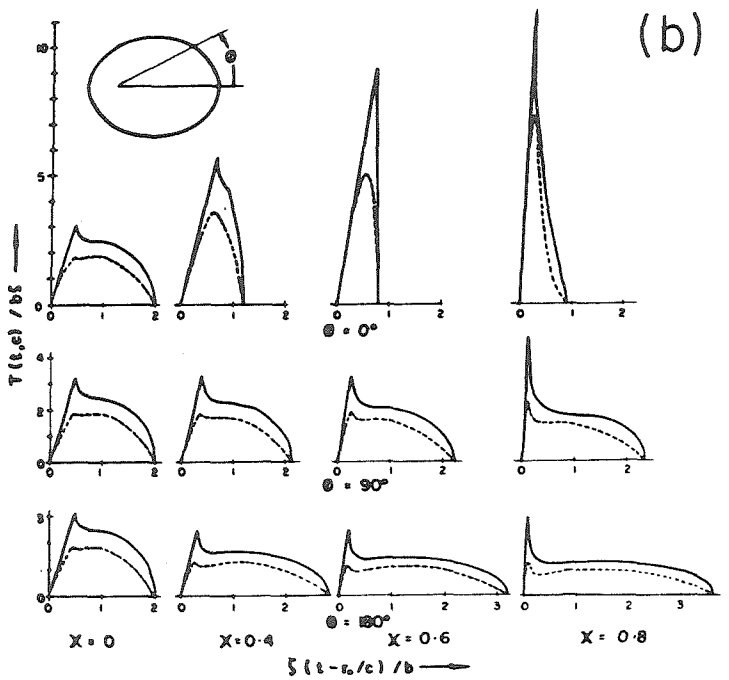
(b)
T(t,c) / bρ
θ = 0°
θ = 90°
θ = 180°
X = 0
X = 0·4
X = 0·6
X = 0·8
ζ (t - r₀/c) / b

since waves traveling to teleseismic distances leave the source in a direction approximately perpendicular to those that travel to the accelerograph stations. We will focus on the second source of the 09h 21m aftershock since it dominates the radiation from the earthquake. Figure 4-2a shows theoretical time functions for circular faults calculated for various values of θ (defined above) based on the formulation of Savage (1966). The unit of time is the time required for the rupture to travel from the center to the edge of the fault. The left and right columns give the P-wave and S-wave time functions respectively. The symmetrical form of the observed teleseismic time function (Figure 4-1) is fit reasonably well by the P-wave time function for $\theta = 30^{o}$, the value suggested above. On the other hand, the circular fault model predicts that SH stations at local distances should see the S-wave time function for $\theta = 90^{o}$ which is antisymmetrical and longer in duration than at teleseismic distances. Given that the teleseismic time function duration is 2.3 sec, the circular fault model predicts that the local SH time function should 3.4 sec long (t_c = (0.4, 0.0, 3.0sec)). As expected, synthetics computed with this value do not fit the observed records.

On the other hand, unilateral fault propagation along a line normal to the direction to the accelerograph stations (i.e., northwesterly) would predict equal apparent duration at both local and teleseismic receivers. Figure 4-2b shows P-wave time functions for elliptical fault planes for several values of ϕ (defined in the figure) and $\chi = (V/c)\sin\theta$. Note that the duration is approximately the same for $\phi = 90^{o}$

at both teleseismic ($\chi \sim 0.4$) and local ($\chi \sim 0.8$) distances. The shape, however, is quite different from the teleseismic inversion results (Figure 4-1). At the present stage of modeling, it is unclear how this dilemma can be resolved.

Aftershock Energy Release

A notable feature of the Friuli earthquake sequence is the large size of the September aftershocks relative to the mainshock. The seismic moment of the September 15 (09h 21m) aftershock is nearly one-third the moment of the mainshock. Besides that earthquake, there were three other large events between September 11 and 15, 1976 (Table 2-1). To provide a quantitative measure of the energy release of the aftershock series, the seismic moment (M_o) was estimated from local magnitude (M_L) using the relation: $\text{Log } M_o = 15 + 1.7M_L$ (Wyss and Brune, 1968). The moment sum of the Friuli earthquake sequence from May 1976 through December 1977 is slightly over 8×10^{25} dyne-cm, of which $3\text{-}4 \times 10^{25}$ dyne-cm was released during the mainshock (Figure 4-3). Thus, the aftershock sequence was considerably more energetic than the mainshock.

The anomalously high aftershock activity of the Friuli sequence can be placed in perspective by comparing it to the somewhat larger 1971 San Fernando, California earthquake ($M_o = 8.6 \times 10^{25}$ dyne-cm; Langston, 1978). Figure 4-4 shows the body wave magnitudes (m_b) as reported by the NEIS for the larger aftershocks of the two sequences plotted versus time after the mainshock. Notice, in particular, the greater activity of the Friuli sequence for the periods between 0 and 20 days and 130 to

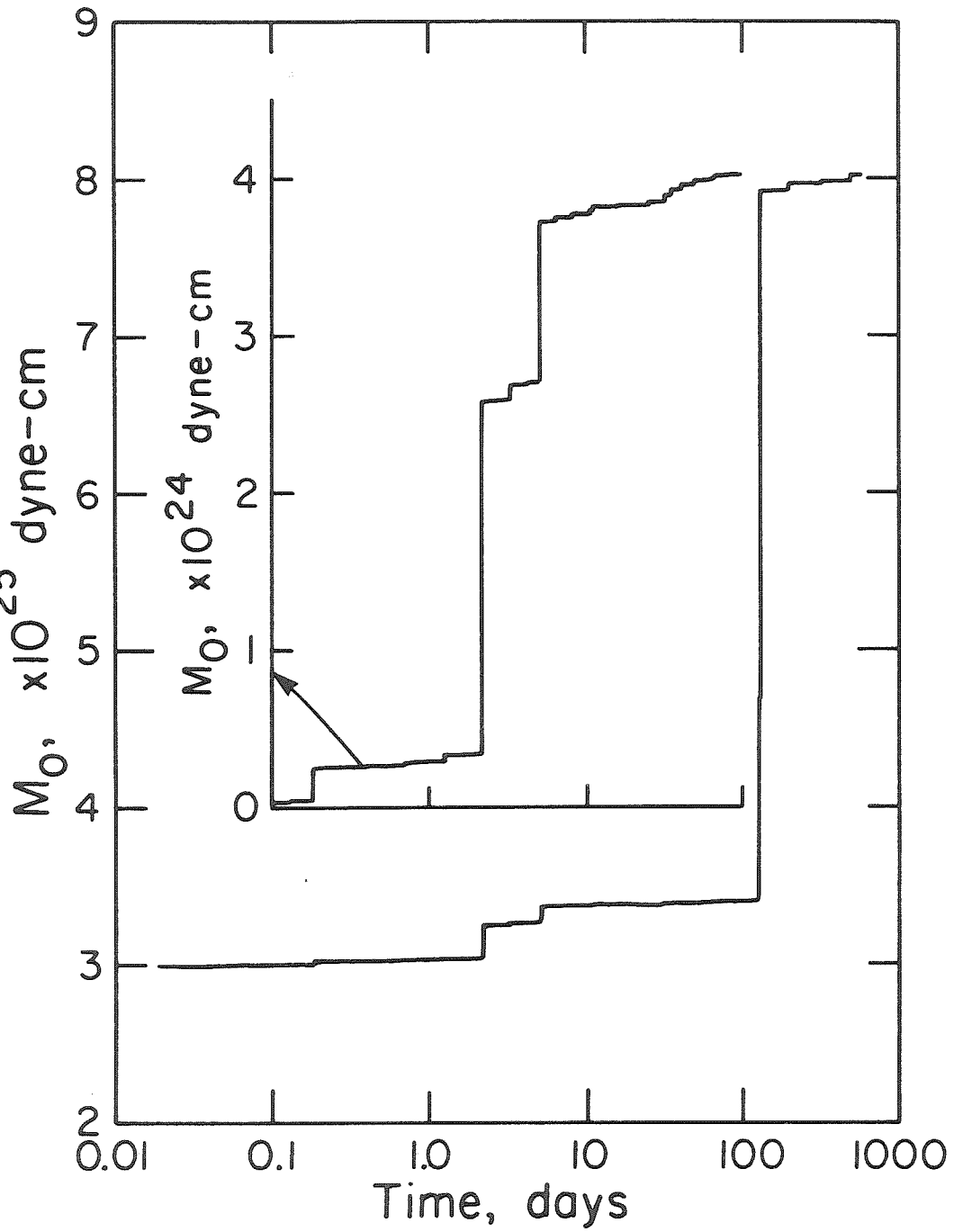

Figure 4-3. Summation of seismic moment with time for earthquakes of the Friuli sequence calculated from an empirical relation between local magnitude and seismic moment (see text).

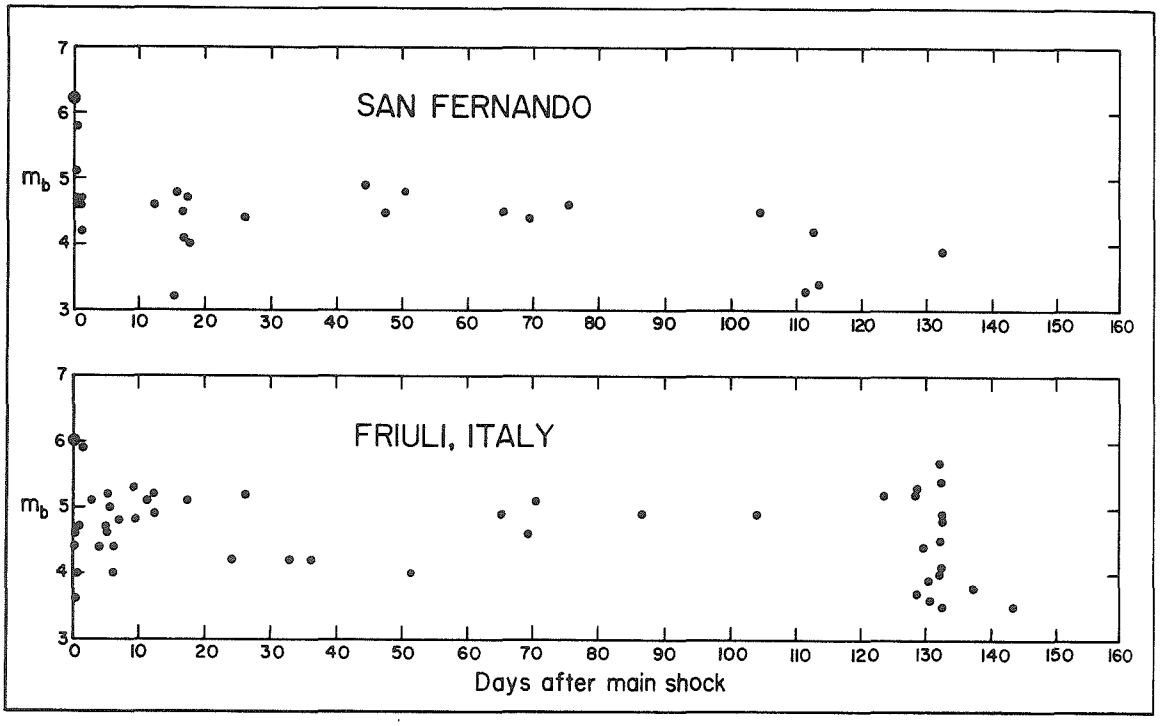

Figure 4-4. Body wave magnitude (m_b) versus time after the mainshock for the Friuli and San Fernando earthquakes.

140 days. During the time between 20 and 120 days, both numbers and magnitudes of the events are nearly the same. Hadley and Kanamori (1978) estimated the moment sum of the aftershocks of the 1971 San Fernando earthquake to be 3.5×10^{24} dyne-cm, about two orders of magnitude smaller than the mainshock. An enlargement of the energy-release curve for the first 100 days of the Friuli aftershock sequence is shown as an inset in Figure 4-3. This curve is directly comparable to Figure 2 of Hadley and Kanamori (1978). Comparing the two diagrams, note that the moment sum for the Friuli sequence is somewhat larger than for San Fernando, and that most of the energy release came during two large earthquakes.

The differences in mode of strain release between the Friuli and San Fernando earthquakes is evident in the teleseismic body waves. The San Fernando P waveforms are considerably more complicated than those for Friuli. Compare the data shown in Figure 2-9 to observations reported by Langston (1978; his Figure 1). Langston modeled the San Fernando records by upward propagating fault rupture on a plane that changes dip near the surface. Recently, Heaton (1980) has suggested that local and teleseismic data can be best fit by two en echelon fault planes. On the other hand, the Friuli data can be modeled by slip on a single fault plane.

It appears that the mechanical properties of the San Fernando and Friuli seismic zones are rather different. In the case of San Fernando, most of the energy was released by a single large, complex earthquake. For Friuli, the seismic energy was liberated in a series of smaller,

relatively simple earthquakes. Had the September aftershocks occurred within a few tenths of seconds of the mainshock instead of several months later, the correspondence between the Friuli and San Fernando earthquakes might have been quite striking in both waveform and seismic moment. There are tantalizing hints of similar behavior during past Friuli earthquakes. For the earthquake of March 26, 1511, in particular, felt reports collected by Ambraseys (1976a, b) mention that the mainshock was followed by a series of strong aftershocks, especially those of June 6 and August 8, 1511.

The anomalously high aftershock energy release of the Friuli sequence can be better appreciated by comparing it to other sequences. Mainshock seismic moment, cumulative aftershock moment and the ratio of these quantities for several moderate-sized, shallow earthquakes are listed in Table 4-2. Most of these shocks occurred in California where excellent seismic networks are in place. The values of M_o^A/M_o^M vary from 1.2 for Friuli to 3.8×10^{-4} for the Santa Barbara, California earthquake. A typical range seems to be 0.01 to 0.10. Note that if the aftershocks after September 11 are discounted, the Friuli value is within the range of typical events. Of particular interest are the unusually low values for the Santa Barbara and Point Mugu shocks. These earthquakes are located about 75 km apart along the southern California coast. In contrast, the Oroville earthquake, in the Sierra Nevada foothills, has a value significantly higher than the other California events. This earthquake may be atypical in that it occurred in an area of low historical seismicity apparently in relation to the filling of a

Table 4-2. Source Data for Selected Earthquakes

Earthquake	m_b	M_S	Duration (sec)	M_o^M x10^{25}	M_o^A dyne-cm	M_o^A/M_o^M
Haicheng (H)	6.4	7.4	7.0	30.0	2.0	0.07
Friuli (F)	6.0	6.5	4.5	4.0	4.7	1.2
				4.0	0.4	0.1
09h 21m (FA)	5.4	5.9	3.5	1.0		
Koyna (K)	6.0		6.5	3.2		
Gibbs F.Z. (G67)	5.5	6.5	17.0	20.0		
(G74)	5.8	6.9	22.0	50.0		
Parkfield	5.8	6.4		1.4	0.037	0.03
El Golfo (E)	6.3	6.3	4.0	5.0		
Truckee (T)	5.4		3.0	0.72	0.12	0.17
Borrego Mtn. (B)	6.1		4.5	11.2	0.124	0.01
San Fernando	6.2	6.5		8.6	0.35	0.04
Point Mugu	5.7	5.2		1.6	0.004	0.0025
Oroville (O)	5.8	5.6	3.0	0.57	0.19	0.33
Santa Barbara (S)	5.5	5.6	6.0	1.1	0.00042	0.00038
Coyote Lake	5.4	5.7		0.6	0.006	0.01
Imperial Valley	5.7	6.9		16.6	0.462	0.03

Sources for Table 4-2.

Haicheng, China (2/5/75) - Gu *et al.* (1976), this study.

Friuli, Italy (5/6/76) - Cagnetti and Pasquale (1979), this study.

Koyna, India (12/10/67) - Langston (1976)

Gibbs Fracture Zone (2/13/67, 10/16/74) - Kanamori and Stewart (1976)

Parkfield, California (6/28/66) - Tsai and Aki (1969); McEvilly *et al.* (1967)

El Golfo, Mexico (8/7/66) - Ebel *et al.* (1978).

Truckee (9/12/66) - Greensfelder (1968); Tsai and Aki (1970); Burdick (1977)

Borrego Mountain, California (4/9/68) - Allen and Nordquist (1972); Burdick and Mellman (1976); Ebel (1980).

San Fernando (2/9/71) - Langston (1978); Hadley and Kanamori (1978)

Point Mugu, California (2/21/73) - Stierman and Ellsworth (1976)

Oroville, California (8/1/75) - Langston and Butler (1976); Morrison *et al.* (1976); Bakun and Lindh (1977).

Santa Barbara, California (8/13/78) - Whitcomb *et al.* (1979); Wallace *et al.* (1981).

Coyote Lake, California (8/6/79) - Uhrhammer (1980).

Imperial Valley (10/15/79) - Hutton *et al.* (1980).

large reservoir. The Parkfield, Borrego Mountain, San Fernando, Coyote Lake and Imperial Valley earthquakes have almost identical M_o^A/M_o^M ratios, despite the fact that they occur in different tectonic settings.

There is no correlation between M_o^A/M_o^M ratio and either magnitude or source depth (all of these earthquakes are shallow). More likely, these numbers reflect differences in the state of stress in the crust following the mainshock. In the case of the Santa Barbara and Point Mugu shocks, virtually all of the stress was relieved in the mainshock. Relatively high levels of stress, on the other hand, remained after the Friuli and Oroville earthquakes which was subsequently released as aftershocks.

Additional information on the stress state of the Friuli fault zone can be inferred from the areal pattern of aftershock energy release. Figure 4-5 shows the cumulative seismic moment for all aftershocks from May 6 to September 9 plotted by 0.05^o square blocks. Only blocks in which ΣM_o exceeds 0.1×10^{23} dyne-cm are indicated. Location uncertainties make precise statements impossible, yet several general features are apparent. First, notice the low energy release around the mainshock epicenter. This region may correspond to the fault area of the initial short-period source, which had a stress drop of ~126 bars. This quiet zone persists during the high activity after September 8. Secondly, there is a marked asymmetry to the energy release. The southern, shallower edge of the zone is quite active while the deeper, northern side is quiescent. This may be related to increased normal stress with depth which acts to inhibit deeper aftershocks.

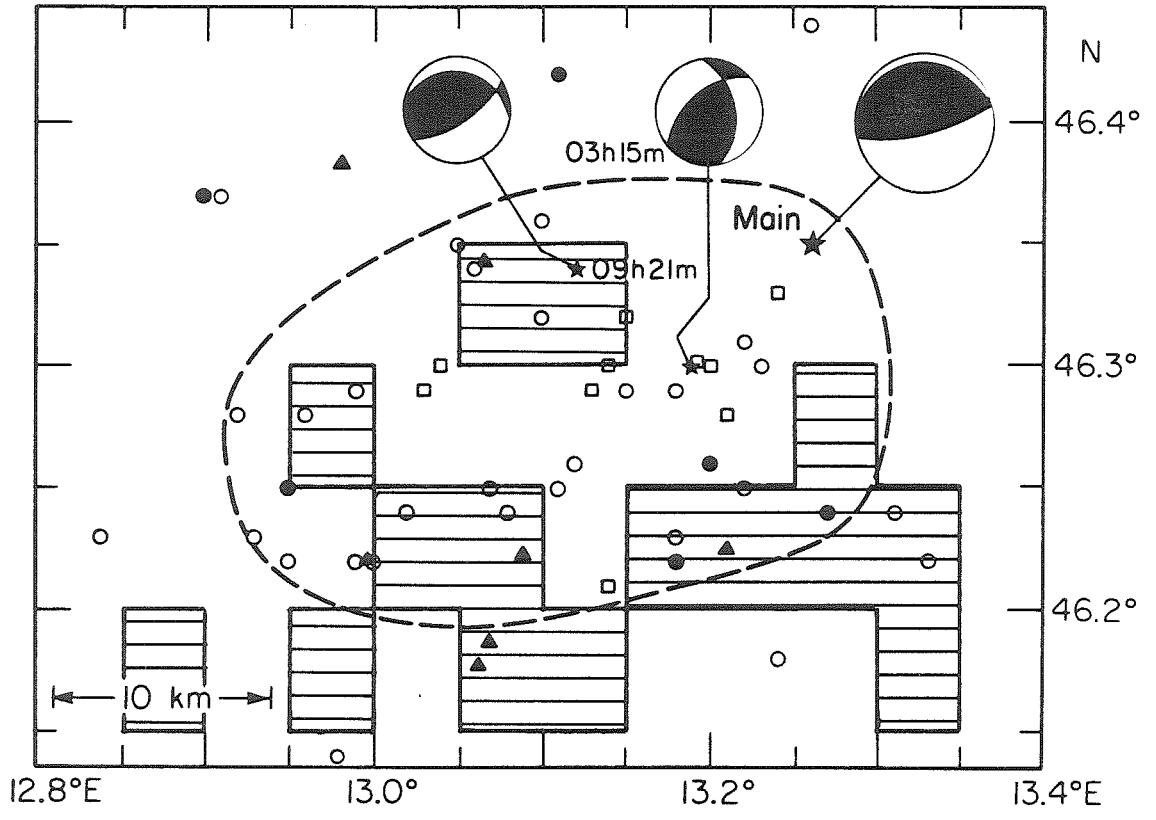

Figure 4-5. Areal aftershock energy release in the Friuli region for the period between May 6 and September 8, 1976. Shaded areas have cumulative aftershock moment release greater than 0.1 x 10^{23} dyne-cm. Other symbols are the same as Figure 2-2.

Alternatively, material properties, in particular fault strength, may change with depth. Finally, the interior of the aftershock zone is particularly quiet. The high moment release in the block containing the 09h 21m aftershock is due to a single M_L = 4.1 event on May 10th.

Summary

This thesis has documented a four month long process of seismic strain release in the Friuli region of northeastern Italy. The sequence began on May 6th, 1976 with a small foreshock followed one minute later by the M_S = 6.5 mainshock. Detailed analysis of short-period records reveals that the earthquake was initiated by massive faulting at a depth of 8 km. Long-period waves were radiated by an elliptically shaped fault plane approximately 15 km wide by 30 km long. Average displacement in this zone was 33 cm. The focal mechanism indicates that movement occurred along a planar surface striking nearly east-west and dipping northward at 15^{o}. The sense of motion on this surface implies southward thrusting of the Alps over the Friuli coastal plain. It should be pointed out that this 15^{o} dipping plane intersects the surface approximately 20 km south of the thrust faults mapped in Figure 2-1, assuming an 8 km deep source at the ISC location (star). This observation implies that the epicenter must either be farther north or that the fault must steepen at shallower depths in order to involve these thrusts directly with the Friuli earthquake.

Two lines of evidence point to the existence of high stress and high strength areas within the main fault plane. Short-period waves

radiated by the mainshock originate from three limited regions (asperities) having stress drops an order of magnitude higher than the overall stress drop of 12 bars. Four months after the mainshock, the 09h 21m aftershock (September 15) was the culmination of a dramatic increase in seismic activity which began four days previously. This earthquake had a mechanism and depth similar to that of the mainshock and it occurred about 10 km westward of the mainshock epicenter. This geometry suggests that this event represents fracture of a high strength part of the main thrust plane. Some slip may have occurred in this zone during the mainshock, but strength and stress levels remained high. Throughout most of the aftershock sequence, from May to September, the impending fault area of the 09h 21m earthquake was free of seismic activity. The stress drop for this aftershock is intermediate between the average value for the mainshock and the individual asperities.

Another large aftershock occurred six hours prior to the 09h 21m event, at 03h 15m. This earthquake was complex in that it was initiated by an event which had a normal fault mechanism while the main movement was characterized by shallow angle thrusting. These two earthquakes, along with the major aftershocks on September 11, represent the failure of the last major region of stress on the thrust surface.

In the broadest sense, the Friuli earthquakes are the consequence of the underthrusting of the African Plate beneath Europe. These earthquakes are not, however, subduction zone events in the classical sense. Rather, the southern Alps represent one zone of a broad area of crustal deformation caused by the plate collision. The Friuli

earthquakes are a single episode in this process of deformation. The contribution of this thesis is the elucidation of the manner in which this deformation occurs.

References

Ahorner, L., H. Murawski and G. Schneider (1972). Seismotektonische traverse von der Nordsee bis zum Apennin, Geol. Runds., vol. 61, 915-942.

Aki, Keiiti (1966). Generation and propagation of G waves from the Niigata earthquake of June 16, 1964. Part 2: Estimation of earthquake moment, released energy, and stress-strain drop from the G wave spectrum, Bull. Earthq. Res. Inst., vol. 44, 73-88.

Allen, Clarence R. and John M. Nordquist (1972). Foreshock, main shock and larger aftershocks of the Borrego Mountain earthquake, in The Borrego Mountain Earthquake of April 9, 1968, USGS Prof. Paper No. 787, 16-23.

Amato, A., P. F. Barnaba, I. Finetti, G. Groppi, B. Martinis and A. Muzzin (1976). Geodynamic outline and seismicity of Friuli-Venetia-Julia region, Boll. Geof. teor. appl., vol. 18, 217-256.

Ambraseys, N. N. (1976a). The Gemona di Friuli earthquake of 6 May 1976, in The Gemona de Friuli Earthquake of 6 May 1976, UNESCO Technical Report RP/1975-76/2.222.3, Paris, France.

Ambraseys, N. N. (1976b). Engineering seismology aspects of the Gemona-Friuli earthquake, Boll. Geof. teor. appl., vol. 18, 257-272.

Anderson, Don L. and R. S. Hart (1978). Attenuation models of the earth, Phys. Earth Planet. Int., vol. 16, 289-306.

Angenheister, G., H. Bogel, H. Gebrande, P. Geise, P. Schmidt-Thome and W. Zeil (1972). Recent investigations of surficial and deeper crustal structures of the eastern and southern Alps, Geologishe Rundschau, vol. 61, 349-395.

Bache, Thomas C., David G. Lambert and Terrance G. Barker (1980). A source model for the March 28, 1975, Pocatello Valley earthquake from time-domain modeling of teleseismic P waves, Bull. Seism. Soc. Am., vol. 70, no. 2, 405-418.

Bakun, W. .H. and A. G. Lindh (1977). Local magnitudes, seismic moments, and coda durations for earthquakes near Oroville, California, Bull. Seism. Soc. Am., vol. 67, no. 3, 615-629.

Ben-Menahem, Ari, M. Rosenman and D. G. Harkrider (1970). Fast evaluation of source parameters from isolated surface wave signals, Bull. Seism. Soc. Am., vol. 60, no. 4, 1337-1387.

Berg, G. V. and G. W. Housner (1961). Integrated velocity and displacement of strong earthquake ground motion, Bull. Seism. Soc. Am., vol. 51, no. 2, 175-189.

Brady, A. G. (1966). Studies of Response to Earthquake Ground Motion, Ph.D. Thesis, Earthquake Engineering Research Laboratory, California Institute of Technology, Pasadena, California 91125.

Bullen, K. E. (1965). An Introduction to the Theory of Seismology, Cambridge Univ. Press, New York, 381pp.

Burdick, Lawrence J. (1977). Broad-Band Seismic Studies of Body Waves, Ph.D. Thesis, California Institute of Technology, Pasadena, California 91125.

Burdick, L. J. and G. R. Mellman (1976). Inversion of the body waves from the Borrego Mountain earthquake to the source mechanism, Bull. Seism. Soc. Am., vol. 66, no. 5, 1485-1499.

Burdick, L. J. and Christine Powell (1980). Apparent velocity measurements for the lower mantle from a wide aperture array, J. Geophys. Res., vol. 85, no. B7, 3845-3856.

Burridge, R. and L. Knopoff (1964). Body force equivalent for seismic dislocations, Bull. Seism. Soc. Am., vol. 54, no. 6, 1875-1888.

Cagnetti, V. and R. Console (1977). Space-time distribution of the Friuli (1976) earthquakes, Ann. di Geof., vol. 30, 107-184.

Cagnetti, Vittorio and Vincenzo Pasquale (1979). The earthquake sequence in Friuli, Italy, 1976, Bull. Seism. Soc. Am., vol. 69, no. 6, 1797-1818.

Caputo, M. (1976). The area of the fault, the dislocation, the stress drop and the seismic moment of the Friuli earthquake of May 6th, 1976, Ann. di Geof., vol. 29, 171-178.

Carpenter, E. W. (1966). Absorption of elastic waves - an operator for a constant Q mechanism, U.K. Atomic Energy Authority, AWRE Report No. 0-43/66.

Carpenter, E. W. and E. A. Flinn (1965). Attenuation of teleseismic body waves, Nature, vol. 207, 745-746.

Chung, Wai-Ying (1978). Part I: Variation of Seismic Source Parameters and Stress Drop within a Descending Slab as Revealed from Body-Wave Pulse Width and Amplitude Analysis, Part II: A Seismological Investigation of the Subduction Mechanism of Aseismic Ridges, Ph.D.

Thesis, California Institute of Technology, Pasadena, California 91125.

Chung, W. Y. and H. Kanamori (1976). Source processes and tectonic implications of the Spanish deep-focus earthquake of March 29, 1954, Phys. Earth Planet. Inter., vol. 13, 85-96.

CNEN-ENEL (1976). Contribution to the Study of Friuli Earthquake of May 1976, CNEN-ENEL Commission on Seismic Problems Associated with the Installation of Nuclear Plants, Rome, Italy, 135pp.

CNEN-ENEL (1977). Uncorrected Accelerograms from the Friuli, Italy Earthquake of May 6, 1976 and Aftershocks (part 3), ibid.

Console, R. (1976). Meccanismo focale del terremoto del Friuli del 6 Maggio 1976, Ann. di Geof., vol. 29, 165-170.

Console, R. and C. Gasparini (1976). Hypocentral parameters for the Friuli, May 6th 1976 earthquake, Ann. di. Geof., vol. 29, 153-159, in Italian.

Der, Zoltan, Eugene Smart and Audrey Chaplin (1980). Short-period S-wave attenuation under the United States, Bull. Seism. Soc. Am., vol. 70, no. 1, 101-125.

Ebblin, C. (1976). Orientation of stresses and strains in the Piedmont area of eastern Friuli, NE Italy, Boll. Geof. teor. appl., vol. 18, 559-579.

Ebel, John (1980). Evidence for Fault Asperities from Systematic Time-Domain Modeling of Teleseismic Waveforms, Ph.D. Thesis, California Institute of Technology, Pasadena, California 91125.

Ebel, John, L. J. Burdick and G. S. Stewart (1978). The source

mechanism of the August 7, 1966 El Golfo earthquake, Bull. Seism. Soc. Am., vol. 68, no. 5, 1281-1292.

Eshelby, J. D. (1957). The determination of the elastic field of an ellipsoidal inclusion and related problems, Proc. Roy. Soc. London, Series A, vol. 241, 376-396.

Finetti, I. and C. Morelli (1972). Deep seismic refraction exploration on Eastern Alps, Boll. Geof. teor. appl., vol. 14, 59-66.

Finetti, I., M. Russi and D. Slejko (1979). The Friuli earthquake (1976-1977), Tectonophysics, vol. 53, 261-272.

Frasier, Clint W. and John Filson (1972). A direct measurement of the Earth's short-period attenuation along a teleseismic ray path, Jour. Geophys. Res., vol. 77, no. 20, 3782-3787.

Fuchs, Karl (1966). The transfer function for P-waves for a system consisting of a point source in a layered medium, Bull. Seism. Soc. Am., vol. 56, no. 1, 75-108.

Futterman, Walter I. (1962). Dispersive body waves, J. Geophys. Res., vol. 67, no. 13, 5279-5291.

Geller, Robert J. (1976). Scaling relations for earthquake source parameters and magnitudes, Bull. Seism. Soc. Am., vol. 66, no. 5, 1501-1523.

Greensfelder, Roger (1968). Aftershocks of the Truckee, California earthquake of September 12, 1966, Bull. Seism. Soc. Am., vol. 58, no. 5, 1607-1620.

Gu, H., Y. T. Chen, X. Gao and Y. Zhao (1976). Focal mechanism of

Haicheng, Liaoning Province, earthquake of February 4, 1975, Acta Geophys. Sin., vol. 19, 270 (in Chinese).

Gutenberg, B. and C. F. Richter (1954). Seismicity of the Earth, Hafner Publ. Co., New York, 310 pp.

Gwinner, M. P. (1971). Geologie der Alpen, Schweizesbart, Stuttgart, 477 pp.

Hadley, D. and H. Kanamori (1978). Recent seismicity in the San Fernando region and tectonics in the west-central Transverse ranges, California, Bull. Seism. Soc. Am., vol. 68, no.5, 1449-1457.

Hagiwara, Takahiro (1958). A note on the theory of the electro-magnetic seismograph, Bull. Earthq. Res. Inst., vol. 36, 139-164.

Hartzell, Stephen (1980). Faulting process of the May 17, 1976 Gazli, U.S.S.R. earthquake, Bull. Seism. Soc. Am., vol. 70, no. 5, 1715-1736.

Hartzell, Stephen and James N. Brune (1979). The Horse Canyon earthquake of August 2, 1975 - Two stage stress release process in a strike-slip earthquake, Bull. Seism. Soc. Am., vol. 69, no. 4, 1161-1173.

Haskell, Norman A. (1960). Crustal reflection of plane SH waves, J. Geophys. Res., vol. 65, no. 12, 4147-4150.

Haskell, Norman A. (1962). Crustal reflection of plane P and SV waves, J. Geophys. Res., vol. 67, no. 12, 4751-4767.

Haskell, N. A. (1964). Total energy and energy spectral density of elastic wave radiation from propagating faults, Bull. Seism. Soc.

Am., vol. 54, no. 6, 1811-1841.

Heaton, T. H. (1978). Generalized Ray Models of Strong Ground Motion, Ph.D. Thesis, California Institute of Technology, Pasadena, California 91125.

Heaton, Thomas H. (1980). The 1971 San Fernando earthquake; a double event, abstract, Eos (Am. Geophys. Union, Trans.), vol. 61, no. 46, 1027.

Helmberger, Donald V. (1968). The crust-mantle transition in the Bering Sea, Bull. Seism. Soc. Am., vol. 58, no. 1, 179-214.

Helmberger, Donald V. (1974). Generalized ray theory for shear dislocations, Bull. Seism. Soc. Am., vol. 64, no. 1, 45-64.

Helmberger, D. V. and L. J. Burdick (1979). Synthetic seismograms, Ann. Rev. Earth Planet. Sci., vol. 7, 417-442.

Helmberger, Donald V. and David G. Harkrider (1978). Modeling Earthquakes with Generalized Ray Theory, in Modern Problems in Elastic Wave Propagation, J. Miklowitz and J. Achenbach (eds.), John Wiley and Sons.

Helmberger, Donald V. and Stephen D. Malone (1975). Modeling local earthquakes as shear dislocations in a layered halfspace, Jour. Geophys. Res., vol. 80, no. 35, 4881-4888.

Hong, T. L. and D. V. Helmberger (1978). Glorified optics and wave propagation in nonplanar structure, Bull. Seism. Soc. Am., vol. 64, 1313-1330.

Hsu, S. H. (1976). Characteristics of the Haicheng Earthquake of 1975 in Proceedings of the Lectures by the Seismological Delegation of

the People's Republic of China, Paul M. Muller, editor, Jet Propul. Lab., Calif. Inst. of Technol., Pasadena.

Hutton, L. Katherine and others (1980). Caltech-USGS Monthly Preliminary Epicenters for October 1979 through December 1979, Seismological Laboratory, California Institute of Technology, Pasadena, California 91125.

Kanamori, Hiroo and Don L. Anderson (1975). Theoretical basis of some empirical relations in seismology, Bull. Seism. Soc. Am., vol. 65, no. 5, 1073-1095.

Kanamori, Hiroo and Don L. Anderson (1977). Importance of physical dispersion in surface wave and free oscillation problems: review, Rev. Geophys. and Space Phys., vol. 15, no. 1, 105-112.

Kanamori, H. and G. Stewart (1976). Mode of strain release along the Gibbs Fracture Zone, Mid-Atlantic Ridge, Phys. Earth Planet. Inter., vol. 11, 312-332.

Karnik, V. (1971). Seismicity of the European Area, Part II, D. Reidel Publ. Co., Dordrecht-Holland, 218 pp.

Kawasaki, Ichiro, Yasunori Suzuki and Ryosuke Sato (1973). Seismic waves due to a shear fault in a semi-infinite medium, Part I: point source, J. Phys. Earth, vol. 21, 251-284.

Langston, Charles Adam (1976a). Body Wave Synthesis for Shallow Earthquake Sources: Inversion for Source and Earth Structure Parameters, Ph.D. Thesis, California Institute of Tecnology, Pasadena, California 91125.

Langston, Charles A. (1976b). A body wave inversion of the Koyna,

India earthquake of December 10, 1967 and some implications for body wave focal mechanisms, J. Geophys. Res., vol. 81, no. 14, 2517-2529.

Langston, C.A. (1977). The effect of planar dipping structure on source and receiver responses for constant ray parameter, Bull. Seism. Soc. Am., vol. 67, 1029-1050.

Langston, Charles A. (1978). The February 9, 1971 San Fernando earthquake: a study of source finiteness in teleseismic body waves, Bull. Seism. Soc. Am., vol. 68, no. 1, 1-30.

Langston, Charles A. and Rhett Butler (1976). Focal mechanism of the August 1, 1975 Oroville earthquke, Bull. Seism. Soc. Am., vol. 66, no. 4, 1111-1120.

Langston, Charles A. and Donald V. Helmberger (1975). A procedure for modeling shallow dislocation sources, Geophys. J. R. astr. Soc., vol. 42, 117-130.

Lort, J. M. (1971). The tectonics of the eastern Mediterranean: a geophysical review, Rev. Geophys. Space Phys., vol. 9, 189-216.

Madariaga, Raul (1976). Dynamics of an expanding circular fault, Bull. Seism. Soc. Am, vol. 66, no. 3, 639-666.

Martinis, B. (1975). The Friulian and Julian Alps and Pre-Alps, Chapter 2 in Structural Model of Italy, L. Ogniben, M. Parotto and A. Proturlon (eds.), Consiglio Nazionale delle Ricerche, Rome.

Mayer-Rosa, D., N. Pavoni, R. Graf and B. Rast (1976). Investigations of intensities, aftershock statistics and the focal mechanism of Friuli earthquakes in 1975 and 1976, Pure Appl.

Geophys., vol. 114, 1095-1103.

McEvilly, T. V., W. H. Bakun and K. B. Casaday (1967). The Parkfield, California, earthquake of 1966, Bull. Seism. Soc, Am., vol 57, no. 6, 1221-1244.

McKenzie, D. P. (1972). Active tectonics of the Mediterranean Region, Geophys. J. R. astr. Soc., vol. 30, 109-185.

Mellman, George R. (1978) A Method for Waveform Inversion of Body-Wave Seismograms, Ph.D. Thesis, California Institute of Technology, Pasadena, California 91125.

Mogi, K. (1968). Development of aftershock areas of great earthquakes, Bull. Earthquake Res. Inst., vol. 46, 175-203.

Morrison, Paul W., Brian W. Stump and Robert Uhrhammer (1976). The Oroville earthquake sequence of August 1975, Bull. Seism. Soc. Am., vol. 66, no. 4, 1065-1084.

Muller, G. (1977). Fault-plane solution of the earthquake in northern Italy May 6, 1976, and implications for the tectonics of the eastern Alps, J. Geophys., vol. 42, 343-349.

Ohnaka, Mitiyasu (1973). A physical understanding of the earthquake source mechanism, J. Phys. Earth., vol. 21, 39-59.

Papazachos, B. C. (1973). Distribution of seismic foci in the Medterranean and surrounding area and its teconic implications, Geophys. J. R. astr. Soc., vol. 33, 421-430.

Raleigh, B., G. Bennett, H. Craig, T. Hanks, P. Molnar, A. Nur, J. Savage, C. Scholz, R. Turner and F. Wu (1977). Prediction of the Haicheng earthquake, Eos (Am. Geophys. Union, Trans.), vol.

58, 236-272.

Ritsema, A. R. (1976). Preliminary analysis of Friuli earthquake records, Boll. Geof. teor. appl., vol. 18, 875-887.

Savage, J. C. (1965). The effect of rupture velocity on seismic first motions, Bull. Seism. Soc. Am., vol. 55, no. 2, 263-275.

Savage, J. C. (1966). Radiation from a realistic model of faulting, Bull. Seism. Soc. Am., vol. 56, no. 2, 577-592.

Savage, J. C. (1972). Relation of corner frequency to fault dimensions, J. Geophys. Res., vol. 77, 3788-3795.

Scholz C. H. (1977). A physical interpretation of the Haicheng earthquake prediction, Nature, vol. 267, 121-124.

Somerville, Paul G., Ralph A. Wiggins and Robert M. Ellis (1976). Time domain determination of earthquake fault parameters from short-period P-waves, Bull. Seism. Soc. Am., vol. 66, no. 5, 1459-1484.

Stewart G. S., R. Butler and H. Kanamori (1976). Surface and body wave analysis for the February 4, 1975 Haicheng and July 27, 1976 Tangshan Chinese earthquakes, abstract, Eos (Am. Geophys. Union, Trans.), vol. 57, 953.

Stierman, Donald J. and William J. Ellsworth (1976). Aftershocks of the February 21, 1973 Point Mugu, California earthquake, Bull. Seism. Soc. Am., vol. 66, no. 6, 1931-1952.

Trifunac, M. D. (1972). A note on correction of strong-motion accelerograms for instrument response, Bull. Seism. Soc. Am., vol. 62, no. 1, 401-409.

Tsai, Yi-Ben and Keiiti Aki (1969). Simultaneous determination of the seismic moment and attenuation of seismic surface waves, Bull. Seism. Soc. Am., vol. 59, no. 1, 275-287.

Tsai, Yi-Ben and Keiiti Aki (1970). Source mechanism of the Truckee, California earthquake of September 12, 1966, Bull. Seism. Soc. Am., vol. 60, no. 4, 1199-1208.

Uhrhammer, R. A. (1980). Observations of the Coyote Lake, California earthquake sequence of August 6, 1979, Bull. Seism. Soc. Am., vol. 70, no. 2, 559-570.

Wallace, Terry C., Don V. Helmberger and John E. Ebel (1981). A broadband study of the August 13, 1978 Santa Barbara earthquake, in preparation.

Whitcomb, James H. and others (1979). Caltech-USGS Monthly Preliminary Epicenters from March 1978 to January 1979, Seismological Laboratory, California Institute of Technology, Pasadena, California 91125.

Wu, K.-T., M.-S. Yue, H.-Y. Wu, S.-L. Chao, H.-T. Chen, W.-Q. Huang, K.-Y. Tien, and S.-D. Lu (1976). Certain characteristics of the Haicheng earthquake (M = 7.3) sequence, Acta Geophys. Sinica, vol. 19, 95-109, reprinted in Chinese Geophysics, vol. 1, no. 2, 289-308.

Wyss, M. and J. N. Brune (1968). Seismic moment, stress and source dimensions for earthquakes in the California-Nevada region, J. Geophys. Res., vol. 73, 4681-4694.

Wyss, M. and T. C. Hanks (1972). The source parameters of the San

Fernando earthquake from teleseismic body waves, Bull. Seism. Soc. Am., vol. 62, no. 2, 591-602.